5 Analysis of Experimental Image Sequences

This chapter deals with the analysis of the statistical properties and the spatio-temporal metabolic dynamics of the population of cells in leaves of *Kalanchoë daigremontiana* . The spatially resolved information about the metabolic state is retrieved by imaging of leaf chlorophyll fluorescence. The same different temperature conditions in continuous light as discussed in Chapter 4 are considered: rhythmic and arrhythmic free-running conditions, as well as slow versus fast temperature changes.

5.1 Chlorophyll Fluorescence Imaging

The chlorophyll fluorescence signal is a plant-intrinsic probe of photosynthetic function (Genty et al. 1989). As it is a non-invasive method to detect any change in the overall bioenergetic status of the plant, it has become a routine method for ecophysiological studies in many laboratories.

5.1.1 Plant Physiological Background

Chlorophyll Fluorescence Signal

Chlorophyll-a molecules represent the principal class of pigments responsible for light absorption in photosynthesis (Lüttge et al. 1997; Nobel 1999). They are gathered in the photosystems, i.e. pigment clusters situated at the thylakoid membrane of the chloroplasts. The light energy absorbed by the photosystems first excites light harvesting molecules, which submit the absorbed energy to the reaction center of the photosystem, consisting of so-called excitation-trap chlorophyll molecules. The de-excitation of the trap-chlorophyll can occur via two pathways. Either the excited electron is transferred via a phaeophytin molecule to a quinone, which stabilizes the charge separation. The quinone is also the first element of a series of molecules representing the electron transfer chain, at the end of which biochemical energy carriers NADP are reduced. The missing electron in the trap molecule is replaced by an electron emerging from the oxidation of water. Alternatively, if the rate constant for electron transfer is slowed down due to a saturation of the electron transport chain with electrons, the trap molecule returns to its ground state by emission of a fluorescence photon (Fig. 5.1).

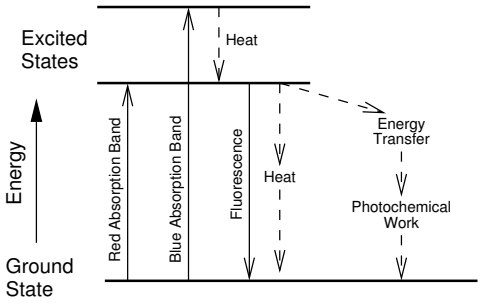

Figure 5.1: Energy scheme of chlorophyll molecules. Excitation can occur via absorption of photons in the red ($\approx$ 680 nm) or blue ($\approx$ 430 nm) range of the visible spectrum. The higher excited states decays quickly to the lowest excited state by radiationless transition, i.e. heat emission (dashed line). The lowest excited state can be de-excited by emission of a photon giving the fluorescence light of $\approx$ 700 nm, or by electron transfer to plastoquinone A, the first electron acceptor of the electron transport chain. These electrons are finally used for reduction of biochemical energy carriers.

A measure of the quantitative relation of the competing deexcitation pathways is the quantum yield, or quantum efficiency Φ which depends on the involved rate constants k_i (Nobel 1999):

$$\Phi_i = \frac{\text{number of molecules using } i\text{th deexcitation reaction}}{\text{number of excited molecules}} = \frac{k_i}{\sum_i k_i} \tag{5.1}$$

Equation 5.1 indicates that the rate constant for a particular pathway determines what fraction of the molecules in a given excited state will use that deexcitation pathway. In the present case, the rate constant of the photochemical pathway, that is electron transport, depends on the energy demand of the cell, i.e. the abundance of oxidized, electron accepting NADP molecules. The rate constant, and hence the quantum yield increases when there is a high energy demand. The quantum efficiency of photochemical reaction at photosystem II (Φ_{PSII}) is thus a measure of the metabolic state of the cell (Genty et al. 1989). A consequence of a preferred de-excitation via electron transfer is a quenching of the fluorescence signal, such that the leaf chlorophyll fluorescence (F) enables the determination of Φ_{PSII} and, consequently, the metabolic status of a cell or a leaf patch.

Saturating Pulse Method

As the absolute number of excited molecules is not available for calculation of Φ_{PSII}, relative quantum efficiencies have to be determined. This is accomplished by the saturating pulse method (Schreiber et al. 1986; Schreiber & Bilger 1993): to obtain the relative quantum efficiency of photochemical reactions in photosystem II, the chlorophyll fluorescence signal is measured two consecutive times: once before (F), and once during a short pulse of extremely high light intensity, giving the maximal fluorescence (F^{max}). The intense

light flash causes a saturation of the electron transfer chains with electrons, such that during the second measurement, all deexcitations occur via fluorescence, resulting in a maximum fluorescence signal (F^{max}). Φ_{PSII} is then calculated as (Genty et al. 1989)

$$\Phi_{\mathrm{PSII}} = \frac{F^{max} - F}{F^{max}} = 1 - \frac{F}{F^{max}} \tag{5.2}$$

5.1.2 Imaging and Scaling

The data presented in this chapter are based on recordings of Φ_{PSII} with a sampling interval of $\delta t = 20$ min. After recording of the image F_{ij}, the photon flux density L during 1 second was raised to 1200-1500 μE m^{-2}s^{-1} (cf. Appendix D), providing the saturating light flash. During this flash, the image of F_{ij}^{max} was recorded (Rascher 2001). Each image contains 768x512 pixels with a 14 bit resolution (16384 grey-levels). One pixel corresponds to a disk with a diameter of ≈ 200 μm. which is a little less than the average diameter of a mesophyll cell of *K. daigremontiana* (Rascher et al. 2001). In order to stay within the limits of the available computer memory and to maintain processing speeds reasonable, in this work the images are rebinned by a factor of 4, such that one data set Φ_{ijk} consists of $N_i \cdot N_j \cdot N_k, N_i = 192, N_j = 128$ pixels sampled at N_k times ($N_k \approx 72\cdot$ duration of imaging given in days).
Fig. 5.2 shows the histograms of Φ_{ijk} from three different image series. In every case, the distribution of the Φ_{PSII} values is centered around a value close to 0.9, with a width of about a few percent. In order to make the data sets comparable, all Φ_{ijk} are scaled to the maximum likelihood value of the distribution Φ^{MLH}, which is indicated by the dotted lines in Fig. 5.2.

$$\tilde{\Phi}_{ijk} = \frac{\Phi_{ijk}}{\Phi^{MLH}} \tag{5.3}$$

In order to keep the equations simple, the tilde is going to be omitted for the rest of this work.

5.1.3 Correlation with Gas Exchange Dynamics

A crucial question about the Φ_{PSII} signal is its relation to the simultaneously measured gas exchange of the leaf. Figure 5.3 shows timeseries in LL of $\hat{\Phi}_k =< \Phi_{ijk} >_{ij}$, J_c and c_{ia} (ref. Appendix D) for different environmental conditions (corresponding to Fig. 5.2). The left column of Fig. 5.3 (Series 1) represents the dynamics under rhythm conditions (21^{o}C, 192 μE m^{-2}s^{-1}). A clear correlation of $\hat{\Phi}$ and J_c is given, as well as a significant anti-correlation of $\hat{\Phi}$ and c_{ia} . A possible phase-shift between the maximum of J_c and the minimum has not been quantified. The physiological reasons behind this specific correlation and phase relation comprise the temporal pattern of energy demand of Rubisco, as well as gluconeogenesis following the decarboxylation of malic acid, which is discussed in detail in Rascher (2001). The middle column of Fig. 5.3 shows a timeseries

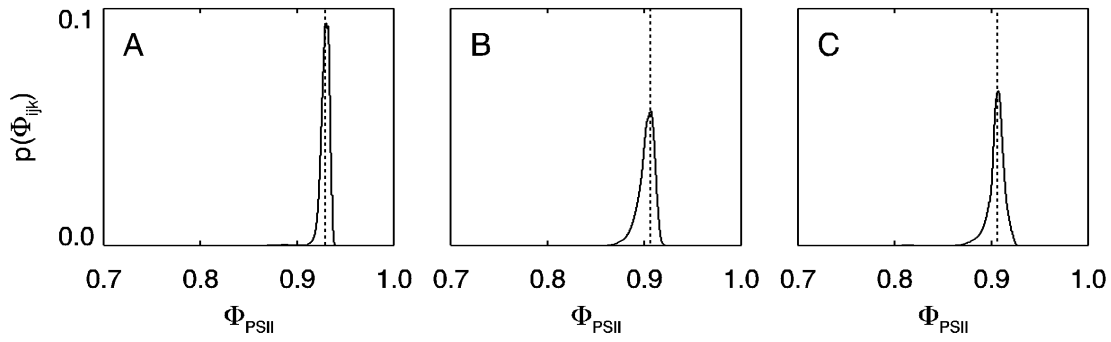

Figure 5.2: Histogram of Φ_{ijk}. **A:** Rhythmic timeseries, 21^{o}C, 192 μE m^{-2}s^{-1} , 0 - 240 h in LL. **B:** Arrhythmic timeseries, 28^{o}C, 201 μE m^{-2}s^{-1} , 0 - 144 h in LL. **C:** timeseries with fast and slow temperature variations between 31^{o}C and 24^{o}C, 140 μE m^{-2}s^{-1} , 0 - 240 h in LL. The dotted lines mark the maximum likelihood value of the distribution (Φ^{MLH}), which is used as reference value in this work for scaling of Φ_{ijk}.

in arrhythmic conditions (28^{o}C, 192 μE m^{-2}s^{-1}). All three quantities are arrhythmic, and a correlation analysis (data not presented) does not reveal any significant correlations hidden in the data. The right column of Fig. 5.3 (Series 3) contains data of experiments with slow and fast temperature changes. While the rhythm re-initiation of J_c observed at about 3 d in LL (Fig. 5.3F) is not covered by $\hat{\Phi}$, the response to the fast temperature change (at 6-6.5 d in LL) is visible in the chlorophyll fluorescence data. Overall this indicates that at least for rhythmic conditions and strong stimuli one may infer leaf CO_2 relations from the photochemical yield.

5.2 Rhythmic Conditions

One of the central questions about the CR of *Kalanchoë daigremontiana* under conditions where the rhythm is clearly expressed is about the origin of the rhythm damping. As was quantitatively hypothesized in the preceding Chapter 4, it could either be a phenomenon which is only observed on the level of the collective rhythm, or it might as well have a local origin. Figure 5.4 shows the time series of Φ_{PSII} in four arbitrarily selected points in the leaf and the spatial average, at 21^{o}C and a photon flux (L) of about 192 μE m^{-2}s^{-1} . Three of the four points clearly show timeseries with waveforms similar to the collective rhythm. This spot-check is a first indication that damping might be a local event and not only a global phenomenon.

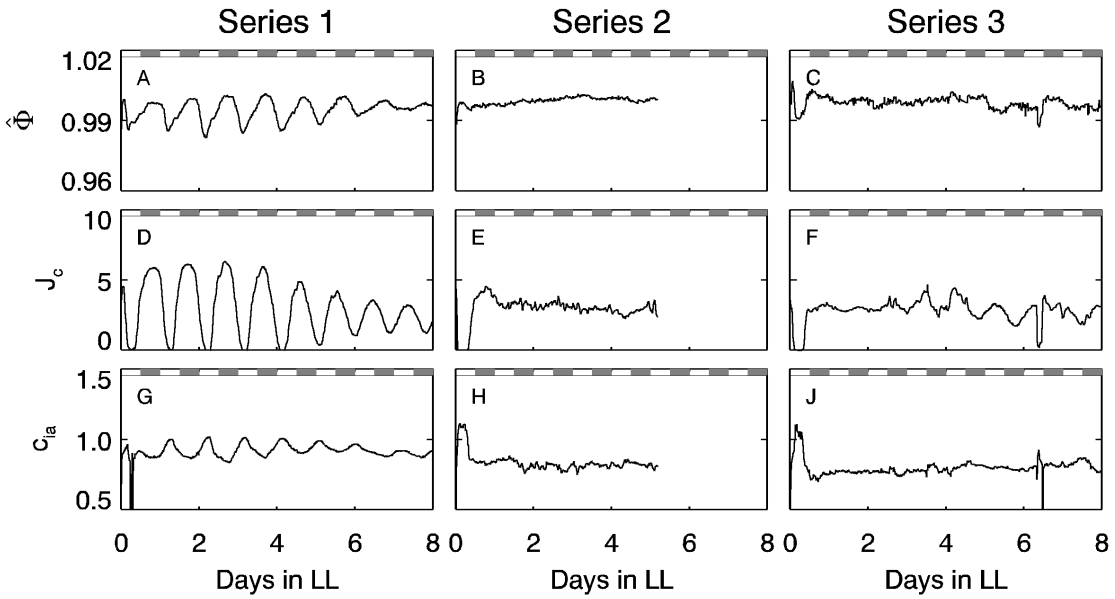

Figure 5.3: Comparison of the time-course of $\hat{\Phi}$ (**A**-**C**), J_c (**D**-**F**) and c_{ia} (**G**-**J**). The left column shows a rhythmic timeseries, parameters are identical to Fig. 5.2A. Series 2 in the middle column represents the arrhythmic series (parameters like 5.2B). Series 3 corresponds to the series with slow and fast temperature-changes , Fig. 5.2C.

5.2.1 Population Statistics

Figure 5.5 shows the population statistics of the rhythm properties of 192x128 = 24576 pixels as a function of time. The arrangement of the subfigures is identical as the subfigures K-N as discussed in Table 4.2. Figures 5.5A,B show $\hat{\Phi}_{PSII}$ and its LS-spectrum, clearly exhibiting circadian oscillations. Fig. 5.5C contains the amplitude of the average $A(\hat{\Phi}_k$, the average amplitude $\hat{A}_k$ and the population phase scatter D_k. Clearly, there is an increase of the phase scatter over time (dotted line), however, the amplitude of the average and the average amplitude are correlated to each other. This indicates that there is both increasing phase dispersal but at the same time, the amplitude dynamics are a local phenomenon as well, hence it appears like a mixture of the scenarios exhibited in Figs. 4.8 and 4.9. Fig. 5.5D is the distribution of dominant frequencies in the population. It indicates a certain amount of heterogeneity of dominant frequencies, being centered around the circadian frequency, and there is obviously a subpopulation of slow oscillators ($\nu^{dom} \approx 0.2$ cycles/day) and a subpopulation of oscillators with the second circadian harmonic ($\nu^{dom} \approx 2$ cycles/day) being dominant.

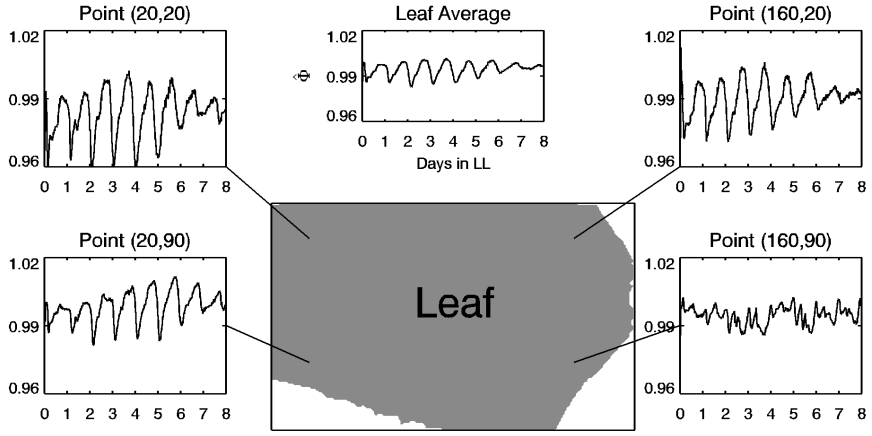

Figure 5.4: Dynamics of four points of four individual pixels of a rhythmic timeseries (T_L =21^{o}C, L= 192 μE m^{-2}s^{-1}). In top center the spatial average $\hat{\Phi}$ is plotted, while to the left and right, the individual timeseries are plotted. Lines link the individual plot to their location in the leaf. The petiole is situated between points (160,20) and (160,90).

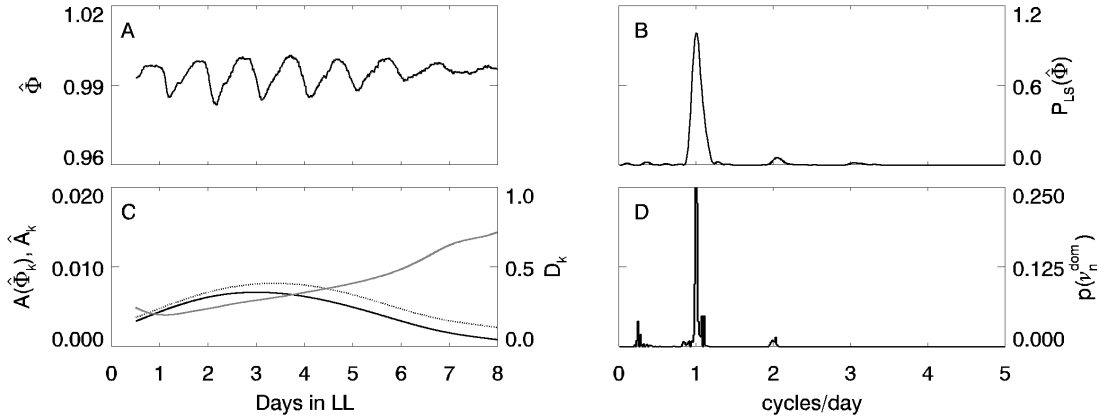

Figure 5.5: Population statistics of the timeseries of Fig. 5.4. **A:** Meanfield rhythm ($\hat{\Phi}$), **B:** Normalized powerspectrum of $\hat{\Phi}$. **C:** Amplitude of average (A($\hat{\Phi}$), solid black line), average amplitude ($\hat{A}(\Phi_{ij})$, dotted black line) and population phase scatter (D_k, grey line). **D:** Distribution of dominant frequencies in population ($p(\nu^{dom})$).

5.2.2 Spatio-Temporal Dynamics

Snapshots

The characteristic spatio-temporal dynamics observed for this leaf is featured by a sequence of 48 single images with inter-image intervals of about an hour, starting at 24 h in LL (Fig. 5.6). The most marking feature in these pictures is the region of relatively low Φ_{PSII} in the upper left corner, which during one circadian cycles enlarges and then shrinks again. This is an obvious result of heterogeneity and belongs to a class of "waves" that have also been observed for calcium waves for instance (Keener & Sneyd 1998). As discussed in Chapter 3.3, this pattern is not a wave being described by PDEs with an explicit spatial coupling of the each point, but emerges from a spatial dependence of internal and/or external parameters determining the phase of each oscillator, which causes kinematic, or pseudo- or phase waves (Murray 1993; Winfree 2001).
Another prominent area is situated in the bottom half of the leaf, where a conjuction of patches deviates from the spatial gradient being observed and which do not take part in the phase wave dynamics explained above. This dynamics and a possible link to the leaf middle vein is most obvious in the bottom row of snapshots, i.e. for $t \geq 65.9$ h.
That phase-waves plus heterogeneity are behind this pattern becomes also evident from snapshots of the phase (Fig. 5.7). Such snapshots of the phase of the pixels taken at the identical times as in Fig. 5.6 reveal running phase waves, spreading from the upper left to lower right corner. Another noteworthy fact discovered by this analysis is the phase dynamics of the leaf area along the middle vein. Especially at the point where the petiole is connected to the leaf and also somewhat further up the vein, there are areas 12 circadian hours (180^o) out of phase with the surrounding leaf tissue. Interestingly the odd points observed in the lower leaf half are in phase with the areas along the vein. These findings are further quantified by looking at the spatial distribution of rhythm quantities.

Spatial Distribution of Rhythm Parameters

Analyzing the image by applying timeseries analysis tools pixel-wise yields the spatial distribution of rhythm properties (Fig. 5.8 top). The temporal average $\overline{\Phi}_{ij} = \sum_k \Phi_{ijk}/N_k$ is plotted in Fig. 5.8A. As expected from the snapshots, the upper left corner exhibits the lowest average. The apparent gradient in rhythm parameters, which extends from the upper left to the lower right of the image, is also seen in the plot of the average amplitude (Fig. 5.8B), with the highest amplitudes being situated in upper half of the leaf. Spectral analysis (Fig. 5.8C) gives a more complex image. Again the fastest oscillators are observed in the upper half of the leaf, with the fastest oscillators being found at the top rim of the image. In the lower half of the leaf however, an extended pattern of dominant frequencies in the infradian range is shown, i.e. periods above 32 h are dominant. Interesting to see is the area of the petiole where very fast oscillation $\tau^{dom} < 16$h are prominent. These fast oscillators correspond to the smaller peak at $\nu^{dom} \approx 2$ in the distribution 5.5D.

The bottom row of Fig. 5.8 shows the phase relations of each Φ_{ij} with $\hat{\Phi}$. Fig. 5.8D exhibits the mean phase difference $\overline{\Delta\varphi}(\Phi_{ij} : \hat{\Phi})$. The sources of the phase waves are evidenced by the positive values of this quantity in the northernmost of the image. The middle part of the leaf is in phase with the meanfield, while the 180^o phase-shift of the odd areas is clearly visible by the white color stains. The cross-correlation function shows high values throughout the leaf, except for the mentioned alternative areas, indicating that the waveform of the majority of the Φ_{ij} is very similar to the waveform of $\hat{\Phi}$ (Fig. 5.8E). The synchronization index $S(\Phi_{ij} : \hat{\Phi})$ shows a pattern of high synchrony, which is symmetric with respect to the vein, however the vein area itself does not show any high synchronization (Fig. 5.8F). Interesting to notice is that the areas of significant S at first glance occupy the same the area of 22 h $< \nu^{dom} <$ 24 h (Fig. 5.8C), as well as the areas of $\Delta\varphi(\Phi_{ij} : \hat{\Phi}) \approx 0$ (Fig. 5.8D). Knowing about these phase dynamics, it may be speculated that the frequency doubling observed near the petiole spot could result from the superposition of a circadian signal being in phase with the widest part of the leaf, and a circadian signal around the petiole being π out of phase.

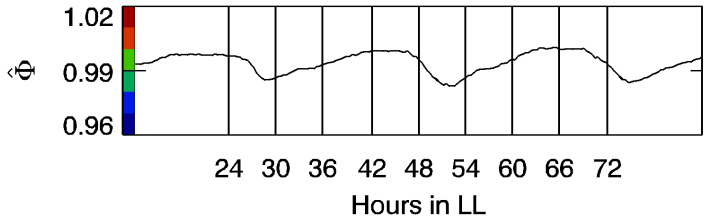

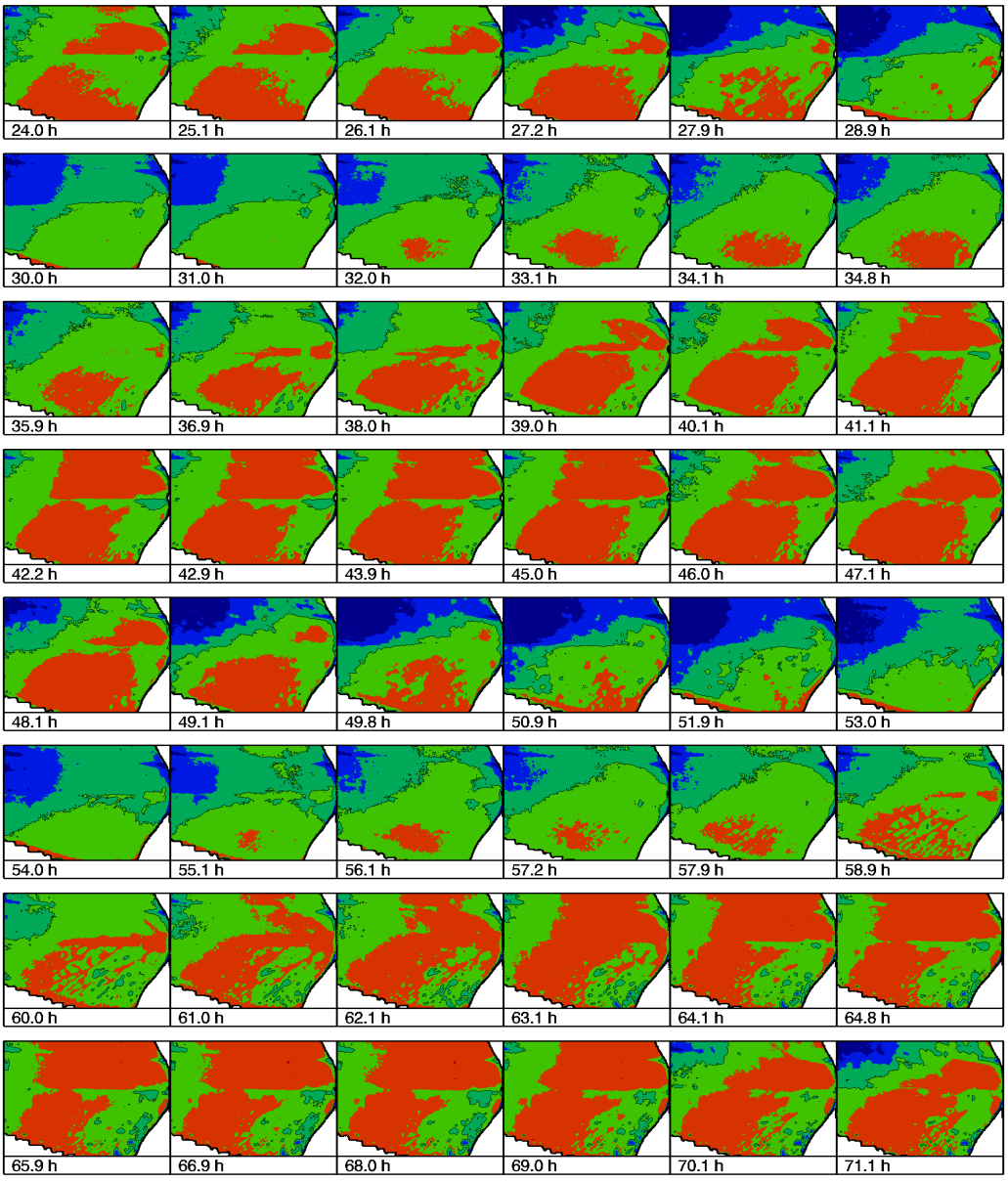

Figure 5.6: Snapshots of Φ_{ijk} of the rhythmic timeseries shown in Fig. 5.4,5.5. **Top:** $\hat{\Phi}$ for a time-section between 0 and 96 h in LL. Vertical bars mark the times of leftmost image in each row of snapshots. The color bar gives the coding for the snapshot images. **Bottom:** Series of snapshots of Φ_{ij}. Images range times from 24 - 71 h in LL, with a time of $\approx$ 1 h between each image.

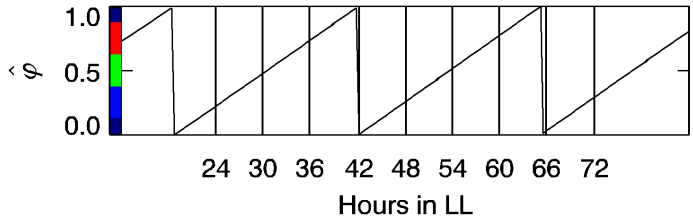

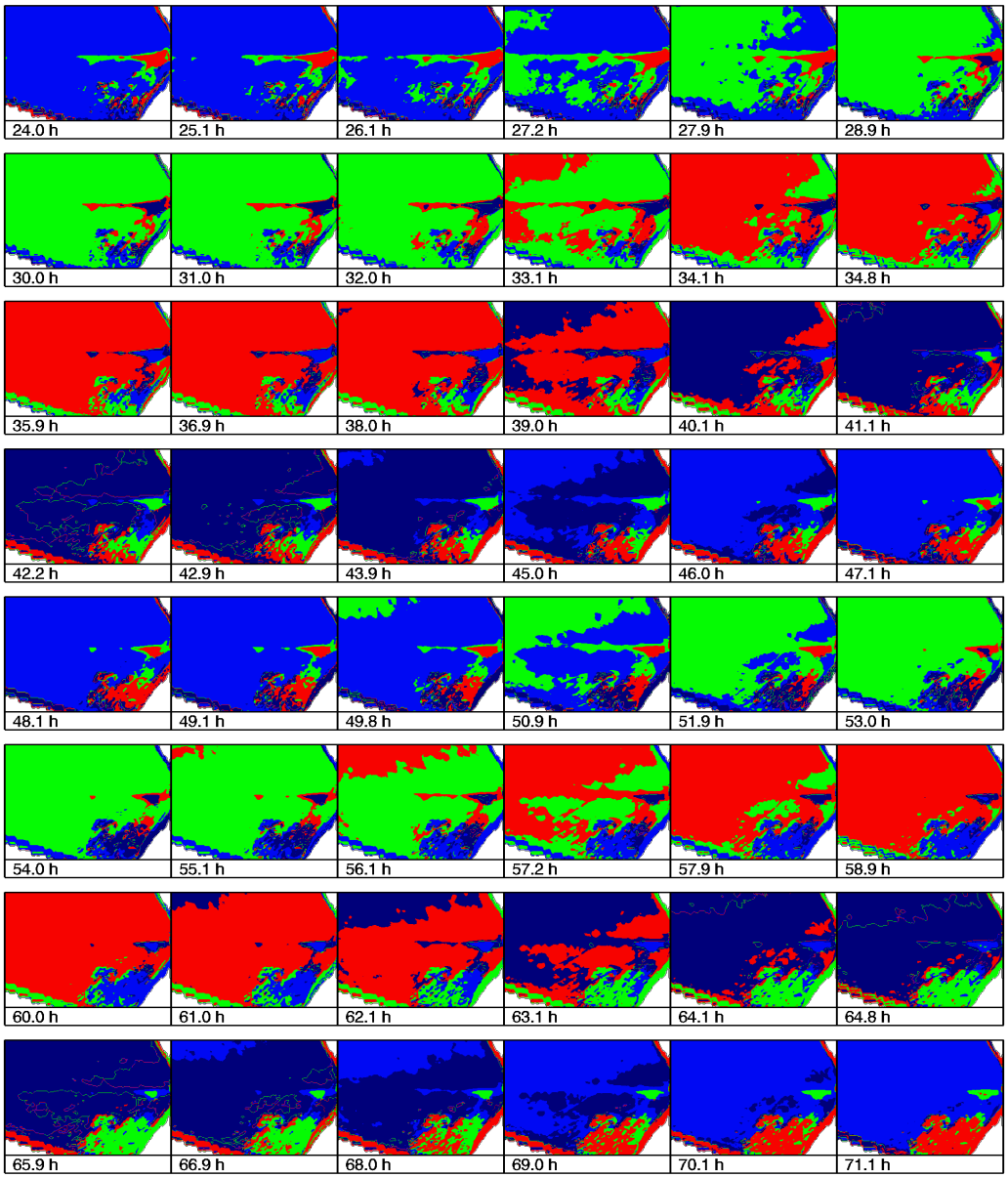

Figure 5.7: Snapshots of $\varphi(\Phi_{ijk}\,)$ of the rhythmic timeseries Fig. 5.4. **Top:** $\varphi(\hat{\Phi})$ for a time-section between 0 and 96 h in LL. Vertical bars mark the times of the leftmost image in each row of snapshots. The color bar gives the coding of the snapshot images. **Bottom:** Series of snapshots of $\varphi(\Phi_{ij})$. The times of snapshots are identical to Fig. 5.6 and range from 24 - 71 h in LL, with a time of $\approx$ 1 h between each image.

5.2.3 Rhythm Correlations

The quantities used for comparison of $\hat{\Phi}$ and Φ_{ij} (Fig. 5.8 bottom) are now being applied to reveal possible relations between the set of Φ_{ij} and i) a reference timeseries $\Phi_{i'j'}$ of a particular pixel with coordinates (i',j') and ii) the timeseries of light intensity L and water vapor pressure deficit (Δw, see Appendix D).

Relations between Leaf Pixels

The phase relations of four selected points (i',j') in the leaf with all other points (i,j) is shown in Fig. 5.9. In correlation to the structure of Fig. 5.8, the left column shows the $\overline{\Delta\varphi}$ ($\Phi_{ij} : \Phi_{i'j'}$). All four points again are consistent with the previous analyses, in that the first oscillators to reach a certain phase are situated at the top of the image, with a gradual diminution of the phase shifts in the southeastern direction of the image (Fig. 5.9A,D,G,K). Again, the spot where the petiole meets the leaf, and an extended area in the bottom half are out of this gradual pattern. The middle column with the cross-correlations C($\Phi_{ij} : \Phi_{i'j'}$) shows two complementary areas, with the petiole spot and a zone towards the south of the image against the rest of the leaf (Fig. 5.9B,E,H). Only Fig. 5.9L seems to feature a special point which might be at the boundary of the two complementary zones and thus show a singular kind of relation with the other points. This applies also for the synchronization index S($\Phi_{ij} : \Phi_{i'j'}$, where in Fig. 5.9M no synchronization is detected with any of the other pixels. The other pictures of S, exhibited in the right column of Fig. 5.9 indicate that a cluster of pixels in the middle of the leaf, around the vein is characterized by high synchronization (Fig. 5.9C,F,J). Especially the pattern of S in Fig. 5.9J is similar to the pattern seen in Fig. 5.8F.

Relations with Environmental Quantities

The relations of the Φ_{ij} with the time series of L and Δw are plotted in Fig. 5.10. The top row (A-C) shows the relation with L_k, while the bottom row features Δw_k. The columns are organized like the previous figures, i.e. showing from left to right $\overline{\Delta\varphi}$, C and S. The most striking fact is that the waveforms of Φ_{ij} are not correlated in any spot with neither L not Δw (Fig. 5.10B,E). Another intriguing finding is that the pattern seen in $\overline{\Delta\varphi}$ ($\Phi_{ij} : L$) (Fig. 5.10A) is almost identical to $\overline{\Delta\varphi}$ ($\Phi_{ij} : \hat{\Phi}$) (Fig. 5.8D). Also the synchronization pattern S($\Phi_{ij} : L$) (Fig. 5.10C) has the same structure like S($\Phi_{ij} : \hat{\Phi}$) (Fig. 5.8F). Concerning the relations with Δw , there are large areas with $\overline{\Delta\varphi}$ ($\Phi_{ij} : \Delta w$) $\approx$ 0.5 (Fig. 5.10D) . Taking into account the antiproportionalities of Φ_{PSII} and c_{ia} (Fig. 5.3A/G), and the proportionality of c_{ia} and Δw (Eq. D.3) this is expected. Interesting to notice is that the zones showing significant synchronization with Δw are phase shifted away from $\overline{\Delta\varphi}$ ($\Phi_{ij} : \Delta w$) = 0.5 (black areas). Also the different zones being linked to the petiole spot are phase shifted to give $\overline{\Delta\varphi}$ ($\Phi_{ij} : \Delta w$) $\approx$ -0.25. Synchronization with Δw occurs in the "pacemaker region" (Keener & Sneyd 1998) at the top rim of Fig. 5.10F, i.e.

the region with the oscillators showing the highest amplitudes, the fastest frequencies and largest phase advance with respect to the meanfield phase. The cross-correlations (Fig. 5.10B/E show intermediate correlation or anti-correlation, without a meaningful profile.

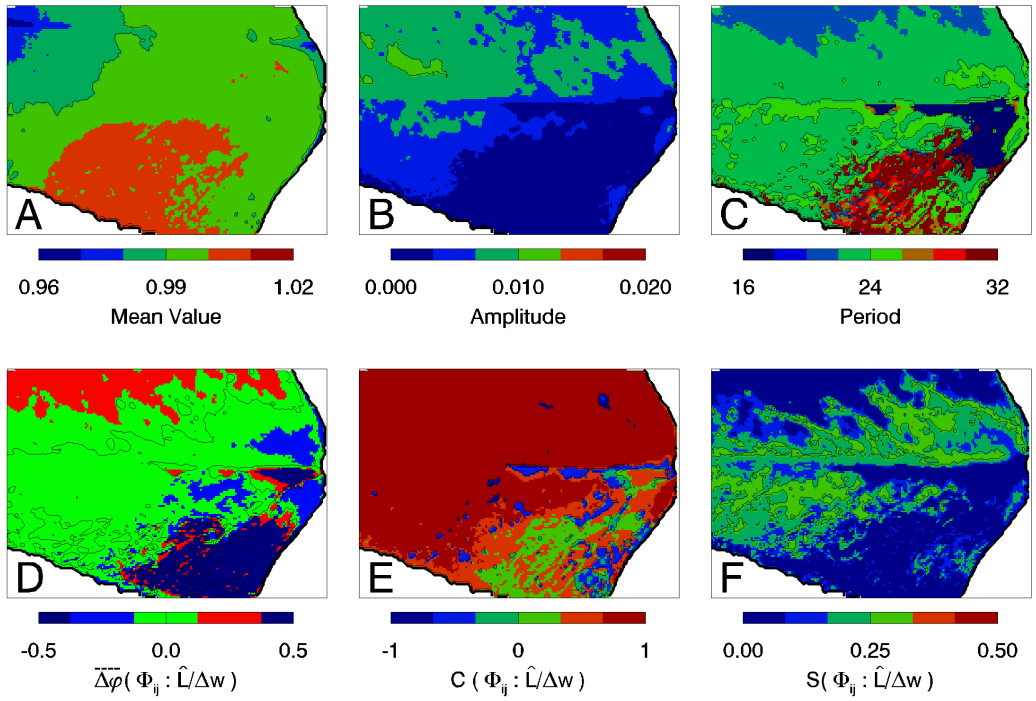

Figure 5.8: Spatial distribution of rhythm parameters of rhythmic timeseries (Fig. 5.4) and relations of individual timeseries with meanfield rhythm. **A:** Temporal average $\bar{\Phi}_{ij}$. **B:** Average amplitude $\bar{A}(\Phi_{ij})$. **C:** Dominant period τ_{ij}^{dom}). The bottom row features the relations of each single pixel with the meanfield signal $\hat{\Phi}_k$. **D:** Phase difference $\Delta\varphi(\Phi_{ij} : \hat{\Phi})$. **E:** Maximal cross-correlation $\mathrm{C}(\Phi_{ij} : \hat{\Phi})$ for a range of lags between $\pm$ 13 h. **F:** Maximal synchronization index $\mathrm{S}(\Phi_{ij} : \hat{\Phi})$ for a range of lags between $\pm$ 13 h.

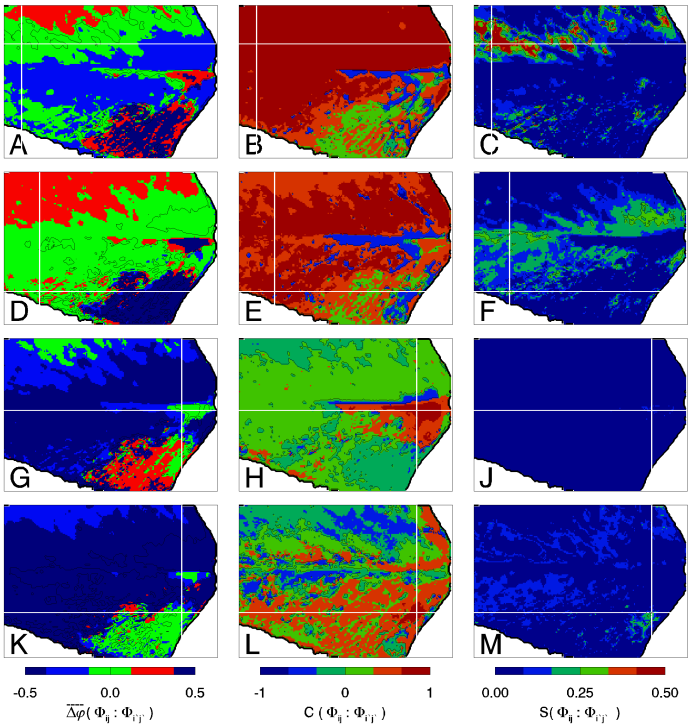

Figure 5.9: Rhythm relations between 4 arbitrarily selected pixels in rhythmic timeseries Fig. 5.4. **A**-**C**: The relations between point (16,32) and all other pixels belonging to the leaf. **D**-**F** point (32,100), **G**-**J** point (160,60) **K**-**M** point (160,90). Left column: Phase difference $\overline{\Delta\varphi}$ $(\Phi_{ij} : \Phi_{i'j'})$, with i' and j' marking the coordinates of the reference pixel. Middle column: Maximum cross-correlation $\mathrm{C}(\Phi_{ij} : \Phi_{i'j'})$. Right column: Maximum synchronization index $\mathrm{S}(\Phi_{ij} : \Phi_{i'j'})$.

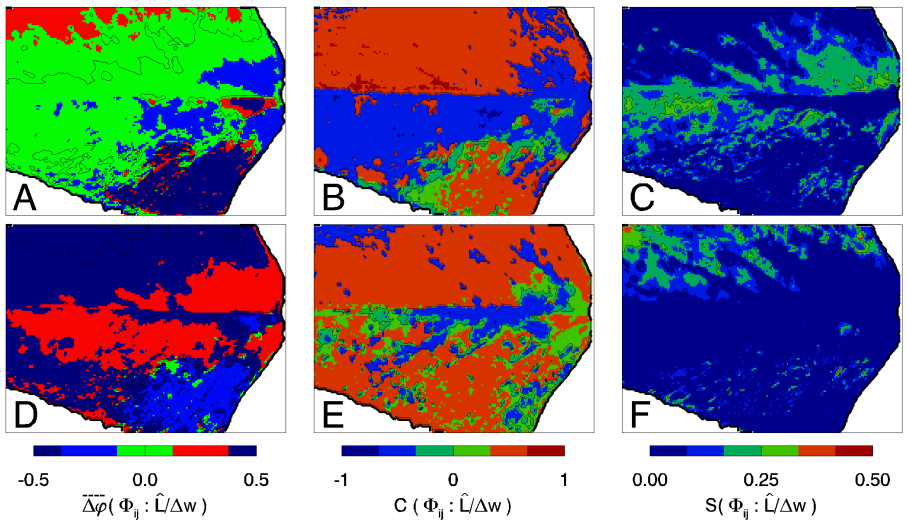

Figure 5.10: Phase relations with L and Δw for rhythmic image-series (Fig. 5.4). Top: Phase-relations with photon flux density L. **A**: $\overline{\Delta\varphi}$ $(\Phi_{ij} : L)$, **B**: $\mathrm{C}(\Phi_{ij} : L)$, **C**: $\mathrm{S}(\Phi_{ij} : L)$. Bottom, Phase relations with water vapor pressure deficit Δw . **D**: $\overline{\Delta\varphi}$ $(\Phi_{ij} : \Delta w)$, **E**: $\mathrm{C}(\Phi_{ij} : \Delta w)$, **F**: $\mathrm{S}(\Phi_{ij} : \Delta w)$

5.2.4 Discussion

The analysis of sequences of images in free-running conditions permitting rhythm expression reveals that

- rhythm damping is a local phenomenon, i.e. the damping of the whole-leaf rhythm is also observed in each individual pixel. This is quantified by the correlation of $A(\hat{Phi}_k$ and $\hat{A}(\Phi_{ijk})$ (Fig. 5.5C) and the high cross-correlation of each individual pixel with the mean field $\mathrm{C}(\Phi_{ij} : \hat{\Phi})$(Fig. 5.8E),

- spatio-temporal dynamics is caused by gradients in amplitude, mean values and frequency, which give rise to phase waves (Figs. 5.6, 5.7, 5.8),

- there are zones in the leaf, in particular the spot where the petiole meets the leaf, the dynamics of which is exempt from the gradual pattern of amplitude and phase properties observed in the rest of the leaf.

- the pattern of phase differences and synchronization between $\hat{\Phi}$ and the Φ_{ij} (Fig. 5.8D,F) correspond closely to the patterns of $\overline{\Delta\varphi}$ $(\Phi_{ij} : L)$ and $\mathrm{S}(\Phi_{ij} : L)$ (Figs. 5.10A,C), and

- patches of high synchronization with Δw coincide with a "pacemaker region" (Keener & Sneyd 1998) consisting of the oscillators with the highest dominant frequencies and the largest phase advance with respect to the average population

In fact, the investigated image series is the one that has been featured in (Rascher et al. 2001). There the data were analyzed with a measure of heterogeneity based on cellular automata techniques (Hütt & Neff 2001), which showed onsetting oscillating heterogeneity as of 2 days in LL. This dynamical heterogeneity measure detects both the patch of cells in the lower half of the leaf, which show very slow oscillations Fig. 5.8C, as well as the dynamical structure resulting from the spreading and shrinking of the area of low Φ_{PSII} with a circadian rhythm. The course of the timeseries of heterogeneity can be explained from the findings of this section: the slow patches of the lower leaf half come to rest at a low level of Φ_{PSII} . At times the dynamically spreading and shrinking region of low Φ_{PSII} is extended, the heterogeneity drops, and increases when this region recedes again.
The crucial question being raised from these findings is the origin of the heterogeneity. There is a number of arguments in favor of a gradient in light intensity.

- Φ_{PSII} is proportional to J_c and anti-proportional to c_{ia} (Fig. 5.3A,D,G). This means the region of low Φ_{PSII} represents higher concentrations of internal CO_2 , which would be favored by lower L in that region (cf. Chapter 2.1). It should be noted that an in-depth discussion of this phenomenon will have to take into consideration the exact phase-relations of the three considered quantities.

- The region of lowest Φ_{PSII} shows higher amplitudes than the rest of the leaf (Fig. 5.8A/B). In the whole-leaf rhythm this is favored by reduced light intensity (Buchanan-Bollig 1984).

- In this scenario, the patches which according to Rascher et al. (2001) come to rest earlier would be exposed to higher light intensity. Taking into account that an average L of 192 μE m^{-2}s^{-1} is rather high and close to the transition value for arrhythmicity, the rhythm stopping in that part of the leaf could be induced by the local L attaining arrhythmic values. This is also in concordance with the observation, that in leaf exposed to lower light intensities (120 μE m^{-2}s^{-1} , data not shown) this kind of heterogeneity based on local rhythm stopping is not observed.

An important role for L in the formation of patterns is also suggested by the fact that the patches of high S($\Phi_{ij} : \Phi_{i'j'}$) as well as S($\Phi_{ij} : \hat{\Phi}$) Figs. 5.9C,F,J/5.8F coincide with the patches of high S($\Phi_{ij} : L$) (Fig. 5.10C). Remembering the definition of synchronization, which states the requirement of two autonomously oscillating systems, this implies that there might be a significant contribution of a frequency in the circadian range in the spectrum of L. The spatio-temporal dynamics observed here could thus be phenotypical for an oscillatory medium which is driven by a driver with spatially heterogeneous amplitude and mean value. This hypothesis, which gives a consistent description of the observed spatio-temporal dynamics will have to be checked for in future experiments, taking explicit control of the distribution of light intensity on the leaf, as well as its temporal characteristics.
Another interesting point are the patches of synchronization with water vapor pressure deficit (Δw) and their appearance in a region of the leaf where the highest amplitudes and the fastest and earliest oscillation of Φ_{PSII} are observed. If there is a strong signal for the stomata, given by large amplitudes of internal CO_2 oscillations, also transpiration will oscillate with high amplitude, eventually imposing a cyclic variation on Δw . A significant S($\Phi_{ij} : \Delta w$) could be caused by the fact that it is this region which mostly contributes to variations in global Δw . This would not be synchronization in the original sense, but rather a causal phase relation (the phase of Δw being generated by strong, rhythmic transpiration in that area), which is constant over time. This aspect will be further discussed in Chapter 7.1
Closing this section from the point of view of the prototype models discussed in Chapter 4, the findings of this section suggest that noise could be a factor that influences the phase relations of the population Fig. 5.5C. However, the fact that there is a significant correlation of local timeseries with a global signal, which is subject to spatial heterogeneity, are more closely described by heterogeneous DLC dynamics than noisy FHN dynamics.

5.3 Arrhythmic Conditions

Analyzing spatio-temporal dynamics in the arrhythmic regime with the same protocol as the preceding rhythmic series should deliver relevant information considering whether arrhythmicity is due to the phase decoherence of spiking noisy oscillators, or a deterministic damping of local oscillations. The selection of some individual timeseries from the leaf (Fig. 5.11) already indicates that again DLC dynamics are apparently closer to experimental reality, as no large-amplitude oscillations are observed.

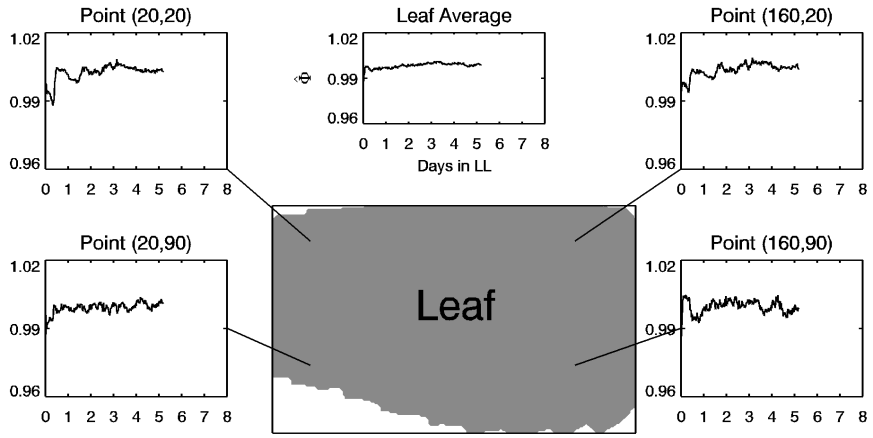

Figure 5.11: Dynamics of four points of four individual pixels of the arrhythmic timeseries (T_L =28^{o}C, L= 201 μE m^{-2}s^{-1}). In the top center the spatial average $\hat{\Phi}$ is plotted, while to the left and right, the individual timeseries are plotted. Lines link the individual plot to their location in the leaf.

5.3.1 Population Statistics

The population statistics exhibited in Fig. 5.12 underline the hypothesis of locally quenched oscillations, as is seen in subfigure C. While the amplitude of the average is zero throughout, the average amplitude is somewhat higher but still much below the value observed for the rhythmic regime (Fig. 5.5C). Phase dispersal (grey line) is less than 1, and shows an interesting time-course which significantly decreases with time. The shortness of the timeseries however does not allow a detailed discussion of this phenomenon. There is evidence that frequency heterogeneity could play a role in the phase scatter, as the distribution of dominant frequencies (Fig. 5.12B) shows two peaks: one close to one cycle/day and the other at an infradian frequency < 0.5 cycles/day. These peaks are also found in the spectrum of $\hat{\Phi}$ (Fig. 5.12B).

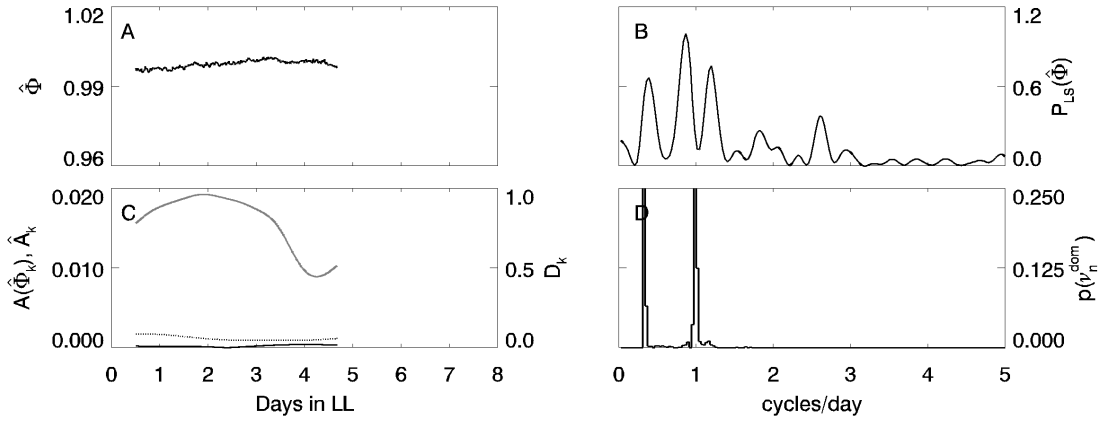

Figure 5.12: Population statistics of the timeseries of Fig. 5.11. **A:** Meanfield rhythm ($\hat{\Phi}$), **B:** Normalized powerspectrum of $\hat{\Phi}$. **C:** Amplitude of average (A($\hat{\Phi}$), solid black line), average amplitude ($\hat{A}(\Phi_{ij})$, dotted black line) and population phase scatter (D_k, grey line). **D:** Distribution of dominant frequencies in population ($p(\nu_{ij}^{dom})$).

5.3.2 Spatiotemporal Dynamics

Snapshots

Heterogeneity is also observed in snapshots of this arrhythmic series of images (Fig. 5.13), yet the gradients observed are not as steep as seen in the rhythmic series Fig. 5.6. The upper half of the leaf does not show any patterns at all, while the area of the leaf vein shows lower values of Φ_{PSII} . There are no coherent patterns in the observable amplitude dynamics.

Passing to the phase dynamics that can be observed in the leaf during a course of 48 h (Fig. 5.14), there is a pronounced difference between the upper and the lower half of the leaf. The most striking observation is that they are separated by a phase difference of about 0.5 cycle. Also, the upper half shows very quick phase advances over almost the whole half of the leaf, which is indicated by a simultaneous change of color everywhere. In the lower part however, there is again evidence for the spread of phase-waves, starting at the left part of the vein and some isolated points in the middle of the lower leaf-half.

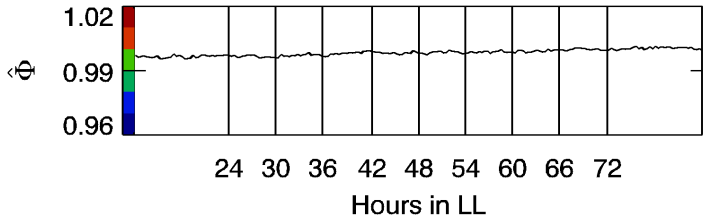

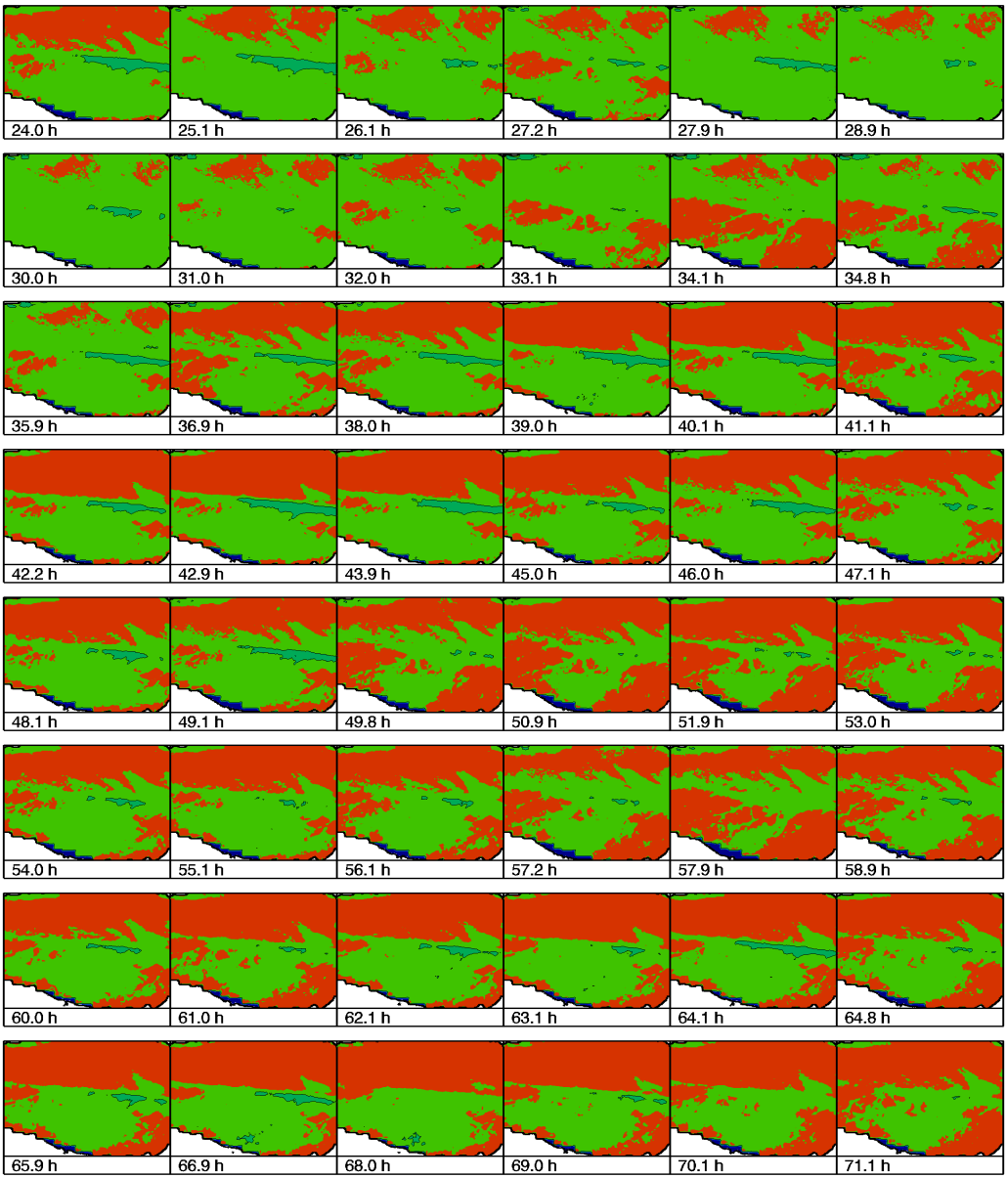

Figure 5.13: Snapshots of Φ_{ijk} of the arrhythmic timeseries shown in Fig. 5.11,5.12. **Top:** $\hat{\Phi}$ for a time-section between 0 and 96 h in LL. Vertical bars mark the times of leftmost image in each row of snapshots. The color bar gives the coding for the snapshot images. **Bottom:** Series of snapshots of Φ_{ij}. Images range times from 24 - 71 h in LL, with a time of $\approx$ 1 h between each image.

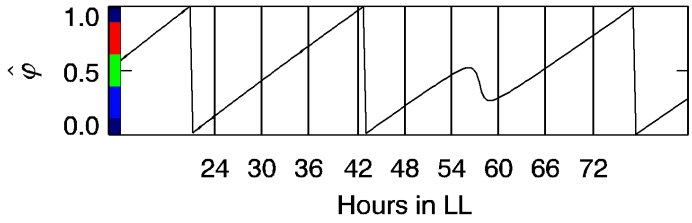

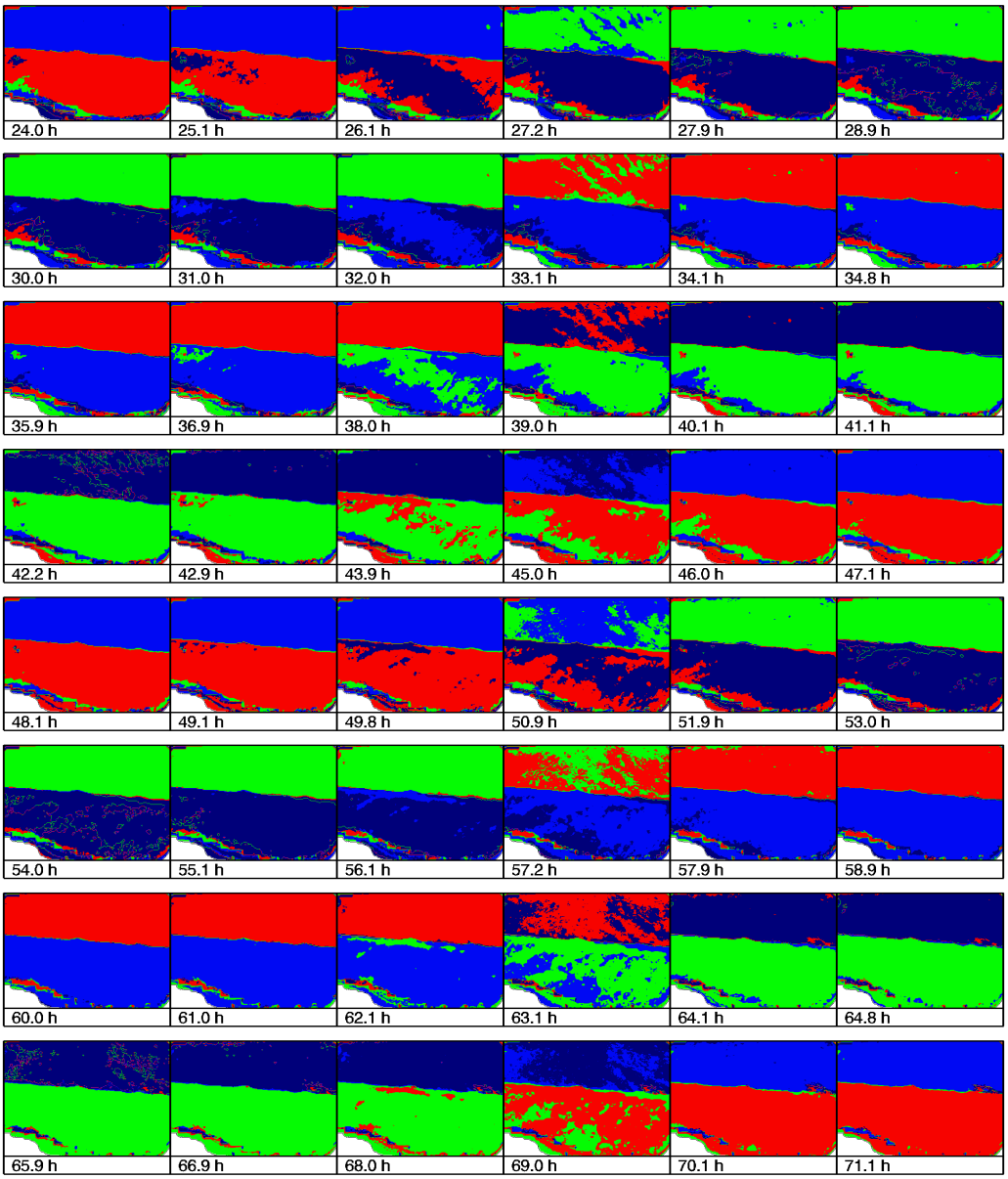

Figure 5.14: Snapshots of $\varphi(\Phi_{ijk})$ of the arrhythmic timeseries Fig. 5.4. **Top:** $\varphi(\hat{\Phi})$ for a time-section between 0 and 96 h in LL. Vertical bars mark the times of the leftmost image in each row of snapshots. The color bar gives the coding of the snapshot images. **Bottom:** Series of snapshots of $\varphi(\Phi_{ij})$. The times of snapshots are identical to Fig. 5.13 and range from 24 - 71 h in LL, with a time of $\approx$ 1 h between each image.

Spatial Distribution of Rhythm Parameters

The spatial distribution of rhythm parameters exhibited in Fig. 5.15 confirms the preceding statements of this section. The image of $\overline{\Phi}_{ij}$ (A) shows a slight heterogeneity as was also observed in the snapshots, and as stated before, amplitudes are vanishing in the entire leaf (B). The separation of characteristics between the upper and lower half of the leaf persists also for the dominant frequencies (C), and gives an explanation for the bimodal distribution of frequencies seen in Fig. 5.12D: while the lower half shows oscillating points with mostly periods of around 24 h, the upper half shows dominant infradian oscillations with periods longer than 30 h (C).
The large difference in periods within the image makes it difficult to discuss average phase differences, as the phase difference cannot be constant in time. This must be born in mind, when considering $\overline{\Delta\varphi}(\Phi_{ij} : \hat{\Phi})$ (Fig. 5.15D), which shows the upper half being on average about 0.25 τ ahead of $\hat{\Phi}$, while the lower half trails about 0.25 cycles behind. Except for a spot of high anti-correlation in the lower half, the waveforms of the Φ_{ijk} are highly correlated with $\hat{\Phi}$, suggesting that arrhythmicity is a local phenomenon and not an emergent effect only visible at the macroscopic level. In spite of the high values of $\mathrm{C}(\Phi_{ij} : \hat{\Phi})$ throughout the leaf, the synchronization index $\mathrm{S}(\Phi_{ij} : \hat{\Phi})$ does not have a significant value in any point (i,j).

5.3.3 Rhythm Correlations

Relations between Leaf Pixels

From the observed spatio-temporal dynamics one could expect significant differences in the phase relations of the upper and the lower half of the leaf. The phase difference between the leaf pixels as shown in the left column of Fig. 5.16 are indeed a confirmation of the results seen so far: reference points in the lower half (G,K), are in-phase with the lower part and 0.5 cycles out-of-phase with the upper part and vice-versa (A). Interesting to see in Fig.5.16D is that the lower rim of the leaf is obviously in phase with the upper half. The same separation of upper and the lower part is slightly apparent in $\mathrm{C}(\Phi_{ij} : \Phi_{i'j'})$ (Figs. 5.16B,E,H,L). As expected, there is significant synchronization between reference points in the lower half, and a large zone of other pixels exclusively in the lower half (Fig. 5.16J,M). Given a reference point in the upper half, the most significant synchronization is also observed with points in the upper half (5.16C).

Relations with Environmental Quantities

The preceding Section 5.2 dealing with a rhythmic timeseries showed a significant influence of light intensity. As a matter of fact, this is also the case for the arrhythmic timeseries considered here. Figure 5.17C shows that the synchronization index $\mathrm{S}(\Phi_{ij} : L)$ has the same spatial distribution as $\mathrm{S}(\Phi_{ij} : \Phi_{i'j'})$ in Fig. 5.16J,M: there is a high synchronization

between the points in the lower half of the leaf, as well as between the pixels of the lower half and L. Interestingly, the phase of L locks to the lower-half Φ_{ijk} in counter-phase, as is seen in Fig. 5.17A. The differences in $\overline{\Delta\varphi}$ $(\Phi_{ij} : L)$ between the upper and the lower half are only 0.25.
There is the separation of the leaf halves in the correlation with L, though values are not close to $|1|$ 5.17B, and the correlation of Δw with Φ_{ijk} (Fig. 5.17E) is high but without any specific pattern. Significant synchronization with Δw (Fig. 5.17F) is not given.

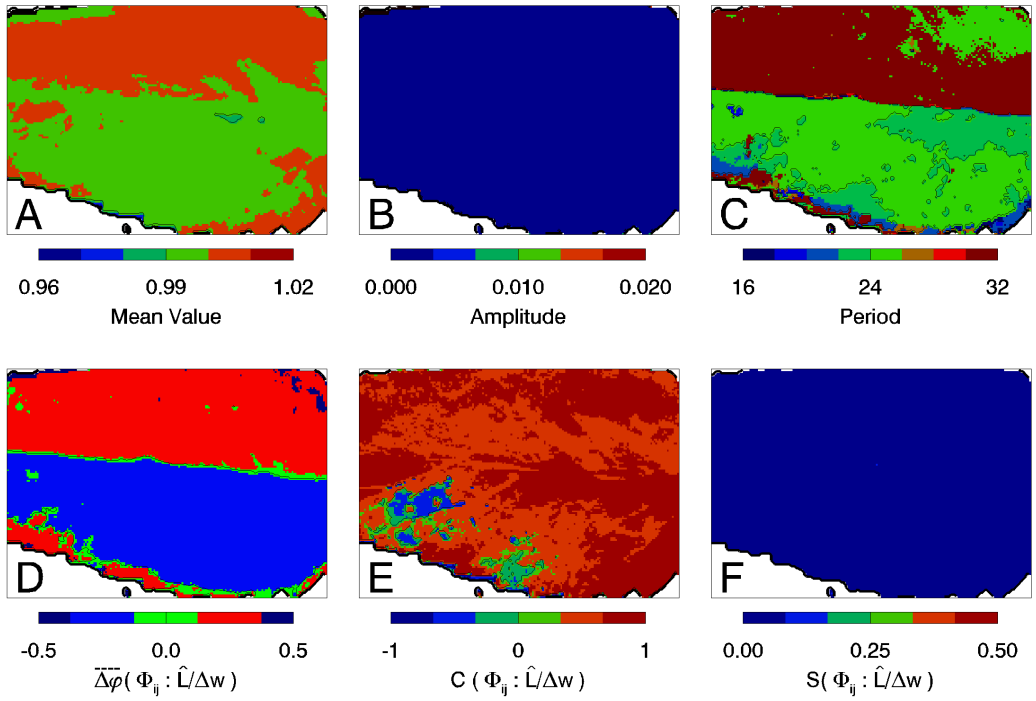

Figure 5.15: Spatial distribution of rhythm parameters of arrhythmic timeseries (Fig. 5.11) and relations of individual timeseries with meanfield rhythm. **A:** Temporal average $\bar{\Phi}_{ij}$. **B:** Average amplitude $\bar{A}(\Phi_{ij})$. **C:** Dominant period τ_{ij}^{dom}. The bottom row features the relations of each single pixel with the meanfield signal $\hat{\Phi}$. **D:** Phasedifference $\Delta\varphi(\Phi_{ij} : \hat{\Phi})$. **E:** Maximal cross-correlation $C(\Phi_{ij} : \hat{\Phi})$ for a range of lags between $\pm$ 13 h. **F:** Maximal synchronization index $S(\Phi_{ij} : \hat{\Phi})$ for a range of lags between $\pm$ 13 h.

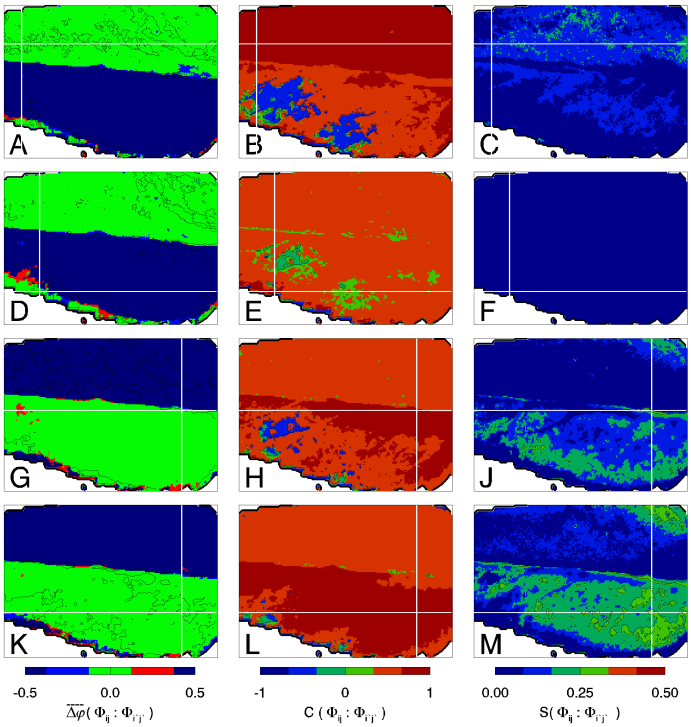

Figure 5.16: Rhythm relations between 4 selected pixels in arrhythmic timeseries Fig. 5.11. **A**-**C**: The relations between point (16,32) and all other pixels belonging to the leaf. **D**-**F** point (32,100), **G**-**J** point (160,60) **K**-**M** point (160,90). Left column: Phase difference $\overline{\Delta\varphi}$ $(\Phi_{ij} : \Phi_{i'j'})$, with i' and j' marking the coordinates of the reference pixel. Middle column: Maximum cross-correlation $C(\Phi_{ij} : \Phi_{i'j'})$. Right column: Maximum synchronization index $S(\Phi_{ij} : \Phi_{i'j'})$.

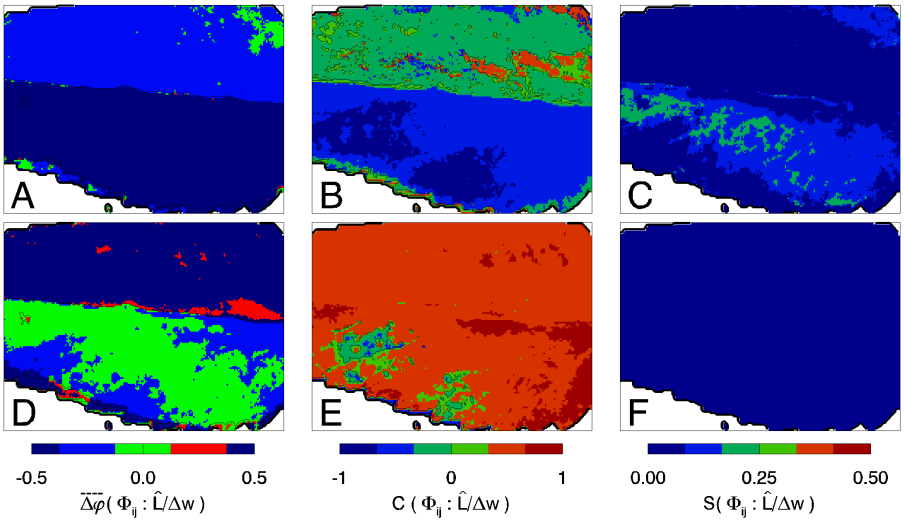

Figure 5.17: Phase relations with L and Δw for rhythmic image-series (Fig. 5.11). Top: Phase-relations with photon flux density L. **A:** $\overline{\Delta\varphi}$ $(\Phi_{ij} : L)$, **B:** $C(\Phi_{ij} : L)$, **C:** $S(\Phi_{ij} : L)$. Bottom, Phase-relations with water vapor pressure deficit Δw . **D:** $\overline{\Delta\varphi}$ $(\Phi_{ij} : \Delta w)$, **E:** $C(\Phi_{ij} : \Delta w)$, **F:** $S(\Phi_{ij} : \Delta w)$

5.3.4 Discussion

The main results of this section are summarized in the following:

- Arrhythmicity and low amplitudes are also local phenomena. Neither in the amplitude snapshots (Fig. 5.13), nor in the statistical and pixel-wise analysis of the individual oscillators (Figs. 5.12C, 5.15B) there are signs for noise-induced spikes with amplitudes comparable to the rhythmic regime. Rather the waveform of the mean-field is correlated to the waveforms of all the individual pixels (Fig. 5.15E).

- There is a significant heterogeneity of frequencies, as there are clusters of oscillators with a dominant period in the circadian range, while other parts of the leaf are showing infradian oscillations. In this particular case, the regions are separated by the vein (Fig. 5.15C).

- The zone which shows predominantly circadian oscillations coincides with the region showing synchronization with light intensity (Fig. 5.17C). There is also a significant degree of synchronization between the individual pixels of this region (Fig. 5.16J,M).

- No significant relation of Φ_{ijk} with Δw is observed (Figs. 5.17D-F).

Returning to the central question of the origin of a circadian contribution to the spectrum of arrhythmic gas-exchange, no support for the hypothesis of a noise-driven excitable medium is found from an analysis of the present experiments. Another investigated image-series (data not shown) yields the same conclusions. The fact that amplitudes remain quenched in comparison to the rhythmic regime throughout the entire leaf, and that phase dynamics show a certain spatial order, rule out a description of circadian CAM by noise-driven FHN-type oscillators.
Circadian oscillations in the arrhythmic regime could emerge from either an internal clock, corresponding to a DLC oscillator with a quenched amplitude but continuing phase evolution, or could be due to a circadian component in light intensity. The aspect of a modulated light intensity has already been discussed in the context of the rhythmic image series, and the evidence found here suggests also an important role for the dynamics in the arrhythmic regime. In fact, it is intriguing to notice that those areas exhibiting circadian oscillations are synchronized with L. One aspect which must not be forgotten in this discussion is that the considered timeseries is relatively short. While the main aspect, i.e. the quenching of the amplitude appears to be a robust phenomenon, particular details like, e.g. the double-peaked frequencies might be artefacts of the shortness of the present timeseries.
The question of exogenous influences on the circadian rhythm of J_c in CAM remains an interesting topic and will be recaptured in Chapters 6 and 7.

5.4 Slow and Fast Temperature Changes

As stated in the introduction and in Chapter 4.3, one of the motivations to speculate about the multi-oscillator nature of the circadian rhythm of CAM was the result of experiments by Rascher et al. (1998), showing that rhythm re-initiation only occurs after fast reductions of T_L from 28^o to 21^{o}C, not after slow ones. These temperature protocols (here between 31^{o}C and 24^{o}C) have also been applied to leaves being monitored with the fluorescence camera (Rascher 2001). The observed phenomenon could not be reproduced, as in most cases the rhythm reappeared also for a slow temperature reduction.
Figure 5.18 shows the timeseries of Φ_{PSII} for four selected pixels in the leaf. Visual inspection of the timeseries shows that there is no homogeneous reaction to the fast temperature pulse given at 6.5 d in LL. While in point(10,40) there is a clear reaction, the other points show only a minimal drop of Φ_{PSII} . Interesting to notice are also spontaneous drops of Φ_{PSII} , which last for about one day, and occur only when the plant is at 24^{o}C, e.g. in point (10,90) at 7.5 d in LL. The comparisons of Φ_{PSII} and c_{ia} in Chapter 5.1 showed that low values of Φ_{PSII} correspond to high internal CO_2 concentrations. If this proportionality still applies, these negative bursts could emerge from an increase of c_{ia} due to malic acid release.

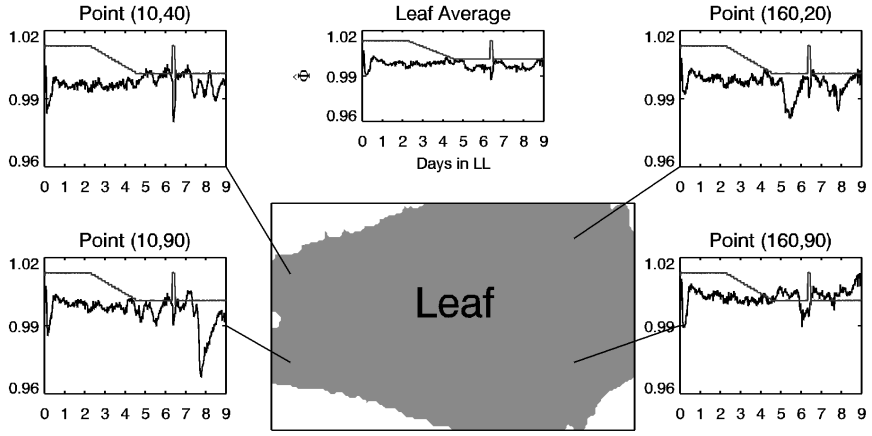

Figure 5.18: Dynamics of four points of four individual pixels of an image series in continuous light (L= 140 μE m^{-2}s^{-1}) and with a temperature protocol of slow and fast reductions from 31 to 24^o C (T_L given by the grey line). In top center the spatial average $\hat{\Phi}$ is plotted, while to the left and right, the individual timeseries are plotted. Lines link the individual plot to their location in the leaf.

These unsteady dynamics, exhibiting steady-state behavior for long intervals of time (e.g. at 31 ^{o}C) being interrupted by sudden bursts, and being subject to a dynamical T_L , make it extremely hard if not impossible to get any meaningful information out of a phase analysis, as a non-arbitrary estimation of a point of reference for phase calculation is extremely intricate for the given data. That is why in this section the discussion of the data is reduced to the consideration of series of snapshots of the Φ_{ijk} .

5.4.1 Snapshots

Figure 5.19 shows a series of snapshots during the slow temperature-descent. The first image is given at 48 h in LL and 31^{o}C, the last image at 142 h in LL and 24^{o}C. The time-interval between the snapshots is $\approx$ 2 h. In the first images, at high T_L , the pattern of Φ_{ij} is similar to the one observed in the arrhythmic regime (Fig. 5.13): there are slight variations in space, however no coherent dynamics can be spotted by visual inspection. As T_L is reduced, the structure of the vascular system of the leaf starts to dominate the pattern, with increased Φ_{PSII} being observed along the central vein and other veins bifurcating from it. Especially at 94.2 h and 109.9 h in LL this is obvious. When T_L has reached the low level of 24^{o}C, at 120 h in LL, Φ_{PSII} starts to drop significantly in a zone at the top rim of the leaf. Different to the images seen for the rhythmic timeseries (Chap. 4.2) there is no rhythmic expansion of this area of low Φ_{PSII} . The cluster reaches its maximum size at about 124 h in LL and remains constant in size for $\approx$ 8 - 10 h, before Φ_{PSII} diminishes again. A smaller zone at the bottom rim of the leaf exhibits the same dynamics. As has been discussed in Fig. 5.18, it is reasonable to assume that this dynamics is caused by malic acid release from the vacuole. In this case, this process seems to be the strongest in cells at the rims of the leaf.
Figure 5.20, continues the snapshot series of Fig. 5.19, and features snapshots of Φ_{ijk} at 24^{o}C , with a short pulse of 31^{o}C given for about 4 h, starting at 152 h in LL. The snapshots start at 120 h in LL, and again, time increments by $\approx$ 2 h between each snapshot. The first snapshots show the appearance of the low-Φ_{ijk} cluster as discussed before. At 154.2 h and 31^{o}C there is another drop in Φ_{ijk} visible, which is induced by the temperature pulse. There will be a series of snapshots with a higher time-resolution in Fig. 5.21 exhibiting the effects of temperature change in more detail. As for Fig. 5.20, it is important to notice that the spatio-temporal dynamics have only been transiently affected by the temperature pulse. At about 174 h in LL, another cycle of Φ_{PSII} decrease starts in exactly the same points as was observed before the T-pulse. At most, a phase-shift has been introduced to each single oscillator, so that the appearance of the low-Φ_{PSII} cluster has been shifted in time but not in space.
Figure 5.21, takes a closer look at the spatio-temporal dynamics being induced by the T-pulse. The series starts at 144 h in LL and exhibits each image that was recorded (δt = 20 min). Clearly, the temperature increase provides a decrease of Φ_{PSII} in almost the entire leaf. Especially in the upper half, the formation of a large cluster of low Φ_{PSII} is obvious. This could be caused by the release of malic acid from the vacuole, which according to the CAM model is induced by high temperatures. Still in the regime of T_L = 31^{o}C, the values in the cluster of low Φ_{PSII} raise again. The temperature down-step does not provide a similar emergence of clusters of high Φ_{PSII} , except for the area of the leaf vein, where Φ_{ijk} is raised for about 2 h.

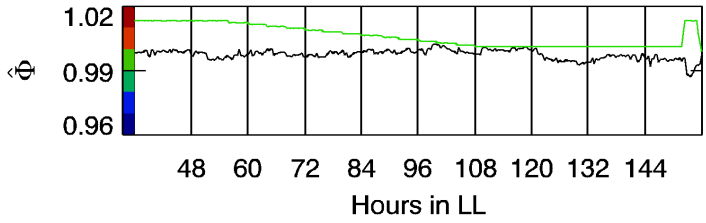

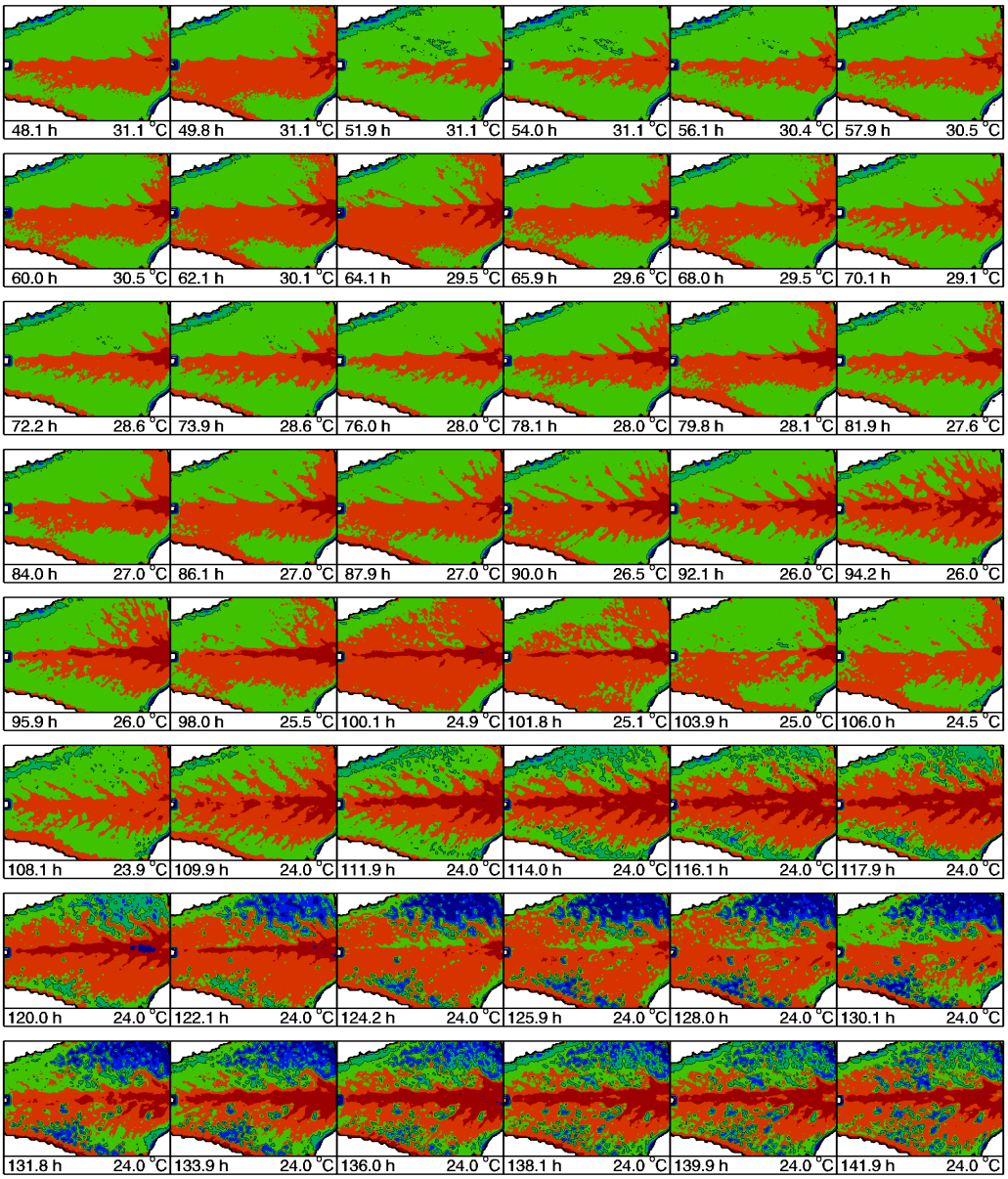

Figure 5.19: Snapshots of Φ_{ijk} of the image-series Fig. 5.18 during slow temperature reduction from 31^{o}C to 24^{o}C. **Top:** $\hat{\Phi}$ for a time-section between 24 and 168 h in LL. The green line represents leaf temperature. Vertical bars mark the times of the leftmost image in each row of snapshots. The color bar gives the coding of the snapshot images. **Bottom:** Series of snapshots of Φ_{ij}. The times of snapshots range from 48 - 143 h in LL, with a time of $\approx$ 2 h between each image. The actual leaf-temperature T_L is also given in each snapshot.

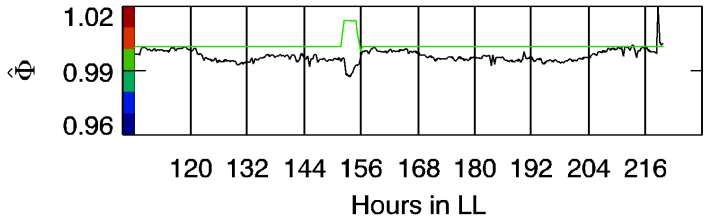

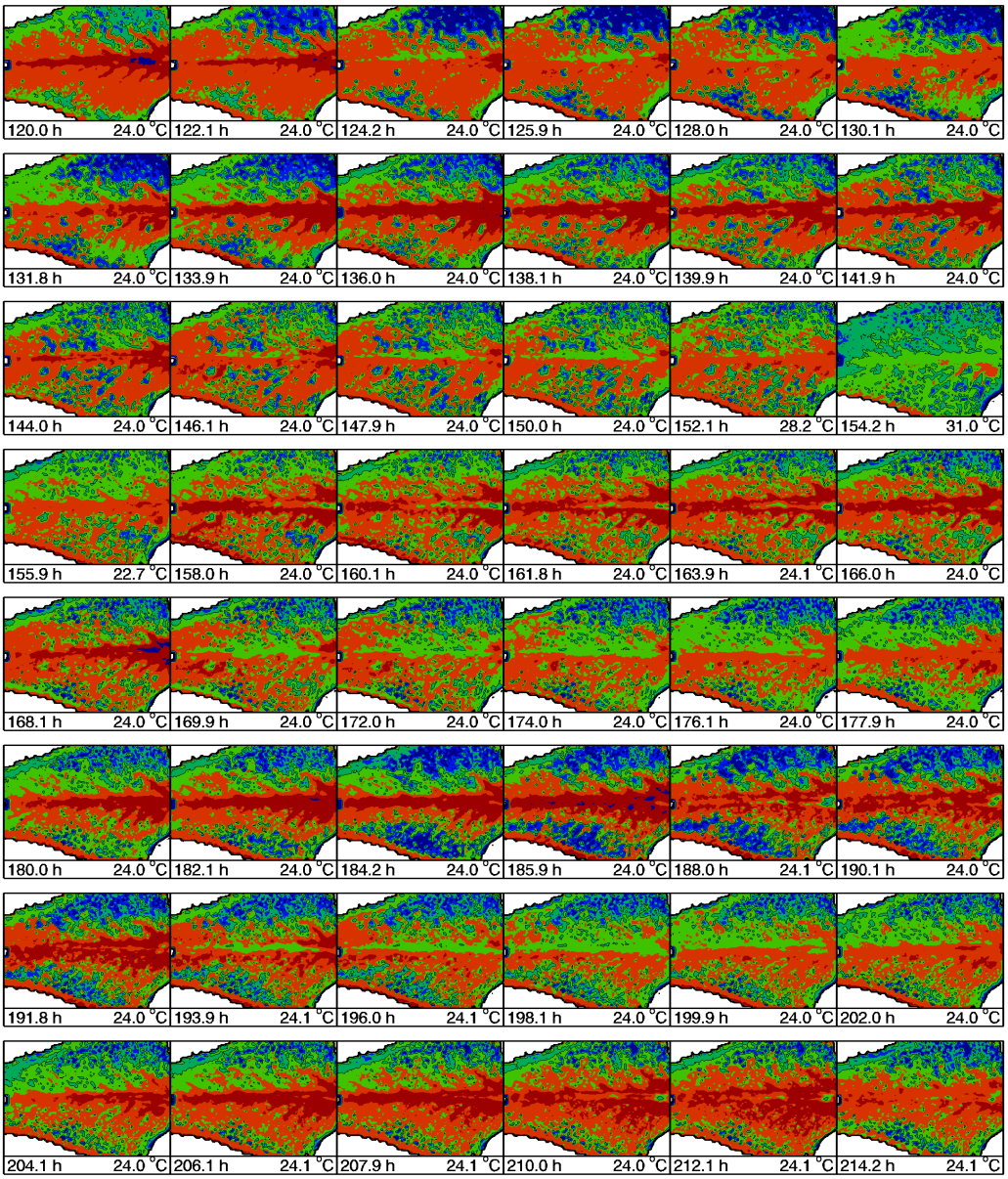

Figure 5.20: Snapshots of Φ_{ijk} of the image-series Fig. 5.18 for constant T_L of 24^{o}C with one temperature pulse in between. **Top:** $\hat{\Phi}$ for a time-section between 96 and 228 h in LL. The green line represents leaf temperature. Vertical bars mark the times of the leftmost image in each row of snapshots. The color bar gives the coding of the snapshot images. **Bottom:** Series of snapshots of Φ_{ij}. The times of snapshots range from 120 - 210 h in LL, with a time of $\approx$ 2 h between each image. The actual leaf-temperature T_L is given in each snapshot.

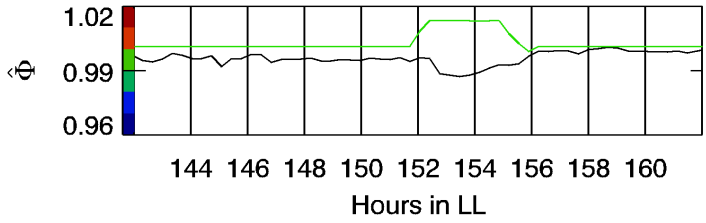

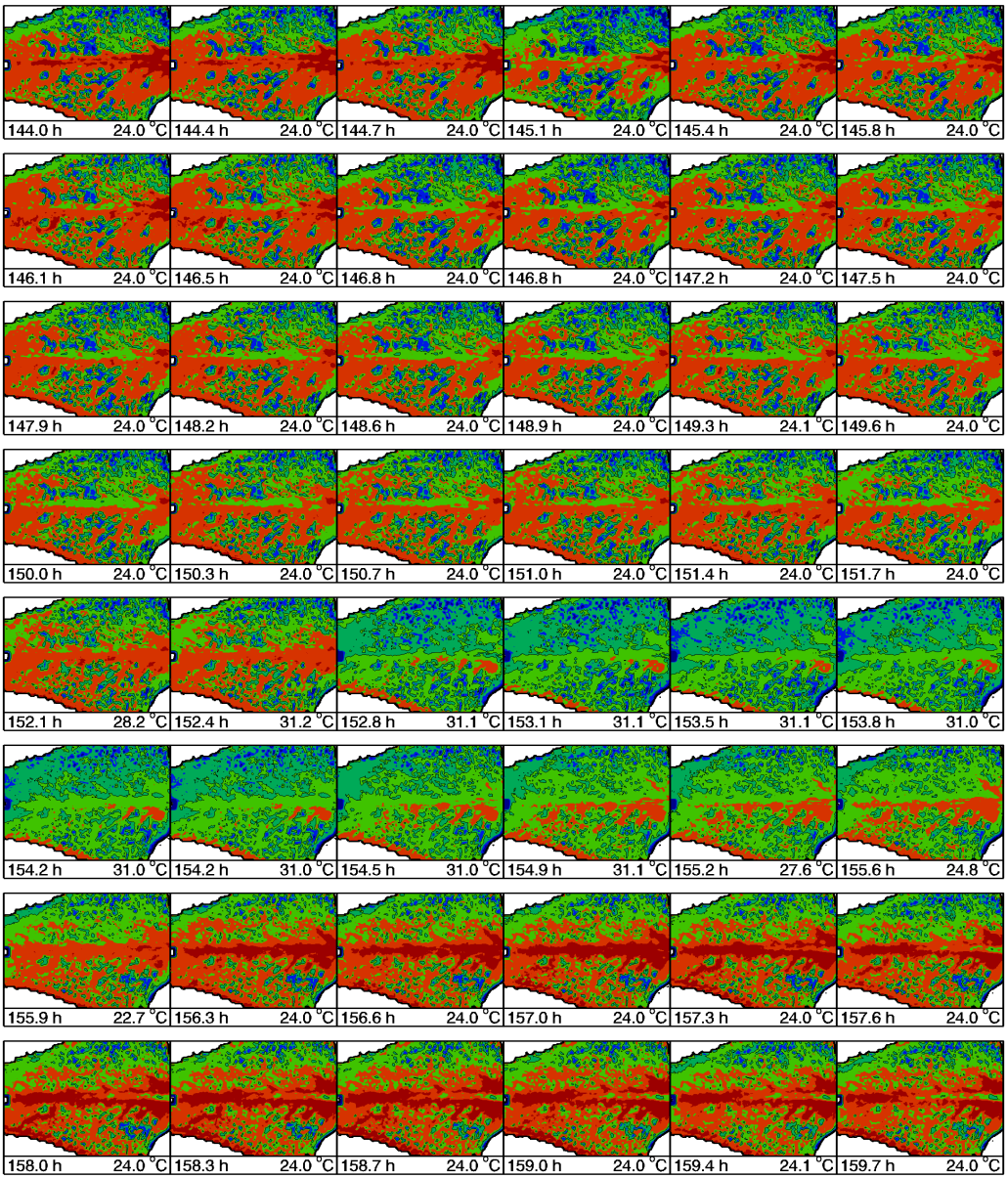

Figure 5.21: Snapshots of Φ_{ijk} of the image-series Fig. 5.18 before and after the temperature pulse, with exhibition of each recorded image. **Top:** $\hat{\Phi}$ for a time-section between 142 and 162 h in LL. The green line represents leaf temperature. Vertical bars mark the times of the leftmost image in each row of snapshots. The color bar gives the coding of the snapshot images. **Bottom:** Series of snapshots of Φ_{ij}. The times of snapshots range from 144 - 160 h in LL, with a time of $\approx$ 20 min between each image. The actual leaf-temperature T_L is given in each snapshot.

5.4.2 Discussion

Unlike in the scenarios of Chapters 5.2 and 5.3, it is not possible to extensively compare the theoretical predictions with the experimental data, as the temperature-change experiments themselves do not show the features that were observed earlier (Rascher et al. 1998). However a few speculations about the dynamics under slow- and fast temperature changes may be derived from the available data.
According to the simulations of a population of excitable oscillators, the reason why the rhythm is re-initiated by fast changes in temperature, but not by a slow transition, is purely attributed to the collective phase dynamics of the populations of oscillators, which is scattered by noise and/or different intrinsic frequencies. Thus only a fast transition from the fixed-point back to limit cycle oscillations results in a high amplitude of the collective oscillation. Like in the previous two sections, there is no hint in the data investigated here, that would support the scenario of a noise driven excitable-medium. In fact, the temperature changes seemingly affect the amplitudes of the individual rhythms, but not the phase scatter of the population. As is depicted in the snapshots shown in Fig. 5.19, there is a re-appearance of high-amplitude oscillations in some patches of the leaf. Yet, the patches in themselves are homogeneous in their phases, as Φ_{PSII} drops at the same instant throughout the cluster. Also, the temperature pulse has immediate effects on the amplitudes of single points in the leaf, but there are no signs for an altered phase dynamics (a reduced phase scatter) with the amplitudes remaining unaffected.
This finding joins the results of Chapters 5.2, 5.3 in that the properties of the collective rhythm are also reflected in the dynamics of each single oscillator, and that heterogeneity rather than the constructive influence of noise are an issue in the population dynamics of CAM leaf tissue. Focusing on the heterogeneity observed in the images of this section, there are some significant differences in the general spatial structure of Φ_{ij}. Here, the leaf is repleted with small-scale structures, which might be connected to the anatomy of the vascular system. Structures of the vascular system have also been observed in the former imageseries. However there they were submerged to more long-range patterns the dynamics of which extended over vast parts of the leaf. Here these long-range, gradual changes in amplitude, mean value, and dominant frequency are missing, and only the branched small-scale patterns are prominent. It may thus be speculated that the dependence of the re-initiation of the global rhythm on the velocity of temperature reduction could be linked to the presence of a certain type of (large-scale) heterogeneity. This aspect is further discussed in the following conclusions of this chapter.

5.5 Conclusions

The analysis of the spatio-temporal dynamics of photochemical efficiency in leaves of *Kalanchoë daigremontiana* departed from the prediction of two alternative scenarios which

both could explain important features of the whole-leaf rhythm (Chapter 4). One is a noise-driven excitable medium, the other one a heterogeneous oscillatory medium, the main difference between the two being that the individual oscillations do not correlate with the global rhythm in the case of the noise-driven excitable medium, i.e. rhythm damping and arrhythmicity are considered as phenomena which can only be understood as collective effects of the population under random influences.

Stochastic Excitable Medium vs. Deterministic Oscillatory Medium

In all three experimental protocols examined in this chapter, no signs in favour of the noise-driven excitable medium could be found (Chapters 5.2.4, 5.3.4, 5.4.2). Rather, in all three experiments there is a clear correlation between the global and the local rhythms showing that a circadian component of arrhythmicity, rhythm damping and the response to temperature changes are all seen in each individual point of the leaf.
This central finding is in accordance with earlier experiments, where stimulus-induced rhythmicity and arrhythmicity in the population of oscillating petals of *Kalanchoë blossfeldiana* were believed to be due to stimulus-induced phase scattering and resetting, but turned out to be phenomena with are exposed by each single oscillator (Engelmann et al. 1978). Similar facts, supporting the role of individual amplitude resetting instead of population phase resetting also prevail in populations of the fruit fly *Drosophila* (Winfree 2001), hence, they seem not to be limited to plants.
These observations of the dynamics call for a reconsideration of the physiology of the CAM model, now that there is evidence that rhythm damping is a phenomenon which must be included also in the single oscillator of CAM. More evidences with respect to this question will be gathered in Chapter 7.

Noise and Heterogeneity

As no kind of threshold dynamics are observed in the present data, also noise is not found to play a constructive or otherwise decisive role (see Chapter 2.1). A more crucial role for the understanding of the spatio-temporal dynamics is suggested for the heterogeneity of the oscillators' rhythm properties.
There are two types of deviations from homogeneity in the leaf, both of which give rise to patterns in the amplitude, mean value and period of the oscillations. One type is linked to the vascular system, in particular the middle vein of the leaf. Influences could be given by the fact that in these areas, there are less photosynthesizing cells, which might influence the chlorophyll signal being integrated over the depth of the leaf. The other type of heterogeneity is of a gradual nature and extends over wide parts of the leaf, e.g. the gradients in Chap. 5.2, or the entire half of the leaf in Chapter 5.3. This gradual pattern of heterogeneity creates pacemaker regions, being a source of running phase-waves, which - most visible in the rhythmic regime - appear as dynamically expanding and contracting

areas of low Φ_{PSII} .
Speculations about the origin of this heterogeneity point towards a gradient in light-intensity. This is a plausible assumption, as light intensity is hard to be equalized all over the bended leaf surface. Furthermore the geometry of the experimental set-up forces different angles between the incident light, the leaf surface and the viewing direction of the camera. And to give a final evidence, it is known that light intensity has a strong impact on amplitude, mean value and period of circadian oscillations, especially in photosynthetic organisms (see Chapter 2.2). However, experiments explicitly investigating this hypothesis, by e.g. temporally shading a certain area of the leaf, must be performed in order to get more decisive clues.

Synchronization

Another hypothesis concerning the influence of light intensity involves its temporal structure. Under both rhythmic and arrhythmic conditions, extended areas of the leaf have been shown to be significantly synchronized. Intriguingly, the same patches of high synchronization between leaf points also are subject to a high degree of synchronization with light intensity. This gives rise to the suggestion that synchronization between leaf cells could be provided by a periodical signal from the environment, in this case most likely a circadian modulation of L.
Considering the spatio-temporal dynamics of Φ_{PSII} , this hypothesis could be answered by extension of the data analysis tools used in this work. A crucial observation in this context is the comparison of the synchronization index of certain reference pixels with all other pixels $\mathrm{S}(\Phi_{ij} : \Phi_{i'j'})$ with the mutual information of the phase of the Φ_{PSII} signal $\mathrm{I}(\varphi(\Phi_{ij}) : \varphi(\Phi_{i'j'})) = -\sum_{q,s} p(\varphi_{ij,q}, \varphi_{i'j',s}) \ln \frac{p(\varphi_{ij,q},\varphi_{i'j',s})}{p(\varphi_{ij,q})p(\varphi_{i'j',s})}$, as shown in Fig. 5.22.

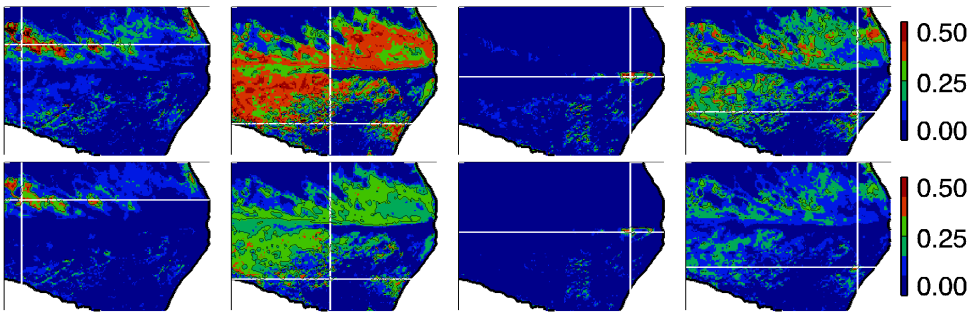

Figure 5.22: Comparison of the synchronization index (**top**) with the mutual phase information (**bottom**) for 4 arbitrarily selected points in the leaf. Data correspond to the timeseries shown in Fig. 5.3A

Comparing S with both mutual informations, one notices a striking similarity of the pattern of $\mathrm{S}(\Phi_{ij} : \Phi_{i'j'})$ and $\mathrm{I}(\varphi(\Phi_{ij}) : \varphi(\Phi_{i'j'}))$. Fig. 5.22 is representative for the entirety

of images in which S and I have been compared. This similarity seems to hold for any environmental condition. If thus, the synchronization index can be replaced by the mutual phase information, in the given model system this would signify that the relations between two pixels (i,j) and (i',j') plus a third quantity could be investigated by considering, e.g., the 3-point mutual phase information $\mathrm{I}(\varphi(\Phi_{ij}) : \varphi(\Phi_{i'j'}) : \varphi(\Delta w))$, and the 2-point conditional phase information $\mathrm{I}(\varphi(\Phi_{ij}) : \varphi(\Phi_{i'j'})|\varphi(\Delta w))$ (Yamada 1999; Matsuda 2000). From these informations, the network structure can be computed, i.e., it can be verified, whether two pixels are directly coupled or only indirectly via a third, environmental, agent mediating the coupling.
This speculation could also enter in the discussion of the results of the temperature-ramp experiments. The figures shown in Chapter 5.4 indeed exhibit heterogeneity, i.e. large areas of low Φ_{PSII} in determined phases of the rhythm. In comparison to the rhythmic regime however, the boundaries of these clusters are fixed, i.e. there is heterogeneity in the leaf, but without a dynamical expansion and shrinking of leaf patches. This is certainly not a proof that a circadian modulation of L is present in the series of Chapter 5.2 and 5.3 and absent in the case of Chapter 5.4, but it creates a new hypothesis for why the effects observed in Rascher et al. (1998) could not be reproduced in the experiments featured later (Rascher 2001). Any changes made in between both experiments, and which could have influenced the temporal structure of one of the control parameters of the experiments, should be carefully checked. An explicit experimental verification of the impact of a heterogeneous driving of the population of cells on the spatio-temporal dynamics in the leaf could give more decisive clues. Checking this hypothesis by simulation is the subject of the next chapter.

6 Simulations of Spatio-Temporal Dynamics

This chapter picks up the hypothesis that the spatio-temporal dynamics observed in the Φ_{PSII} -data analyzed in the previous chapter is linked to spatial gradients in light intensity. The intention is to elucidate some hallmarks being characteristic for various scenarios, rather than dealing with it in an exhaustive manner.

6.1 Distribution of Light Intensity

There are several practical facts about the experimental set-up which render it more probable that light intensity is heterogeneously distributed over leaf surface than being equal in all points. First, *K. daigremontiana* has relatively large leaves, causing a certain degree of bending, when being fitted into the cuvette. In addition to that, the geometrical arrangement of the camera, the illumination device, and the flashlights needed for Φ_{PSII} -imaging, lead to a non-perpendicular incidence of light onto the leaf.
Given an angle of incidence θ_n for a given oscillator number n, the light intensity L_n for that oscillator reads

$$L_n = L_0 \cos(\theta_n) \tag{6.1}$$

Hence, a constant curvature of the leaf surface with respect to the direction of incidence would produce a cosine-gradient in light intensity. Assuming that the source of light is not constant in time, but modulated with some amplitude L_A and period τ_d, the spatio-temporal distribution of L is given by

$$\begin{aligned} L_{nk} &= (L_0 + L_A \sin(\frac{2\pi}{\tau_d} t_k)) \cos(\theta_n) && (6.2) \\ &= L_0 \cos(\theta) + L_A \cos(\theta_n) \sin(\frac{2\pi}{\tau_d} t_k). && (6.3) \end{aligned}$$

This means that a curvature of the leaf surface would imply two spatial gradients, in the mean value of L_n, as well as in the modulation amplitude L_A.
The most basic way to implement such a scenario into simulations is to assume linear gradients of L and L_A over a 1-dimensional chain of oscillators. The simplified consideration of just one dimension can be justified by the fact that it also represents 2-dimensional

radial distributions of L. Thus using the chain of 64 uncoupled oscillators as in Chapter 4, L_n is given by

$$L_{nk} = L_1 + \frac{\Delta L}{\Delta n} + (L_A + \frac{\Delta L_A}{\Delta n}) \sin(\frac{2\pi}{\tau_d} t_k) \tag{6.4}$$

and is illustrated in Fig. 6.1.

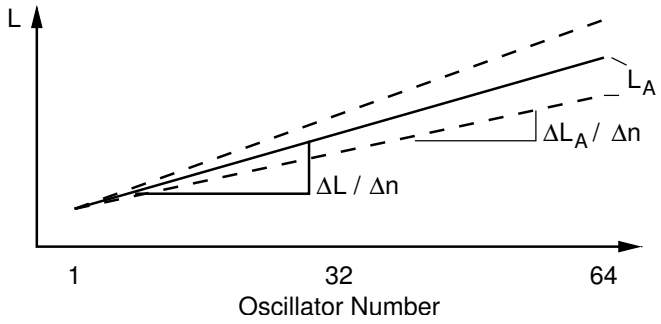

Figure 6.1: Spatial gradients of light intensity. The mean value L as well as the modulation amplitude L_A increase linearly starting with oscillator #1. The steepnesses of the gradients are given by $\frac{\Delta L}{\Delta n}$ and $\frac{\Delta L_A}{\Delta n}$, respectively.

6.2 1-D Chains of DLC oscillators

In this section the gradients in L shown in Fig. 6.1 are applied to a chain of 64 uncoupled DLC oscillators (Eqs. (4.28)-(4.34)), as this model has shown to be a better representation of the experimental observations in Chapter 5. Two scenarios are simulated, analyzed and compared: i) the case of a static gradient ($L_A = 0$), and ii) the case of a dynamical gradient resulting from a modulated source of light.

Static Heterogeneity

The implementation of a static gradient of L to a chain of DLC oscillators leads to a gradient in amplitude, mean value and frequency, with the lowest L being associated with high A, low $\bar{y}$ and the highest $|\omega|$. Hence all the properties characterizing the pacemaker regions observed in the leaf images, are found to be linked to low L in the simulations. Figure 6.2A shows the space-time-plot of the given scenario, the inclination of the lines of equal y indicating the spread of phase waves from the bottom to the top. The mentioned pacemaker qualities of the region of low oscillator numbers n are also manifest in the spatial distribution of $\bar{A}(y_n)$, $\bar{y}_n$ (D), and the dominant frequency ν_n^{dom} (Fig. 6.2C-E). The space-time plot of the phase (Fig. 6.2B) also exhibits the phase waves, which show up through the inclination of lines of equal phases. The most obvious demonstration of running phase waves is given by the phase difference with the meanfield $\overline{\Delta\varphi}(y : \hat{y})$ (Fig. 6.2F): clearly the pacemaker region is ahead of the average, and $\overline{\Delta\varphi}(y : \hat{y})$

decreases with n. The correlation function $C(y_n : \hat{y})$ (Fig. 6.2G) shows intermediate values throughout, and is the highest, where $\overline{\Delta\varphi}(y : \hat{y}) = 0$. An important observation is that the synchronization index $S(y_n : \hat{y})$ is maximal for n=1, and then drops monotonously. This is caused by the fact, that for $n \approx 1$, the oscillators have the highest amplitude and thus the biggest weight in the contribution to the meanfield rhythm $\hat{y}_n$. I.e. $\hat{y}_n$ is most strongly influenced by the oscillators with low n, hence it is clear that here also the highest values of $S(y_n : \hat{y})$ are obtained. The effects of heterogeneity without spatial order had already been discussed in Fig. 4.9. In fact, Fig. 6.2K-N and Fig. 4.9K-N show the same time course of $\hat{y}_k, A(\hat{y}), \hat{A}$, and D_k, as well as the same $P_{LS}(\hat{y})$ and $p(\nu_n^{dom})$.
In Figure 6.3 the phase relations of the y_{nk} are compared with the mean light intensity $\hat{L}$, which in this case is of course a constant in time. Thus, the average phase differences, cross-correlation, and synchronization are zero throughout the population. To make the plot comparable with the investigations with dynamical heterogeneity, the phase relations with $\hat{y}$, Fig. 6.2F-H, are overplotted with dotted lines.

Dynamical Heterogeneity

Adding a temporal modulation to the light gradient in the form of Eq. (6.4), changes the dynamics of the population of oscillators somewhat, as is depicted in Fig. 6.4. The general dynamics remain the same, as there exists a pacemaker region for low n, where the highest amplitudes, the lowest mean values and the earliest phases are observed. (Fig. 6.4A-G) The striking difference is given in Fig. 6.4H, which shows a displacement of the maximum of $S(y_n : \hat{y})$ away from the lowest n, as in the case of a static gradient, to an intermediate value of n.
Turning to the phase relations with $\hat{L}$ (Fig. 6.5), and in particular to subfigure C shows a plateau of significant synchronization with $\hat{L}$ for intermediate values of n. Variation of the modulation period τ_d can shift the location of the plateau, where higher τ_d evoke a shift towards higher n (data not shown). This is to be expected, as the native frequency of the oscillators decreases with n, due to the increasing light intensity. Another comprehensive observation is that the width of the plateau increases with higher modulation amplitudes. Even though these are only first steps towards an understanding of the impact of the spatio-temporal dynamics of the driver, the results are coherent and allow to create hypotheses about the pattern formation in leaves of *K. daigremontiana* , as is concluded next.

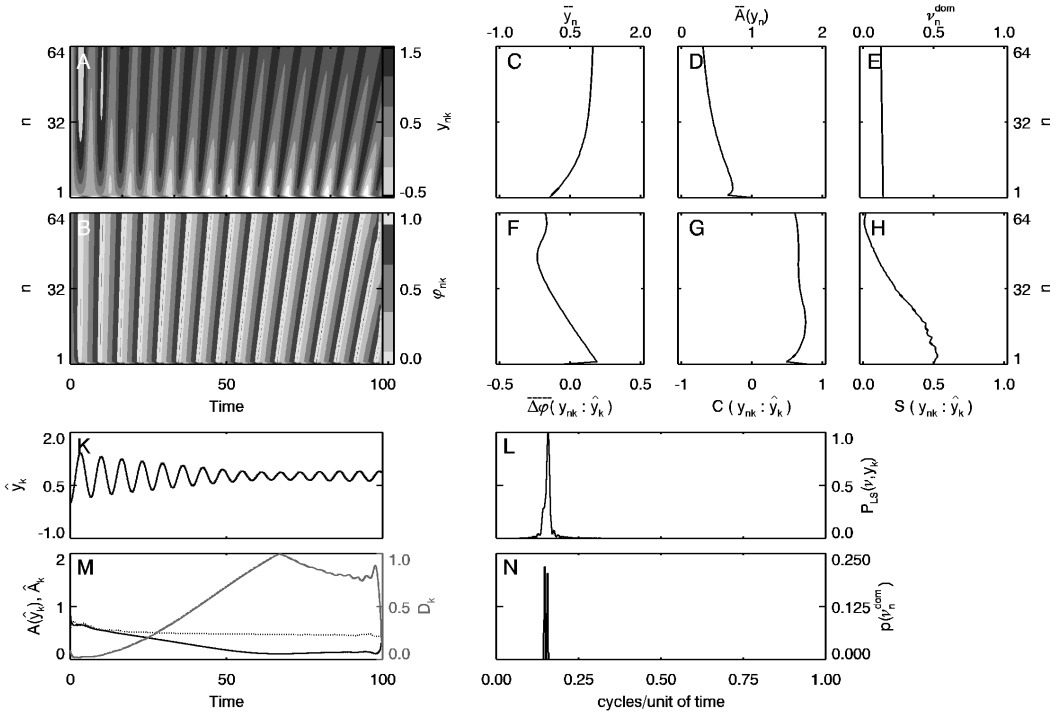

Figure 6.2: Population of N_n=64 DLC oscillators with a static gradient of L. L_1=0., $\frac{\Delta L}{\Delta n} = \frac{1}{64}$, $L_{A,1} = 0.$, $T = 0$. For explanation of the subfigures and all other parameters see Table 4.2. and Fig. 4.8.

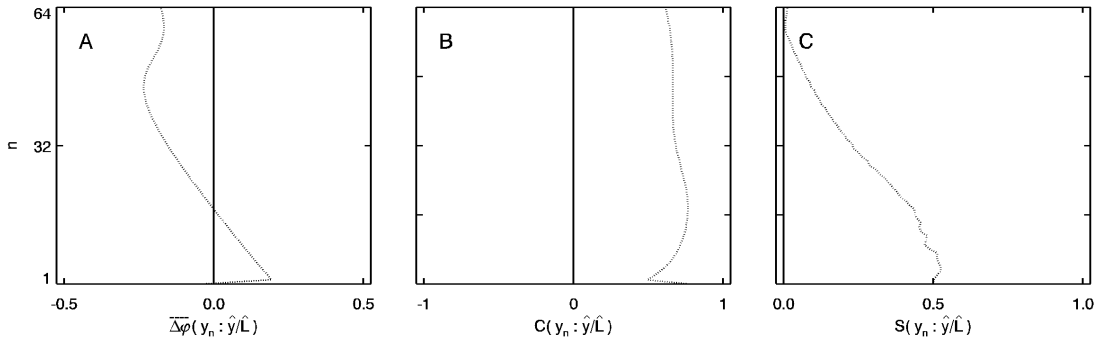

Figure 6.3: Phase relations of N=64 DLC oscillator under static heterogeneity with the meanfield signal $\hat{y}$ (dotted lines) and the mean light-intensity $\hat{L}$ (solid lines) as a function of oscillator number n (ordinate). **A:** Mean phase difference $\overline{\Delta\varphi}$. **B:** Correlation function C. **C:** Synchronization index S. The dotted lines are identical to the graphs in Figs. 6.2F-H.

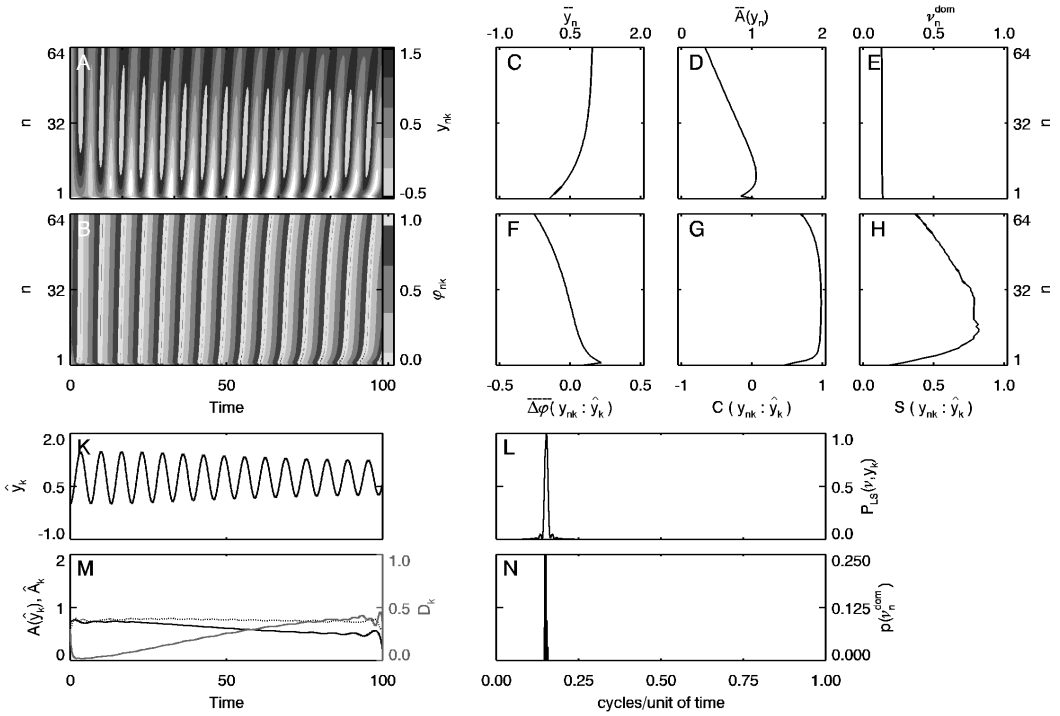

Figure 6.4: Population of N=64 DLC oscillators with a dynamical gradient of L. $\frac{\Delta L}{\Delta n} = \frac{1}{64}$, $L_{A,1} = 0.$, $\frac{\Delta L_A}{\Delta n} = 0.008$, $\tau_d = 6.7$, $T = 0$. For explanation of the subfigures and all other parameters see Table 4.2. and Fig. 4.8.

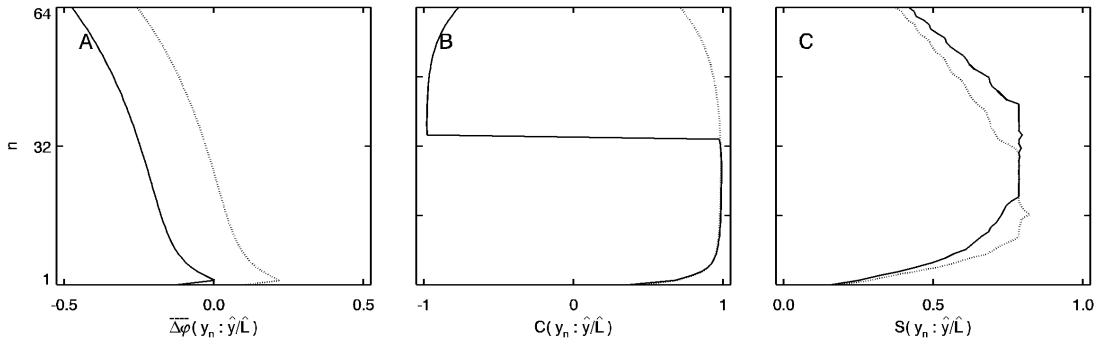

Figure 6.5: Phase relations of N=64 DLC oscillator under dynamical heterogeneity with the meanfield signal $\hat{y}$ (dotted lines) and the mean light-intensity $\hat{L}$ (solid lines) as a function of oscillator number n (ordinate). **A:** Mean phase difference $\overline{\Delta\varphi}$. **B:** Correlation function C. **C:** Synchronization index S. The dotted lines are identical to the graphs in Figs. 6.4F-H.

6.3 Conclusions

It is likely to happen that light is not incident on the leaf surface in a perpendicular and spatially homogeneous manner. In the case of a periodic variation in time of L this heterogeneity is not restricted to the mean value of L in a certain spot, but also extends to the modulation amplitude, which is higher in the places where the mean value is also high. The events in such a heterogeneously driven oscillatory medium can be illustrated by considering the resonance plots that had already been shown in Chapter 3.3. Figure 6.6A shows the situation encountered in the simulations shown in this chapter for low n and hence low L, given the modulation frequency ω_d is lower than the native frequency ω_0. The combination L_A and ω_d is outside of the phase-locking zone, hence the synchronization index is low under that circumstances. Going to higher n, i.e. increasing L, evokes two things: first L_A increases, i.e. moves up in the diagram, and L_0 and ω_0 decrease, such that the shaded phase-locking zone moves to the left in the diagram. Eventually this places the modulation in the phase locking zone, as is shown in Fig. 6.6B. This corresponds to the situation in the plateau of high $S(y_n : \hat{L})$. If n is further increased, the shifts of L_A continue, such that phase-locking is lost again, a situation which corresponds to Fig. 6.6C.

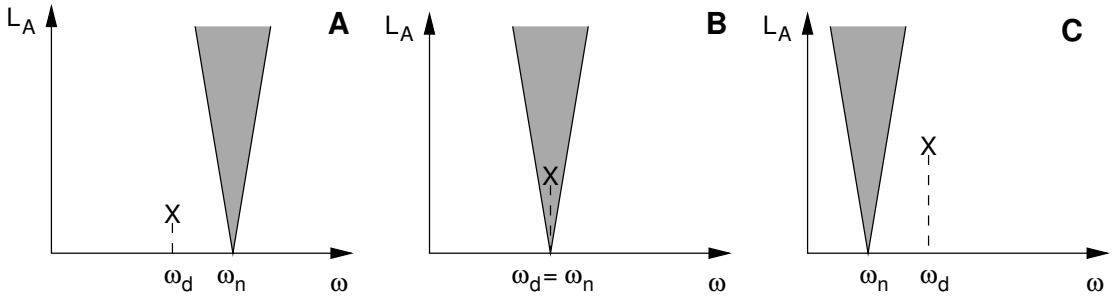

Figure 6.6: Resonance diagrams for different light intensities. Light modulation amplitude L_A is plotted over modulation frequency $\omega_d = 2\pi/\tau_d$. X marks the modulation properties for a given L_0. The shaded areas mark the regions where phase-/ and frequency locking occurs. **A:** At low L and for $\omega_d < \omega_n$ no phase-locking is given. **B:** Increase of L yields a reduction of ω_n and an increase of the modulation amplitude, such that phase-locking might take place. **C:** Further increases of L yield further displacement of L_A and the phase-locking zone, such that no phase-locking to the external driver takes place anymore.

If L_A is zero for all n it is obvious that no phase-locking can take place at all, and the synchronization index with $\hat{L}$ is zero everywhere. Remembering synchronization pattern seen in Chapter 5.2, the situation is nearly identical. The highest synchronization with both $\hat{\Phi}_{PSII}$ and L is neither observed in the pacemaker region (ref. discussion in Chapter 5.2.4), nor in the area which was claimed to be exposed to the highest light intensities, but just in the middle between these two areas. Comparing this result with the simulations performed here, strengthens the hypothesis that the phase waves observed in vivo are caused by the spatio-temporal structure of L. If there would have been a static gradient,

then there shouldn't be any synchronization with L and the regions of highest S with $\hat{\Phi}_{PSII}$ should be located in the pacemaker region. Again, this is not a proof of the hypothesis, but a sound prediction which should be verified in the experiment.
Finally it is interesting to notice that the assumptions about the parameter dependencies on L and T made in the given DLC model, are by no means specific for *Kalanchoë daigremontiana*, but may be valid for a huge class of circadian clocks. Hence this type of synchronization pattern should be observable in other tissues exhibiting cellular circadian activity.

7 Analysis of Multivariate Physiological Timeseries

The analysis of the ensemble of leaf cells (Chapter 5) demonstrated that the dynamics of a single image-pixel correlates with the dynamics of the collective rhythm. This correlation in turn allows to infer properties of the single leaf points from whole-leaf gas-exchange measurements. With this aim in mind, this chapter deals with the analysis of the multi-variate gas exchange measurements performed at entire, intact leaves, considering relations between net whole-leaf CO_2 uptake J_c , leaf conductance to water g_w , and the ratio of internal to external CO_2 concentration c_{ia} under both free-running conditions, as well as periodic variations of temperature and light intensity, as well temporary removal of CO_2 from the ambient air. The analysis is based both on techniques as presented in Chapter 4, as well as simulations of the CAM model by Blasius et al. (1999b).

7.1 Free-running Conditions

One of the main questions of the free-running rhythm of J_c is about the physiological site of rhythm control. Over the years, evidence has been presented which favors a dominant role of the stomata (Lüttge & Ball 1978; Wilkins 1991), while other findings reject this hypothesis and allocate rhythm generation to the mesophyll cells (Ritz & Kluge 1987). In C_3 plants, oscillations of c_{ia} and g_w (being proportional to stomatal conductance to water vapor g_w^s) were found to be coupled but governed by independent oscillators (Hennessey & Field 1991). Given the availability of g_w and c_{ia} data (for details of their measurement and estimation see Appendix D), the dynamics of both can be monitored. Their relation in the course of a free-running rhythm is checked for in this section.
In this context, another important variable being available is Δw , as it is an important signal for stomatal movements (see Chapter 2.1). This section deals with the phase relations among g_w , J_w and Δw and discusses the importance of a cyclic microenvironment as an additional feedback loop influencing the amplitude of the overt rhythm.

7.1.1 Rhythm Generation

Timeseries of J_c , g_w and c_{ia} of a free-running rhythm in constant conditions ($T_L = 21^oC$, $L = 140\ \mu E\ m^{-2}s^{-1}$) are shown in Fig. 7.1. These quantities are investigated

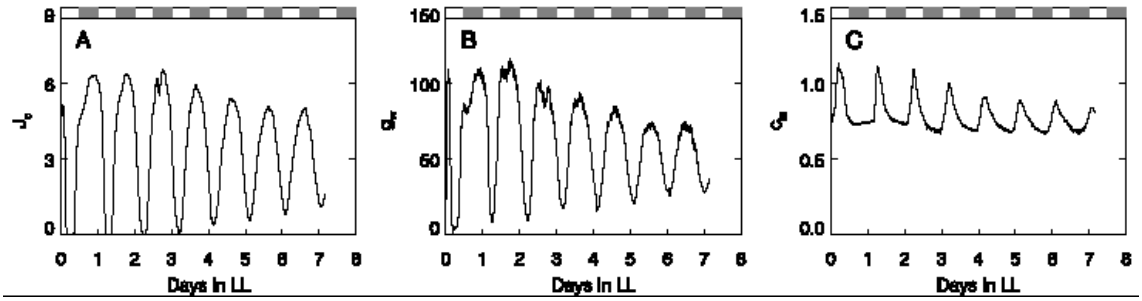

Figure 7.1: Timeseries of J_c (**A**), g_w (**B**) and c_{ia} (**C**) in free-running constant conditions ($T_L = 21^oC$, $L = 140\ \mu\text{E m}^{-2}\text{s}^{-1}$.

by a periodogram analysis with both the Lomb-Scargle method(P_{LS}), and estimation of $d\psi/dt = 2\pi/\tau$ by a linear fit, as well as the computation of their average phase-difference $\overline{\Delta\varphi}$ and the synchronization index S. The results are given in Table 7.1.

The periodogram analysis indicates that c_{ia} oscillates with a slightly larger period ($\tau = 21.9 - 22.0$h than g_w and J_c ($\tau = 21.8h$), as shown independently by both methods. This difference is still within the range of the error, and thus it can only serve as a hint for the control of c_{ia} and g_w by different oscillators. The fact that c_{ia} runs more slowly than g_w and J_c however is consistent with the results for $\overline{\Delta\varphi}$: as given in Table 7.1, $\overline{\Delta\varphi}$ (J_c :c_{ia}) is -0.43, that is $\varphi(J_c)$ is on average $0.07 \cdot 2\pi$ ahead of $\varphi(c_{ia})$, and $\varphi(g_w)$ is even $0.13 \cdot 2\pi$ ahead of c_{ia} , as follows from $\overline{\Delta\varphi}$ (g_w :c_{ia}). The similarity of dominant frequencies of J_c and g_w and also reflected in a high synchronization index, S(J_c :g_w) = 0.47. S(J_c :c_{ia}) = 0.31 and S(g_w :c_{ia}) = 0.27 are significantly lower, which could be due to the differences in intrinsic frequencies.
In total, these results indicate a desynchronized evolution of c_{ia} and g_w . J_c is influenced by both of them (see Chapter 2.1). The fact the the frequency and phase relations of J_c :g_w indicate a fairly synchronous dynamics with almost identical periods, is not a proof for the ultimate control of J_c by g_w . It is rather a hint, that J_c might be masked by

	J_c	g_w	c_{ia}
$\tau(P_{LS}^{max})$	21.8 ± 0.1	21.8 ± 0.1	22.0 ± 0.1
$\tau(d\psi/dt)$	21.79 ± 0.02	21.77 ± 0.02	21.91 ± 0.02
$\overline{\Delta\varphi}$ (x:g_w)	-0.06	-	-
S(x:g_w)	0.47	-	-
$\overline{\Delta\varphi}$ (x:c_{ia})	-0.43	-0.37	-
S(x:c_{ia})	0.31	0.27	-

Table 7.1: Rhythm parameters of J_c , g_w and c_i in Fig. 7.1. $\tau(P_{LS}^{max})$ is the period estimated from the maximum of the Lomb-Scargle-spectrum, and $\tau(d\psi/dt)$ the period estimated from the slope of a linear fit to the unwrapped phase $\psi(t)$. $\overline{\Delta\varphi}$ (x:g_w) and $\overline{\Delta\varphi}$ (x:c_{ia}) stand for the average phase difference between the quantity given in the top row (x stands for either J_c , g_w , or c_{ia}), and g_w and c_{ia} , respectively. S(x:g_w) and S(x:c_{ia}) depict the corresponding synchronization indices.

g_w (see Chapter 2.2). Two other timeseries in similar conditions have been investigated in the same manner (data not shown), supporting the suggested desynchronization of c_{ia} and g_w .

7.1.2 Cyclic Microenvironment

Figure 7.2 compares the timeseries of g_w , J_w and Δw and analyses their periods and phase relations according to the same procedure as in the preceding subsection. From visual inspection of Fig. 7.2, there are obvious correlations of Δw with g_w and J_w , and also the quantification of the $\Delta\varphi$ (Table 7.2) suggests a coherent behavior of all three variables.

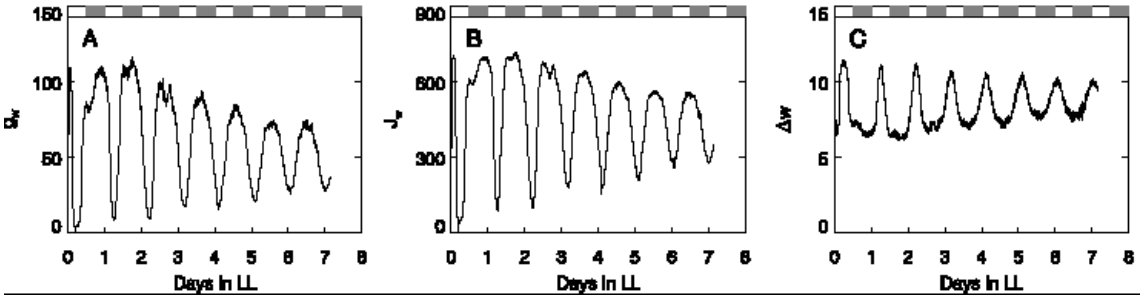

Figure 7.2: Timeseries of g_w (**A**), J_w (**B**) and Δw (**C**) in free-running constant conditions. Data are from the same experiment as in Fig. 7.1 ($T_L = 21^oC$, $L = 140$ μE m^{-2}s^{-1} .

	g_w	J_w	Δw
$\tau(P_{LS}^{max})$	21.8 ± 0.1	21.8 ± 0.1	21.8 ± 0.1
$\tau(\upsilon)$	21.77 ± 0.02	21.79 ± 0.02	21.78 ± 0.02
$\overline{\Delta\varphi}$ (x:J_w)	0.0	-	-
S(x:J_w)	0.61	-	-
$\overline{\Delta\varphi}$ (x:Δw)	-0.48	-0.48	-
S(x:Δw)	0.53	0.61	-

Table 7.2: Rhythm parameters of J_c , g_w and c_i in Fig. 7.1. $\tau(P_{LS}^{max})$ and $\tau(d\psi/dt)$ are estimations of the periods of g_w , J_w , and Δw as explained in Table 7.1. $\overline{\Delta\varphi}$ and S represent the average phase-differences and the synchronization index (see also 7.1).

In contrast to Table 7.1, all quantities have an identical intrinsic period of $\tau = 21.8$ h. Also the high synchronization indices of 0.53-0.61, and $\overline{\Delta\varphi}$ of 0.0, and -0.48 (as expected for quantities which are inversely proportional to each other, Eq. (D.3)), suggest that the circadian rhythm in g_w leads to a circadian variation of J_w , which finally causes a circadian variation of Δw . The latter oscillation is apparently due to the fact that the humidity added to the cuvette air by transpiration is not removed immediately, such that RH remains constant.

Leaf transpiration causes a *self-created, cyclic microenvironment*, a phenomenon which

is frequently observed for circadian cycles, in particular in suspensions of *Gonyaulax polyhedra* (Roenneberg & Hastings 1993; Roenneberg & Merrow 1999). As an increase in g_w leads to a decrease of Δw , which in turn is a signal causing a further increase of g_w (Fig. 2.2), there is a closed loop of *positive feedbacks* between the plant and its environment. Again, this mechanism does not generate a circadian rhythm, but it could amplify the magnitude of the overt rhythm in J_c , and furthermore sustain the oscillation, i.e. significantly reduce the damping rate.

7.1.3 Discussion

This section presented evidence but not yet proofs suggesting that the overt J_c rhythm is generated by two different autonomous oscillators situated in the stomata and in the mesophyll, respectively. It is hypothesized, that the circadian cycle of CO_2 demand is mainly caused within the mesophyll, however the observable rhythm in J_c is masked by g_w .
The masking by g_w and the environmental feedback can modify both the period *and* the amplitude of the rhythm in J_c : the period of the g_w oscillator might also dominate the spectrum of J_c , and the amplitude can be enhanced and sustained by the transpiration feedback loop between g_w and Δw .
These findings, suggesting a multi-oscillator hypothesis also in local rhythm generation of CAM, will be addressed again when interpreting further experiments of this section.

7.2 Periodic Temperature Pulses

Circadian rhythms are subject to entrainment by periodic temperature changes. In experiments performed by Lüttge et al. (1996), *Kalanchoë daigremontiana* showed entrainment to thermocycles with periods $12h < \tau_d < 28h$. This section shows the results of thermoperiodic perturbations with a fixed period of $\tau_d = 16$h, but varied duty-cycles, i.e. the fraction of one period spent at high temperature (Bohn et al. 2002), as well as experiments where the temporal protocol is fixed and only the amplitude of the thermodriver is varied.

7.2.1 Variation of Temporal Driver-Pattern

In the investigation of temporally stimulated systems, there is evidence that not only are the amplitude or the period of environmental stimuli of importance for the reaction of an observed system, but also the temporal pattern of the stimulus (Brezina et al. 1997). Accordingly, the circadian rhythm of *K. daigremontiana* has been driven with thermoperiodic pulses of fixed period $\tau_d = 16$ h and fixed amplitude $\Delta T = 7^oC$ between 21^oC and 28^oC, but different fractions of a period at high and low temperature, respectively.

The temporal patterns applied were warm:cold (WC) 12:4, 11:5, 8:8, 5:11 and 4:12 (Bohn et al. 2002). Two phenomena have been observed in these experiments:

- a continuous transition from free-running oscillations to full entrainment, and
- acute responses to the rate of temperature change, showing circadian gating.

Transition between Full and Partial Entrainment

Figure 7.3 shows the two extreme cases of WC4:12 (top row) and WC12:4 bottom row. In the case of WC(12:4), the spectrum (Fig. 7.3D) shows only significant peaks at $\tau_d = 16$ h, indicating full frequency locking, while for the spectrum of WC(4:12) (Fig. 7.3B) there are still contributions of the endogenous frequency. This phenomenon is also observed in simulations (Bohn et al. 2002). Figure 7.4 shows two simulations of the CAM model

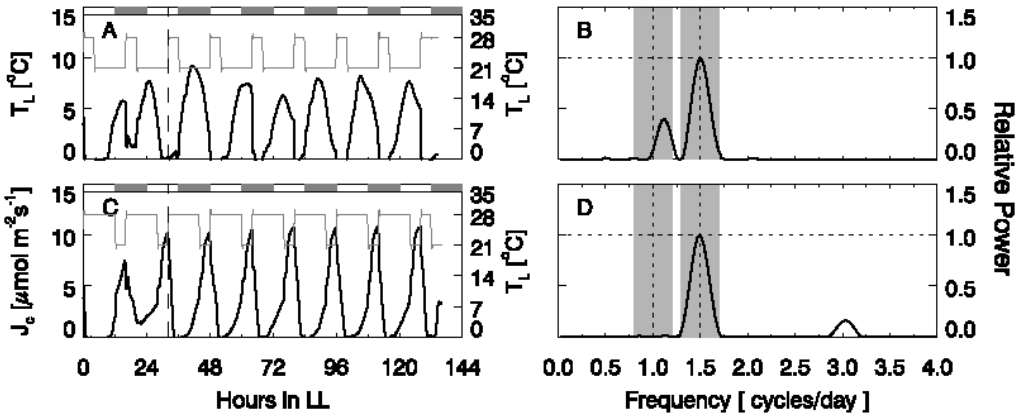

Figure 7.3: Experimental timeseries and frequency spectra for different thermo-driver patterns. **A:** Dynamics of J_c (black line) under a periodic variation of T_L (grey line) with 4 h at 28°C and 12 h at 21°C, WC(4:12). $L = 140$ μE m^{-2}s^{-1} = const. **B:** The Lomb-Scargle spectrum of J_c in A. The grey shading marks the circadian band of 0.8-1.2 cycles/day, and the driver band between 1.3-1.7 cycles/day. **C:** Dynamics J_c (black line) under a periodic variation of T_L (grey line) with 12 h at 28°C and 4 h at 21°C, WC(12:4). $L = 140$ μE m^{-2}s^{-1} = const. **D:** The Lomb-Scargle spectrum of J_c in C.

driven with thermoperiodic stimuli between T=245 a.u. and T=255 a.u. At the baseline-temperature, the oscillation has a τ of 2.42. In Fig. 7.4 the driver period τ_d was chosen to be τ_d=2.0 a.u., and duty cycles for high temperature of 0.3 (top row) and 0.8 (bottom row), respectively, have been considered. Qualitatively, the model shows the same results as the experiments, i.e. significant contribution of the endogenous τ_d in the spectrum of a duty-cycle smaller than 0.5 (Fig. 7.4B), with this contribution vanishing for DCs larger than 0.5 (Fig. 7.4D). In terms of nonlinear dynamics this behavior is characterized as a continuous transition from a driven fixed-point to a driven limit-cycle and vice-versa (Kaiser 2000): for long duty-cycles, the system spends the biggest part of each period in

the steady-state regime, resulting in the driver frequency being the only frequency visible. For short duty-cycles, the system spends more time per τ_d in the limit-cycle regime than at steady-state, so both the intrinsic and the driver frequencies become prominent.

Gated Responses to Temperature Changes

Characteristic kinks in the CO_2 curve being observed when temperature changes are given (see Fig. 7.3), result from an acute reaction of the plant to the rate of temperature change existing on top of responses to the absolute level of T_L . This is visualized by plotting the timeseries of the time derivative of T_L (Fig. 7.5).
In the top row, the temperature changes appear as up-and-down spikes, which give rise to spikes in the time-derivatives of J_c , g_w , and c_{ia} . An crucial observation is that the elicitation of the plant's response is again different for the diverse variables, and apparently depends on the circadian phase, in which the temperature change is invoked. E.g., in the case of WC(12:4) in all variables, a constant response pattern for all T_L -pulses is given, while for WC(4:12) the response strength varies strongly with time. In the dJ/dt-curve (Fig. 7.5A), there are several pulses (at about 12, 32 and 52 h in LL), which are not responded to by J_c , even though changes of g_w , and c_{ia} are observed. This is an indication that the reaction to the rate of temperature change is subject to circadian gating, i.e. is inhibited when the stimulus is given at a circadian time when the gates are closed.

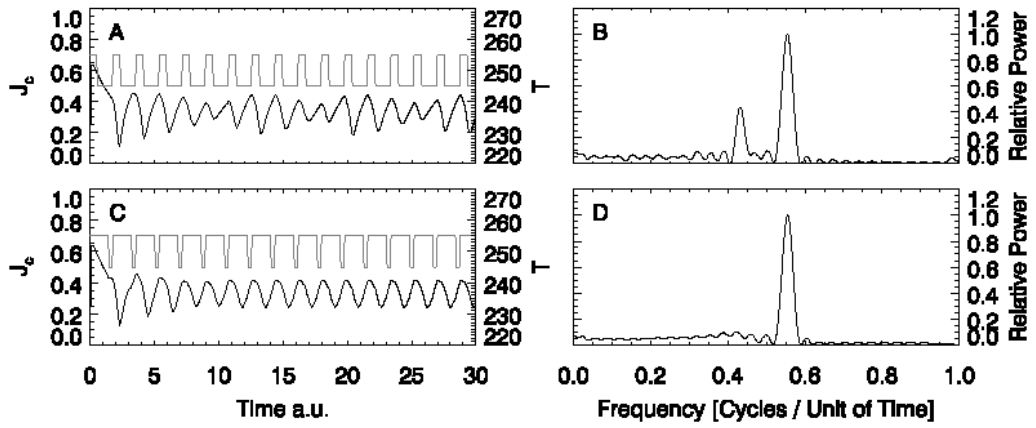

Figure 7.4: Simulations of the CAM model and frequency spectra for different thermo-driver patterns. **A:** Dynamics of J_c (black line) under a periodic variation of T (grey line) with 0.4 time units at $T = 255$ and 1.4 units at $T = 245$. **B:** The Lomb-Scargle spectrum of J_c in A. The intrinsic frequency of the CAM model at $T = 245$ is $\nu = 1/2.42 \approx 0.41$. **C:** Dynamics J_c (black line) under a periodic variation of T (grey line) with 1.4 time units at $T = 255$ and 0.4 time units at $T = 245$. **D:** The Lomb-Scargle spectrum of J_c in C.

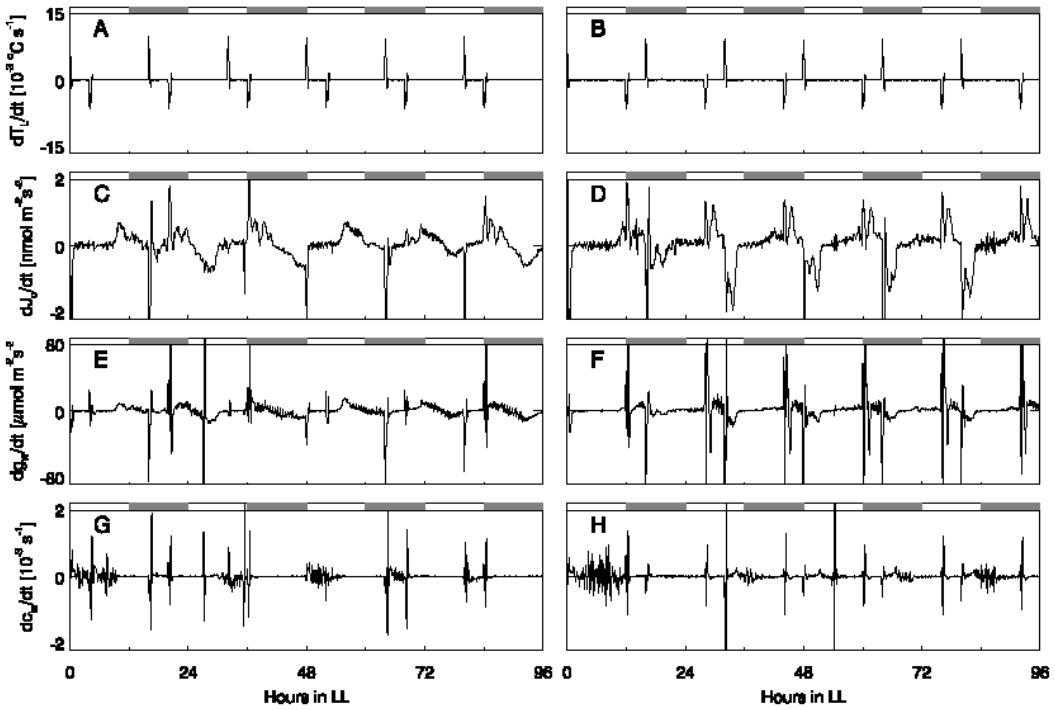

Figure 7.5: Time derivatives of T_L (**A,B**), J_c (**C,D**), g_w (**E,F**), and c_{ia} (**G,H**) for WC(4:12) (**left column**) and WC(12:4), **right column**. The series are derived from the same data set discussed in Fig. 7.3.

7.2.2 Varied Driver Amplitude

In order to probe the sensitivity of the rhythms to temperature changes, and to isolate putatively different oscillators, another set of experiments was performed by Sven Hinderlich at the Institute of Botany, Darmstadt University of Technology, maintaining the WC(4:12) pattern, but now varying ΔT_L as well as the baseline T_L (Bohn et al. 2003), (Fig. 7.6A,B). The chosen tool for data analysis is the Lomb-Scargle periodogram (Fig. 7.6B,D).

The essential information extracted from the spectra obtained from the timeseries during 6 thermocycles, are the maximum powers in the band of circadian frequencies and in the band of the thermodriver. Temperature changes of 1^oC and 3^oC have been applied, using baseline T_L of 21^o, 28^o and 31^oC. An overview of the results for the entire set of variables J_c , g_w , and c_{ia} under the various perturbation scenarios is given in Fig. 7.7, where the maximum powers of the circadian and the driver band are being compared.

At first sight, there again is a difference between the observations for g_w and for c_{ia} . As for c_{ia} τ_d is only dominant at very high ΔT_L (7^oC, Fig. 7.7C) or very high baseline temperatures (31^oC, Fig. 7.7T). For g_w , the driver is mostly dominant, except for the case of 22/21 (Fig. 7.7L), i.e. high amplitudes of endogenous oscillations of malic acid, and weak temperature perturbation. As in the case of the free-running model, the dy-

namical features of J_c correspond to the ones of g_w . In combination with the observation of the preceding section, this tightens the evidence that c_{ia} and g_w are interacting, yet are generated by different, independent, coupled oscillators.

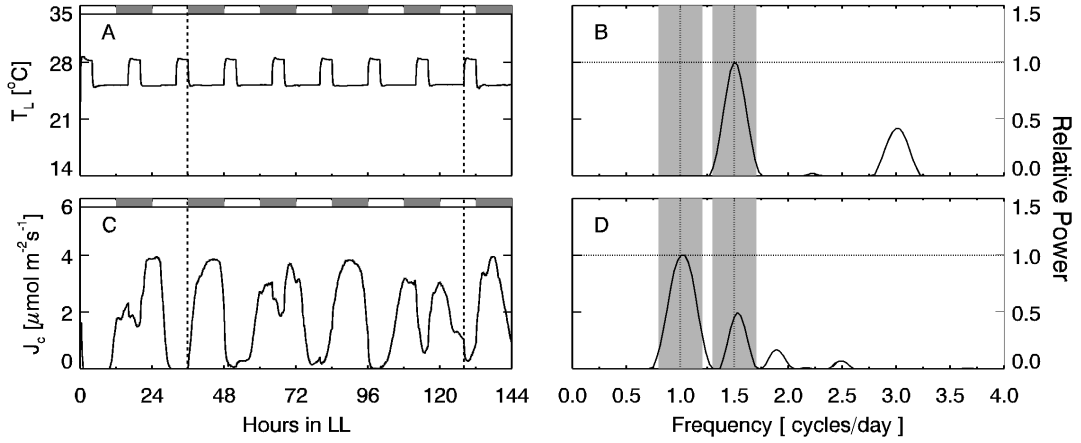

Figure 7.6: Timeseries and spectral analysis representative for experiments with varied driver amplitude. **A:** Temperature pattern with 4 h at 28^{o}C and 12 h at 25^{o}C. L=75 μE m^{-2}s^{-1} . The vertical dashed lines mark the section of the timeseries being subjected to spectral analysis. **B:** Normalized P_{LS} of the timeseries of Fig. A. The grey shading marks the circadian band of 0.8-1.2 cycles/day, and the driver band between 1.3-1.7 cycles/day. **C:** Net CO_2 -uptake under the thermoperturbation of A. **D:** Lomb-Scargle spectrum of C.

7.2.3 Effect of Temperature Changes

In order to elucidate possible signaling pathways, the effect of humidity dynamics upon temperature changes is considered more closely in the following. Figure 7.8 shows the relative humidity in an empty cuvette being subject to temperature changes. Increases of T_A from 21^{o}C to 28^{o}C invoke an immediate drop in RH_a of about 20%, which is recovered on a time scale of about 30 mins. Temperature drops elicit short transient oscillations, reflecting the feedback regulation of the cuvette, which in this case was programmed to maintain RH_a constant. Stomata are sensitive to changes in RH_a, and the observed physical/technical transduction of temperature changes might provide another temperature-sensing pathway, which contributes to masking of the overt rhythm of J_c . Figure 7.9 shows Δw with a leaf in the cuvette, and under temperature perturbations with ΔT = 3^{o}C. The spectrum of Δw for a basic T_L of 21^{o}C shows both significant contributions in the circadian, as well as the thermodriver range (Fig. 7.9B). For a base temperature of 25^{o}C, the dominance of the driver frequency is significantly increased (Fig. 7.9D). Assuming that the amplitude of the CO_2 oscillations in the mesophyll decreases, and Δw increases with T_L , a shift of dominance to the temperature pulses with increasing baseline temperature is to be expected. Hence, the relative humidity of the cuvette air results from a complex interplay of the thermo-induced, transient changes of Δw , and the leaf-induced microenvironment cycles.

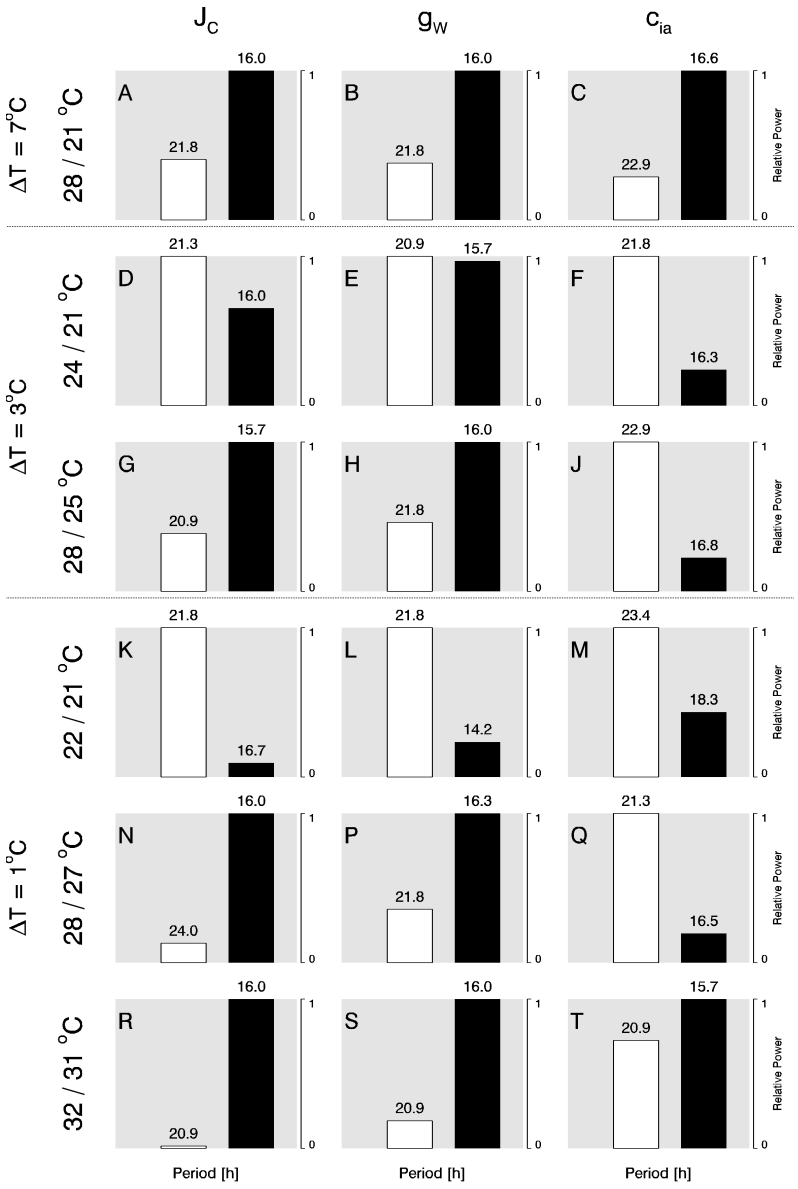

Figure 7.7: Spectral analysis of experiment with varied driver amplitude. White bars show the maximum power in the circadian frequency band, with the dominant period given on top of each bar. Black bars stand for the maximum power in the driver frequency band (cf. Fig. 7.6). In all cases the maximum power of the spectrum is in either one of the two featured bands. The entire spectrum is normalized such that the $P_{LS}^{max} = 1$. The **left column** shows the results for J_c under 6 thermocycles as shown in Fig. 7.6A. the **middle column** shows the results for g_w , the **right column** the results for c_{ia} . The top row (**A,B,C**) exhibits the results for a thermodriver pattern of 4 h at 28^{o}C and 12 h at 21^{o}C. Below, experiments with a ΔT of 3^{o}C are presented, i.e. 24/21^{o}C (**D,E,F**) and 28/25^{o}C (**G,H,J**). The bottom section shows experiments with $\Delta T = 1^o$ C.

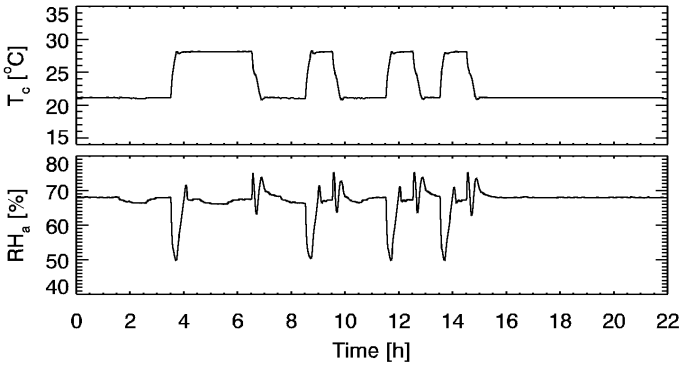

Figure 7.8: Timeseries of an empty cuvette with temperature changes. **Top:** Temperature shifts between 21°C and 28°C imposed within an interval of 22 h. **Bottom:** Time course of relative humidity in the cuvette (RH_a) under the temperature variation shown in the top image.

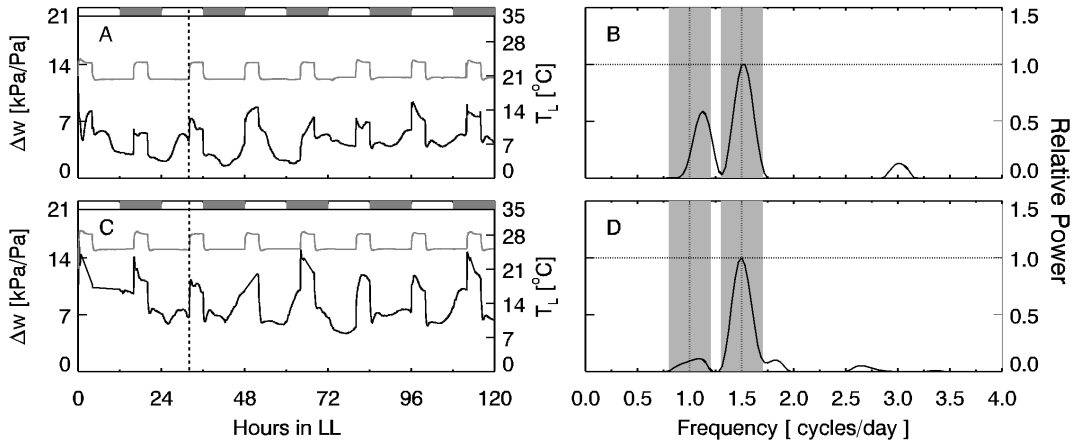

Figure 7.9: Timeseries and power spectra of Δw under stimulation with 4h warm:12 h cold thermocycles. **A:** Leaf temperature (T_L , grey line) with variations between 24 and 21°C. The black line represents Δw . The dashed line marks the start of the section being used for spectral analysis (section ends at 120 h in LL). **B:** Lomb-Scargle spectrum of Δw in A. Spectrum is normalized, so that $P_{LS}^{max} = 1$. The grey shading marks the circadian band of 0.8-1.2 cycles/day, and the driver band between 1.3-1.7 cycles/day. **C,D:** Analog to A,B with temperature perturbations between 25 and 28°C.

7.2.4 Discussion

The combined results of the investigation of thermal influences on the circadian rhythm of J_c strengthen the conjecture of independent circadian oscillations in both mesophyll and stomatal guard cells, as c_{ia} and g_w show a different response to temperature changes and elicit different entrainment behavior to temperature pulses of varied amplitude. The independent reactions of g_w to temperature changes are again a source of masking of J_c . A strong argument for this conjecture is that it provides an explanation of the circadian

gating of responses to temperature changes (Fig. 7.5). As mentioned above, temperature steps at 4, 32 and 52 h in LL do not evoke responses in J_c (Fig. 7.5C). The decreases of T at 4 and 52 h in LL occur in moments of extremely high internal CO_2 concentrations. Hence, even though there are slight changes of g_w the (Fig. 7.5D) J_c is dominated by c_{ia} and thus does not change. The increase of T_L at 32 h also occurs in the regime of high c_{ia} , so the stomatal closure which is supposed to be invoked by increasing temperature does not take place, as g_w (and J_c) are already at a minimum due to high internal CO_2 pressures. The concluding discussion of this chapter will get back to the issue of the relation of stomatal and mesophyll processes.

7.3 Periodic Light-Intensity Pulses

In analogy to thermoperiodic stimulations, rhythmic light-intensity studies have been performed on the circadian rhythm of CAM by Anja Geist at the Institute of Botany, Darmstadt U of T (Bohn et al. 2001). While in that publication, knowledge discovery of experimental data was featured, the focus of this section is hypothesis checking by comparing the impact of changes in L as observed in the experimental data with numerical simulations.

7.3.1 Simulations

Figure 7.10 shows simulations of the CAM model under periodic variation of L. The left panels show simulated timeseries of J_c , g_w and c_c under perturbation with driver period τ_d=2.0, i.e. shorter than the intrinsic τ of 2.42. L is raised from 1 to 4, thus driving the CAM model periodically across a Hopf bifurcation (Blasius et al. 1998). The right panels show the same scenario for $\tau = 2.6$ i.e. a longer than intrinsic driver period. Both timeseries are qualitatively representative for the quality of the dynamics observed for τ_d either greater or smaller than τ. While for $\tau_d > \tau$ a clear 1:1 phase locking takes place, for $\tau_d < \tau$ more complex waveforms emerge. More than that, for the comparison with experimental results, it is worth noticing the direction of responses to changes in L. For both τ, c_c decreases with increasing L due to enhanced activity of C_3 photosynthesis. The drop in c_c induces an increase of g_w , and both the enhanced C_3 -activity and the c_c -mediated increase of g_w together create an increase of J_c . With these predictions in mind, results from experiments are analyzed in the following.

7.3.2 Experimental Data

In the experiments performed by Anja Geist and co-workers (Bohn et al. 2001), the free-running rhythm was exposed to two different driver periods $\tau_d = 24$ h (left panels) and 16 h (right panels). The baseline L was set to 140 μE $m^{-2}s^{-1}$, and an amplitude of ΔL=90

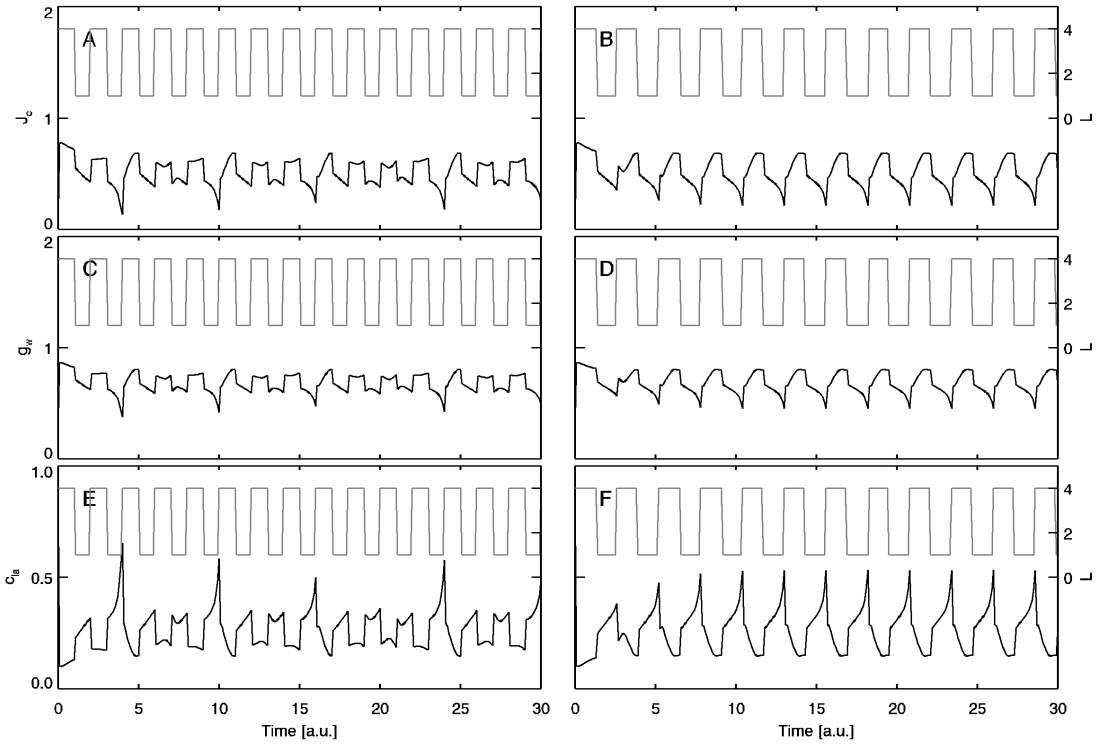

Figure 7.10: Simulation of the free-running rhythm of CAM driven by periodic variation of L between 1 and 4, $T = 245 = \text{const}$. **Left column:** Scenario for a driver period (τ_d) shorter than the intrinsic period τ of the model (τ_d=2.0, τ=2.42). **Right column:** $\tau_d = 2.8 > \tau = 2.42$. **A,B:** The simulated timeseries of J_c (black line) under variation of L (grey line). **C,D:** Simulated values of g_w and L. **E,F:** Timeseries of c_c and L.

μE m^{-2}s^{-1} was imposed on top. Figure 7.11 shows the results for J_c , g_w and c_i for both τ_d. The most visible fact already being discussed in Bohn et al. (2001) is that for τ_d =24 h there is entrainment in all variables. In turn, for τ_d =16 h, the amplitude of J_c loses its overt rhythmicity, while the both g_w and c_{ia} show regular responses and entrainment to the light-intensity steps. Comparison of these experimental with the numerical data yields a significant discrepancy between observation and prediction. As predicted by the model, changes in g_w have the same sign as changes in L. The astonishing fact however is that c_i also increases with L. This raises fundamental questions about the signaling pathways of L in CAM metabolism and stomata, which will be discussed in the following.

7.3.3 Discussion

Light intensity enters the current CAM model via C_3 photosynthesis. As an increase of L enhances Rubisco activity, internal CO_2 is fixed at higher rates, and thus its concentration drops. The experimental fact that CO_2 increases with light intensity raises questions about the source of the additional CO_2 . There are two hypotheses which could

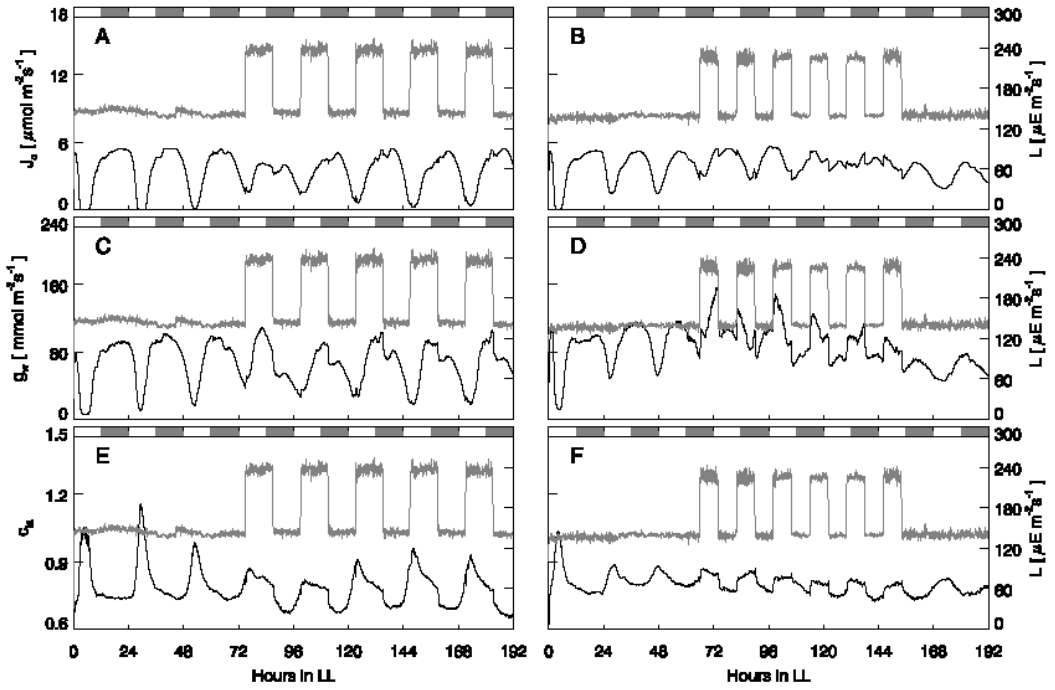

Figure 7.11: Experimental timeseries of the free-running rhythm of CAM driven by periodic light-intensities of 140 μE m^{-2}s^{-1} and 250 μE m^{-2}s^{-1} , T_L =21^{o}C. **Left column:** Driver period τ_d = 24 h. **Right column:** Driver period τ_d = 16 h. L is drawn with grey lines, the scale is to the right. The top row (**A,B**) shows the time-course of J_c , the middle row (**C,D**) data for g_w , and the bottom row (**E,F**) exposes data of c_{ia} .

be thought of.

The first hypothesis addresses the well known fact in chronobiology that the direction of response of circadian rhythms is the same for both temperature and light changes. As elevated temperature increases c_c and hence c_{ia} by enhanced efflux of malic acid, higher light intensities could evoke the same. As a matter of fact, Wilkins (1983) showed that light pulses in continuous darkness provoke malic acid efflux, leading to the hypothesis that the malic acid gates at the tonoplast are opened both by temperature and light. A direct light dependence of malic acid balance is included in the CAM model by Nungesser et al. (1984) and should be reconsidered in future modeling approaches.

The second hypothesis again deals with stomatal conductance. The observation that leaf conductance to water vapor increases with L cannot be explained unless taking into account a direct light sensitivity of stomata to changes in light intensity, which under certain circumstances can override the (also light dependent) internal CO_2 -signal (Mouravieff 1956; Zeiger & Hepler 1977). It might be the elevated g_w which also contributed to the light-induced increase of c_{ia} .

In conclusion, the comparison of numerical simulations and experiments of the light-driven CAM cycle suggest that to understand the CAM-CR in an environment of fluctuating light

intensity, more signaling pathways for light sensing must be taken into account in addition to the already implemented control of C_3 carbon fixation. First, here is reason to assume a direct impact of L on the C_4 part of carbon metabolism and second, stomatal control by c_i is very likely to be overridden by their own sensitivity to changes in light intensity. Thus the masking of J_c by stomatal dynamics is potentially also to be expected for fluctuating light intensity. In the picture of J_c being controlled by two independent oscillators, its breakdown for light stimulations with $\tau_d = 16$ h might be explained by the assumption that the usual phase relation between both oscillators, producing stable oscillations of J_c is destroyed, because of incompatible phase-shifts being evoked in both.

7.4 CO_2 Removal

The last approach of cycle manipulation featured in this chapter addresses the transient deprivation of the metabolic cycle from its substrate by removing CO_2 from the ambient air for a defined interval of time. In particular, the phase dynamics after CO_2 -removal is being investigated for both numerical simulations of the CAM model and experimental data. Departing from the current hypothesis of rhythm generation, the expectation is that a lack of CO_2 leads to a stop of the oscillator because the substrate for filling the vacuole with malate is not present anymore. Thus a phase-shift with respect to an unperturbed control system is expected.

7.4.1 Simulations

The removal of CO_2 from ambient air can be simulated by setting $c_a = 0$, which moves the CAM model over an inverse Hopf-bifurcation to settle in a steady state (Blasius et al. 1998). The crucial observable for a falsification of that model is the phase-shift induced by such a treatment in comparison to an unperturbed cycle. Under the condition that the duration of CO_2 -removal is long enough to allow the system to reach the fixed-point, the induced phase-shift can be predicted from pure arguments of phase-space topology. As the perturbed system is clamped in a fixed-point, which lies on one sole isochrone of the limit cycle, the phase shift depends solely on the phase of the cycle in which the unperturbed system is found just in that moment when the CO_2 -removal is relieved and the perturbed system is again subject to limit-cycle oscillations. Thus all phase shifts from -0.5 to 0.5 can be obtained in function of the time when CO_2 -removal ends. Figure 7.12 shows a number of simulations with different ending times of CO_2 removal to underline the topological statement.

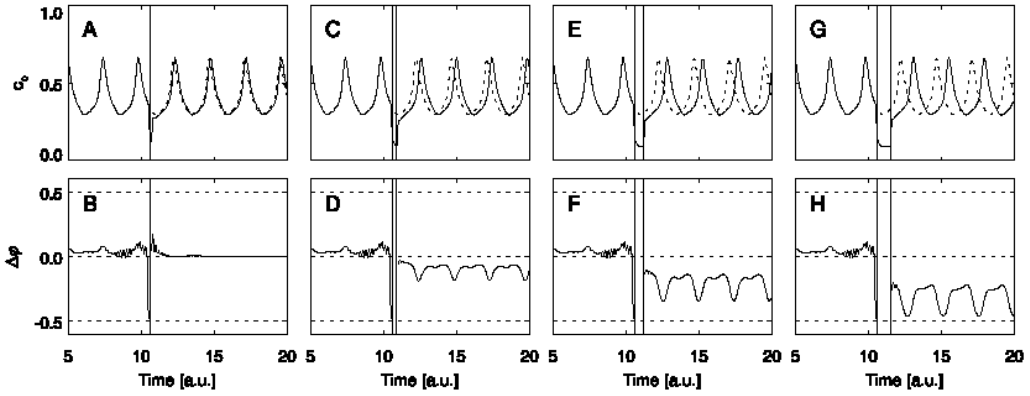

Figure 7.12: Simulation of CO_2 -removal with the CAM model. c_a was set to 0 at time 10.5, and was reset to 1 after an interval of 0.2 (**A,B**), 0.4 (**C,D**), 0.8 (**E,F**) and 1.2 units of time (**G,H**). The **top row** features the internal CO_2 concentration of the model. The solid line depicts the perturbed system, the dotted line an unperturbed control system. Vertical bars mark the time-section of CO_2 removal. The **bottom row** shows the phase difference ($\overline{\Delta\varphi}$) between the perturbed and the control series. Timeseries were not bandpass filtered before the calculation of the phase.

7.4.2 Experimental Data

Experiments with removal of CO_2 from ambient have been performed by Dr. Tomasz Wyka at the Institute of Botany, Darmstadt University of Technology. Several timeseries have been recorded, starting CO_2 removal at around 75 h in LL, i.e. when CO_2 is in a minimum, and 6 h later when the increase of J_c is maximal. The removal times have been varied between 11 and 36 hours. Figure 7.13 (top) shows the timeseries for c_{ia} , as J_c again might be under control of more than one oscillator. The dotted line represents the timeseries of an unperturbed run. Visual inspection of Fig. 7.13 shows that there is no appreciable phase shift between the perturbed and the unperturbed rhythm, i.e. the peaks of the dotted and the solid lines coincide also after the interval of CO_2 removal for all temporal patterns of CO_2 -removal. This is quantitatively confirmed by the timeseries of phase-shifts between both rhythms (Fig. 7.13,bottom): in no case a phase-difference settles on a value very different from 0. In fact the curves seem to head for the 0 difference line and stay there, which is most obvious in Fig. 7.13B. A stopping of the central oscillator by CO_2 removal, as predicted by the model cannot be inferred from the experiments.

7.4.3 Discussion

Again conclusions about the nature of rhythm generation have been drawn from a comparison of model predictions with experimental results. Here evidence is presented that the circadian rhythm of CAM is generated by a device which is capable of generating

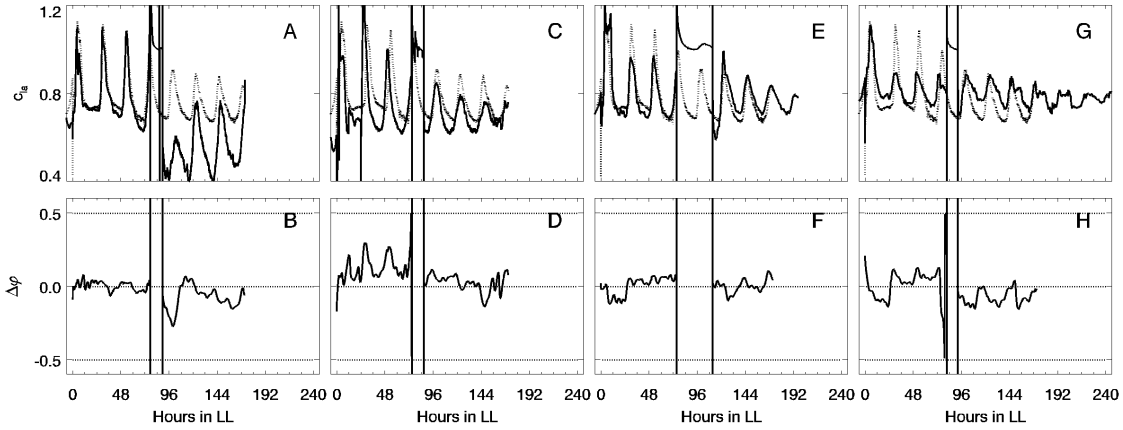

Figure 7.13: Experimental timeseries of internal CO_2 under temporary removal of ambient CO_2 .L= , $T_L = 21^oC$ = const. **Top row:** Timeseries of c_{ia} of a perturbed leaf (solid lines) and an unperturbed leaf (dotted line). The time section of CO_2 -removal is marked by the vertical bars. **Bottom row:** Phase difference ($\overline{\Delta\varphi}$) between the perturbed and the unperturbed timeseries. Phases were calculated after application of a low-pass filter with a cutting $\nu = 1/4$h. CO_2 has been removed between 75-87 h in LL (**A,B**), 77-89 h in LL (**C,D**), 75-111 h in LL (**E,F**), and 84-96 h in LL (**G,H**).

temporal information in a robust manner, being protected from severe metabolic perturbations. This accords with the statements on the robustness of circadian clocks given in Chapter 2 of this work, and rules out the currently featured periodic malic acid accumulation as a central pacemaking process. This is in accordance with observations that the damping of the malic acid amplitude is much stronger than the damping of J_c (Wyka & Lüttge 2003). As robust circadian pacemaking is probably not based solely on metabolic processes, gene transcription cycles might be another candidate. At least the interaction between metabolism and the level of gene expression should be considered in future models, as has also been suggested elsewhere (Roenneberg & Merrow 1999; Nimmo 2000).

7.5 Conclusions

The tools which have been used to assess the relations among the population of rhythms in the leaf tissue (Chapters 4-6) have been applied to elucidate the relations between simultaneously measured quantities of the entire leaf. The results of this chapter suggest not only the existence of the multi-oscillator complexity at leaf level which influences the global output, but also a multi-oscillator and multi-level nature of rhythm generation in each local spot of the leaf. Figure 7.14 compares the regulations incorporated in the CAM model by Blasius et al. (1999b) (A) with the additional picture including the regulations proposed throughout this chapter (B).

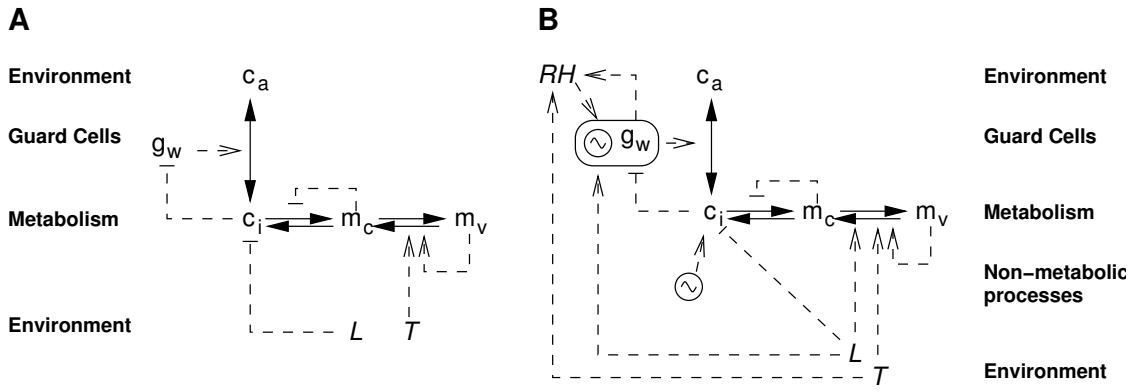

Figure 7.14: Carbon fluxes of CAM and their regulation. **A:** In the model by Blasius et al. (1999b) the dynamics is exclusively generated at the level of metabolism by the network of feedback loops which are under control of the parameters light intensity L, temperature T_L and external CO_2 (c_a). Stomatal conductance is solely determined by c_i . **B:** Contains the structure of Fig. A with the extensions suggested throughout this chapter. See text for explanations.

In total, the following conclusions are suggested from the results of this section (cf. Fig. 7.14):

- The circadian rhythm of J_c emerges from the action of two independent oscillators situated in the mesophyll, controlling c_i , as well as one in the stomatal guard cells, controlling leaf conductance to water g_w . This result is conveyed by an analysis of the dominant frequencies of all three quantities, as well as the phase relations among them (Section 7.1). Furthermore the responses to thermoperiodic perturbations also are explainable with this hypothesis (Section 7.4).

- The relative humidity in the cuvette plays an important role not in rhythm generation but in the masking of the overt rhythm of J_c . First, the circadian rhythm of stomatal conductance g_w and leaf-transpiration causes a self-created cyclic microenvironment, manifest in circadian oscillations of Δw and RH. This can have important effects on the magnitude and the upholding of the amplitude (Section 7.1). Also it is shown that changes of temperature can induce transient variation of RH, hence there is an indirect effect of temperature on g_w, which can significantly mask the rhythm of CO_2 uptake. Hence, future models of the circadian dynamics of J_c should not only take into account relative humidity as a control parameter, but as an additional level of dynamics which influences the gas exchange dynamics and is in turn influenced by the leaf dynamics itself.

- To understand the overt rhythm of J_c in a changing light environment, the fact that stomata may react directly to light changes, in addition to light-dependent CO_2 -signaling, must be taken into account in further models. Furthermore the hypothesis that light intensity has a direct impact on the compartmentation of malic acid must

be taken into consideration in order to obtain a more realistic picture of CAM under changing or fluctuating light intensity.

- Rhythm generation in the mesophyll is an multi-oscillator and/or multi-level process. The fact that CO_2 -removal from ambient air does affect the amplitude but hardly the phase of the circadian rhythm of c_{ia} , leads to the hypothesis, that the putative biological clock might be well protected against metabolic perturbations.

In conclusion, circadian rhythms in CAM not only involve complexity at the tissue level, but also at the local and cellular level. Viable approaches of how to meet the challenges of understanding the emerging multi-level/multi-oscillator networks will be discussed in the following closing chapter.

8 Discussion and Outlook

This thesis departed from the prediction that the circadian rhythm of CO_2 -uptake of entire leaves of the Crassulacean acid metabolism (CAM) plant *Kalanchoë daigremontiana* must be understood as the collective output of a population of oscillators. The aim of this work was the verification of this hypothesis with computational tools based on the theories of nonlinear dynamical systems and statistical physics. The results of this analysis give rise to concrete statements and new hypotheses concerning the chronobiology and plant physiology of circadian rhythms in *K. daigremontiana* . They can be subsumed in two classes of complexity: i) the physico-chemical type of complexity dealing with spatio-temporal dynamics in the population of (identical) leaf cells, and ii) the engineering type of complexity dealing with the multi-level structure of (diverse) functional units generating circadian rhythms in each local point of the leaf. Future work on *K. daigremontiana* with respect to both types of complexity might provide important contributions to understanding the behavior of complex organisms in a fluctuating environment. More than that, continuation of the so-far practiced interdisciplinary research might provide important practical experiences for the development of efficient interfaces of communication between experimentalists and theoreticians, which are likely to become future key factors for significant progress in life sciences.

8.1 Heterogeneity and External Influences: Complexity at Leaf Level

Model Descriptions

At the outset of this thesis, the theoretical description of CAM was based on a noise-driven excitable medium (Blasius 1997; Beck et al. 2001). In this description, the amplitude of the integrated, macroscopic output of the population is mainly a function of the phase dispersion of the oscillators. The amplitudes of the individual oscillations remain constant in all of the relevant scenarios. Alternative to this description of CAM dynamics, another prototype model for circadian rhythms has been investigated. Here environmental influences work directly on the amplitude, the damping constant and the native frequency of the oscillators. This allowed to study effects of heterogeneity on the aggregated dynamics, such that two scenarios of collective rhythmicity in CAM leaves were set against each other: *noisy and identical excitable systems* vs. *deterministic and heterogeneous oscilla-*

tory systems. Comparison of the amplitude and phase statistics of both scenarios with the in vivo amplitude and phase statistics of quantum efficiencies in the leaf showed no evidence for the hypothesized excitability, while the oscillatory model gives a good representation of the observed dynamics, and even further allows for testable predictions of the origins of the spatio-temporal dynamics and patchiness of the leaf. The main conclusion from this investigation is that the properties of the macroscopic rhythm, like, e.g., rhythm damping, are due to microscopic causes and not as predicted by Blasius (1997); Beck et al. (2001) emergent phenomena, which can only be observed at the global level.
From the methodological point of view, the concept of minimal modeling has proven its strength. Focusing on the dynamics only, i.e. abandoning physiological details, allows a tremendous information compression and enhances the numerical and computational feasibility of dynamical scenarios. Here, the model of Peterson & Jones (1979); Peterson (1980) has been used as basis for a phenomenological description of CAM oscillations, and with a few adjustments (not only valid for *K. daigremontiana* !) proved to be a representative description of the dynamics observed in the experiments.
Future work on the spatio-temporal dynamics in CAM leaves might continue from this point on. Dependencies of the oscillator properties on light and temperature different from the exponential shown here could be varied, e.g. a more threshold-like dependency might be checked for. For the consideration of effects of relaxation oscillations, dynamics of populations of displaced limit-cycle oscillators might be compared with other phenomenological models of circadian rhythms, e.g. Kronauers model (Kronauer 1990; Achermann & Kunz 1999), or a version of it adapted to CAM. Elsewhere, rhythm damping has been accounted for by circadian pacemakers consisting of two identical, coupled oscillators. In these systems, rhythm damping is caused by a loss of internal coupling (Daan & Berde 1978; Kawato & Suzuki 1980; Wu et al. 2000). An investigation of arrays of such two-oscillator pacemakers could also be a worthwhile step in investigating the spatio-temporal patterns in metabolic activity of CAM leaves.

Intercellular Communication

In this work and before, only populations without any interaction have been investigated with respect to the circadian rhythm of CAM. For *K. daigremontiana* this seems to be a justified assumption, as there are very high internal resistances to diffusion of e.g. CO_2 (Maxwell et al. 1997). As a matter of fact, phase-waves, which have been found to be the dominating spatio-temporal dynamics, are typical for spatially arranged, yet uncoupled systems. However other CAM plants like e.g. *Clusia minor* have larger intercellular air spaces and thus higher CO_2 conductances, thus here coupling might not be negligible. Hence, a better understanding of the possible coupling pathways in anatomically diverse CAM species, is a critical issue for a thorough understanding of structure formation in leaves of CAM plants.
A prospective experimental approach for testing questions concerning local coupling is

the sealing of the leaf surface with silicon grease. In the sealed area the uptake of ambient CO_2 is prevented, which has a strong impact on the metabolic activity in these areas, being reflected in the Φ_{PSII} signal, as silicon grease is transparent to chlorophyll fluorescence light. With this method, lateral diffusion of CO_2 from unsealed into the sealed areas could be detected. The question whether the observed phase waves are entirely due to spatial gradients in light intensity, or if cell-cell-coupling is involved has to be checked by applying broad stripes of silicon grease across the leaf surface, thus creating different "compartments". If such measures do not yield any changes in the spreading of the phase waves, an important contribution of cell-cell-coupling could be ruled out.
Apart from local coupling, the analyses of Chapters 5 and 7 also suggested the possibility of a global all-to-all coupling, mediated by the relative humidity in the cuvette. Patches in the leaf showing high amplitudes of their oscillation of J_c are also likely to show large changes of leaf water vapor conductance J_w . As was depicted in Chapter 7.1, the circadian rhythm in transpiration rate creates a cyclic microenvironment. Assuming that the water vapor transpired from the leaf is quickly homogenized in space due to the turbulent air flow in the cuvette, long-range interactions - at least between the stomatal apertures - could be evoked.

Spatio-Temporal Dynamics of Environmental Quantities

An analysis involving higher mutual phase informations could also deliver more clues on the importance of the spatio-temporal dynamics of light intensity L. In Chapters 5 and 6, evidences were presented that solely a spatial gradient of L might not be sufficient to explain the observed dynamics and the patterns of significant synchronization between leaf points, as well as between leaf points and L. The data analyses of Chapter 5 as well as the simulations of Chapter 6 give evidence that L must also be a periodic function of time, with a significant periodicity in the circadian range. Apart from the application of higher mutual information, the elucidation of the importance of the spatio-temporal dynamics for the patterns of metabolic activity can be advanced on both the modeling and the experimental side.
The modeling approach featured in Chapter 6 of this work was just an initial step. Simulations of heterogeneously driven systems could be extended to different types of oscillators, e.g. also relaxation oscillators and excitable systems. To the author's knowledge heterogeneous populations have been examined in details, but not for heterogeneous external drivers. Another aspect of introducing environmental time-scales to a population of oscillators is temporally and/or spatially correlated noise, which has been shown to induce spatio-temporal patterns in excitable media (Busch & Kaiser 2000; Busch et al. 2001). Hence, in this field, a lot of ground-laying work in screening the possible dynamical scenarios is to be done.
From the experimental point of view, advances in understanding the impact of the temporal structure of environmental quantities could follow from an explicit control and

modulation of L. In this case, the diverse temperature protocols (arrhythmicity, rhythmicity, ramps) should be repeated, by exposing exactly the same leaf to a protocol of continuous, modulated light, followed by a day-night-section and then passing a second time to continuous light, this time without any modulation. An extension of this assay would be to not only consider a periodic, but later on also a stochastic driving, which could provide valuable information about the impact of noise on the spatio-temporal dynamics in extended systems in vivo. In order to make full use of the power of the now available analysis tools, time series should be recorded as long as possible, even when all conditions are merely held constant.
This issue could extend the importance of investigations of the spatio-temporal dynamics in CAM leaves far beyond plant physiology, as phase synchronization in ecological systems has been a hot topic in the literature of the last years (Cazelles & Boudjema 2001). In addition to the examples of phase synchronization of animal populations by climatic drivers (Grenfell et al. 1998; Post & Forchhammar 2002), phase synchronization has been detected in Hare-Lynx cycles in Canada and modeled by a 3-variable model (Blasius et al. 1999a; Blasius & Stone 2000). Like in *K. daigremontiana* , crucial questions revolve around the type and agent mediating the synchronization. The first mentioned cases suggest synchronization by a common driver, while in the models of (Blasius et al. 1999a; Blasius & Stone 2000), local dispersal of predators and prey is claimed to the decisive process. A remarkable parallel between these models and the dynamics in CAM is that in both cases phase and amplitude dynamics have very diverging properties.
As those systems work on time scales of years, and space scales of 1000 kms, experimental verification of hypotheses are rather difficult to be realized. Well-controlled experiments on pattern formation in leaves of CAM plants could further the knowledge about characteristics of locally or globally acting phase-synchronizing quantities on an experimentally easier accessible time- and space-scale.

8.2 Modular Biology of CAM: Complexity at Cellular Level

In spite of all the advantages of minimal modeling, the predictive power of phenomenological models is increased significantly if the dynamics can be grounded on molecular and physiological bases. As is illustrated in Fig. 8.1, the present work has focused on phenomenological models representing different classes of dynamics. From the comparison with experimental data, the displaced limit-cycle (DLC) scenario has been favored. The upcoming challenge in physiological modeling of CAM is to find a plausible model which gives rise to DLC dynamics, i.e. rhythm damping, and the separation of phase and amplitude generation.
The data analysis of Chapter 7 provided a number of clues about the origin of the cir-

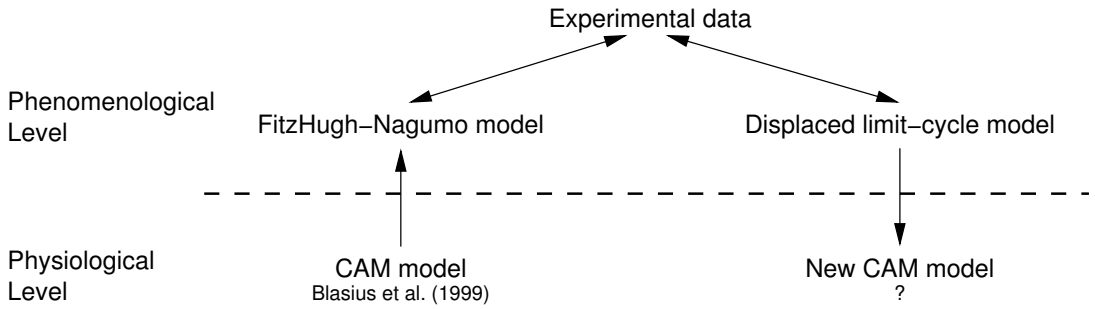

Figure 8.1: Modeling CAM at various levels of details.

cadian rhythm of net CO_2 -uptake. The main suggestion of these analyses is that future models must take into account the multi-level nature of rhythm generation, which proposes a modular modeling approach (Fig. 8.2). Such a proceeding would also bear in itself many practical aspects. For example, there is a number of established models on C_3 photosynthesis (Giersch 2000), as well as there are various existing models for stomatal conductance. Those already existing models could be used as description of the C_3 - and stomatal module. A new C_4 -module might be subject to a major revision in comparison to the models of Nungesser et al. (1984); Blasius et al. (1999b). Since the time these models were formulated, numerous aspects about the involved molecules have been discovered. For instance, a malate channel has been found which shows a strong dependence on temperature and pH (Hafke et al. 2003). Thus modeling of the malate-transport device consisting of several coupled membrane proteins which operate in function of substrate concentration, pH and temperature could be a prospective task. But also the kinetics of malic enzyme should be implemented in a more realistic fashion, as experimental evidences have been gathered on its strong regulation by light intensity and pH (Cook et al. 1995; Wedding 1989).

A general aspect which might be important is the fact that the fluxes and their regulation in the previous CAM models was limited to first-order terms only. Hence, flux saturations or cooperative regulations are not contained in the equations. Knowing that such nonlinearities play a fundamental role in the emergence of oscillatory dynamics, the linearizations inherent to the current model might have to be reconsidered.

As concluded in Chapter 7, the circadian clock in the mesophyll might be independent on metabolic processes. Comparing the situation with other organisms, a hot candidate for rhythm generation might be translational/transcriptional feedback loops. The advantage of a modular design is that the details of such a process need not be known, when one is interested in the impact on other modules. Hence a first approximation in the implementation of circadian gene expression could be to consider it to a black box, which acts as an external driver that periodically modulates fluxes in other modules, by varying rate constants, or the maximal value of certain flux. Subsequent steps could implement minimal models of rhythmic gene expression, such as the ones by Scheper et al. (1999)

or Lema et al. (2000). This would also allow to study a bidirectional coupling of, e.g. metabolism and gene expression.

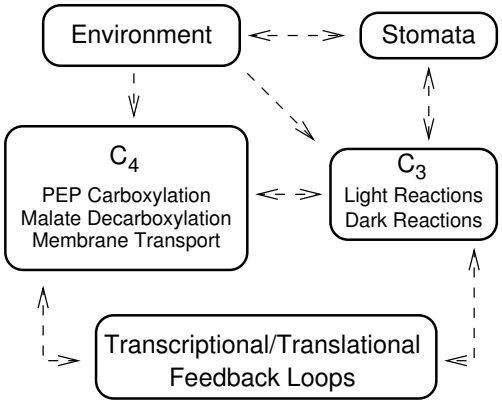

Figure 8.2: Modular structure of CAM.

8.3 Perspectives of Interdisciplinary CAM Research

Working with plant cells is far more difficult than dealing with animal cells, as plants cannot run away from a stressful environment, and hence possess very intricate regulatory systems allowing them to persist in a huge range of environmental conditions. Nevertheless, the results presented here demonstrate that advanced experimental methods, like the combined recording of ecophysiological gas fluxes and chlorophyll fluorescence imaging, together with data analysis methods and modeling approaches from the theory of nonlinear stochastic dynamics are an extremely powerful approach for deciphering the spatial and functional structure of circadian rhythm generation in intact leaves of *Kalanchoë daigremontiana* .

In modular biology, a big importance lies in the interfaces and the communication between the modules (Hartwell et al. 1999). Similarly, the success of interdisciplinary projects depends on whether an efficient protocol for the information flux between the scientists from the diverse disciplines can be established (Knight 2002). In the investigation of the circadian rhythms of CAM these interfaces have been established over many years now, with the present thesis being the latest contribution for the time being. A continuation and further development of this interdisciplinary work offers the chance not only to contribute to an understanding of plant biological clocks and rhythms, but also to develop a model system for advanced studies of the dynamics in extended oscillatory media in an continuously (and randomly) changing, heterogeneous environment.

A Abbreviations

$\Delta\varphi$	Phase difference	Eq. (3.19)
Δw	Vapor pressure deficit of ambient air	Ch. 2.1 and App. D
ν	Frequency of a timeseries	Ch. 3.1
ν_n^{dom}	Dominant frequency in the spectrum of oscillator n	Ch. 3.4
ω	Angular frequency	Ch. 3.1
Φ_{PSII}	Quantum efficiency of Photosystem II	Ch. 5.1
φ	Phase of a timeseries	Eq. (3.7)
ψ	Unwrapped phase of a timeseries	Ch. 3.1
A	Amplitude of a timeseries	Eq. (3.6)
$\hat{A}_k$	Timeseries of the mean amplitude, averaged over the population	Eq. (3.12)
$A(\hat{x}_k)$	Amplitude of the mean value of the population of oscillators	Eq. (3.12)
ADP/ATP	Adenosine di-/triphosphate, Redox couple, Energy storage compound	Ch. 2.1
C	Cross-correlation function	Eqs. (3.18)
c_a	CO_2 concentration in ambient air	Ch. 2.1 and App. D
c_c	CO_2 concentration at carboxylation sites	Ch. 2.1 and App. D
c_i	CO_2 concentration in intercellular air-spaces	Ch. 2.1 and App. D
c_{ia}	Ratio of CO_2 concentration in intercellular air spaces and ambient air	Ch. 2.1 and App. D
CAM	Crassulacean Acid Metabolism	Ch. 2.1
CR	Circadian Rhythm	Ch. 2.2
DLC	Displaced limit-cycle oscillator	Ch. 4.2
FHN	FitzHugh-Nagumo oscillator	Ch. 4.1
g_c	Leaf conductance to CO_2 diffusion	Ch. 2.1
g_c^s	Stomatal conductance to CO_2 diffusion	Ch. 2.1 and App. D
g_c^i	Internal conductance to CO_2 diffusion	Ch. 2.1 and App. D
g_w	Leaf conductance to water vapor	Ch. 2.1 and App. D

IAS	Intercellular air-spaces	Ch. 2.1
J_c	Net CO_2 flux from ambient air into the leaf	Ch. 2.1 and App. D
J_w	Net water vapor flux from the leaf to the ambient air	Ch. 2.1 and App. D
L	Light intensity	App. D
ME	Malic Enzyme	Ch. 2.1
NADP/ NADPH	Nicotinamide adenine di-nucleotide, Redox couple, Energy storage compound	Ch. 2.1
$p(\nu^{dom})$	Probability of a given dominant frequency	Ch. 3.4
$P_{LS}(\omega, x_k)$	Lomb-Scargle periodogram of a timeseries x_k	Eqs. (3.3, 3.4)
PEPC	Phosphoenolpyruvate carboxylase	Ch. 2.1
R_d	Dark Respiration	Ch. 2.1
RH_a	Relative humidity of ambient air	Ch. 2.1 and App. D
Rubisco	Ribulose-bis-phosphate Carboxylase Oxigenase	Ch. 2.1
S	Synchronization index	Eq. (3.23)
T_a	Air Temperature	
T_L	Leaf Temperature	
$\hat{x}_k$	Timeseries of the population average of variable x	Eq. (3.11), Table 4.2
$\bar{x}_n$	Temporal average of variable x of oscillator n	Table 4.2

B Nonlinear Dynamics of Self-Sustained Oscillators

In nonlinear, thermodynamically open systems, self-sustained oscillations arise from the transformation of a non-oscillatory source of energy or matter into oscillatory motions or reactions (Goldbeter 1996; Pikovsky et al. 2001). Periodically recurring processes are just one possibility for the temporal evolution of a system, i.e. self-sustained oscillations are just one subset of the entire class of dynamical processes.

Dynamical Systems

Dynamics is the subject that deals with change, with systems that evolve in time (Strogatz 1994). A dynamical system with continuous evolution in time is mathematically represented by a set of variables $x_1, x_2, ..., x_n$, the evolution of which is described by a set of n ordinary differential equations (ODEs).

$$\begin{aligned} \frac{dx_1}{dt} &= f_1(x_1, x_2, ..., x_n; \alpha) \\ \frac{dx_2}{dt} &= f_2(x_1, x_2, ..., x_n; \alpha) \\ &\vdots \\ \frac{dx_n}{dt} &= f_n(x_1, x_2, ..., x_n; \alpha) \end{aligned}$$

where the α are the parameters of the system. Dynamical systems modeling is thus equivalent to choosing a set of appropriate variables and the formulation of the right-hand sides $f_n(x_1, x_2, ...x_n, \alpha)$. For example, with the law of mass action, the system of chemical reactions

$$\mathrm{A} \leftrightarrow \mathrm{X},\ \mathrm{B} \rightarrow \mathrm{Y},\ \ 2\mathrm{X} + \mathrm{Y} \rightarrow 3\mathrm{X}$$

can be cast in the system of ODEs with variables x and y describing the concentrations of X and Y

$$\frac{dx}{dt} = a - x + x^2 y \tag{B.1}$$

$$\frac{dy}{dt} = b - x^2 y \tag{B.2}$$

and the parameters a and b representing the constant concentrations of reactants A and B (Schnackenberg 1979; Murray 1993).

Systems Analysis

The aims of *systems analysis* are to elucidate the steady-state solutions of the system of ODEs and their local stability. A steady-state, also called equilibrium point, is a set of values of the variables, from which the system does not change as time proceeds, i.e. where $x(t) = x_0, y(t) = y_0$ are constant for all times. They are obtained by setting the left-hand sides of Eqns. (B.1) to 0, and solving the resulting equation system to get the x_n^*. In the case of Eqns. (B.1,B.2) the result yields

$$x^* = b + a,\ y^* = \frac{b}{(a+b)^2}. \tag{B.3}$$

The local stability of a steady-state is determined by perturbing the system with small stimuli. If the steady-state is reestablished, then it is called stable. Otherwise, if the system upon small perturbation leaves the steady state and exhibits another kind of dynamics, the steady state is called unstable. Applied in a systematic fashion, the stability properties of a system can be determined by the technique of linear stability analysis, see (Strogatz 1994; Nicolis 1995).
As parameters change, the local stability of the steady-state may change, thus one important result of systems analysis is to map the dynamical behavior of the system in dependence on the parameters. Any parameter value at which the number and/or stability of the steady states change is called a bifurcation point, and the system is said to undergo a bifurcation. The most important bifurcation for this work is the Hopf bifurcation, in which a self-sustained oscillation is born from stationary steady-state dynamics. For Eqns. (B.1,B.2), the bifurcation line in parameter space (a,b), which separates the steady-state regime from the oscillatory regime, is given by the solutions of the equation

$$b - a = (a+b)^3. \tag{B.4}$$

Figure B.1 shows the different regimes in parameter space and one timeseries for oscillatory and steady-state behavior, respectively. An important aspect is that only values $a > 0, b > 0$ are considered, because as a and b represent concentration of reactants, only positive values are physically sensible.

Phase Plane and Limit Cycles

A powerful tool to visualize the properties of a dynamical system is the phase space (Strogatz 1994). The axes of this space are spanned by the variables x_n, and the temporal evolution given by the ODEs (Eqns. (B.1)) is manifest in the set of trajectories of the system through the phase space. For the system of Eqns. (B.1, B.2), the phase space is shown in Fig. B.2. The left phase portrait (B.2A) shows the system in the steady-state regime, where all trajectories point towards the stable fixed point, the geometrical representation of a steady-state. In the oscillatory regime being shown in Fig. B.2B all trajectories end up in a closed loop, a so-called limit cycle. Fixed points and limit cycles are also called attractors of the system, as they "attract" all the trajectories in a certain

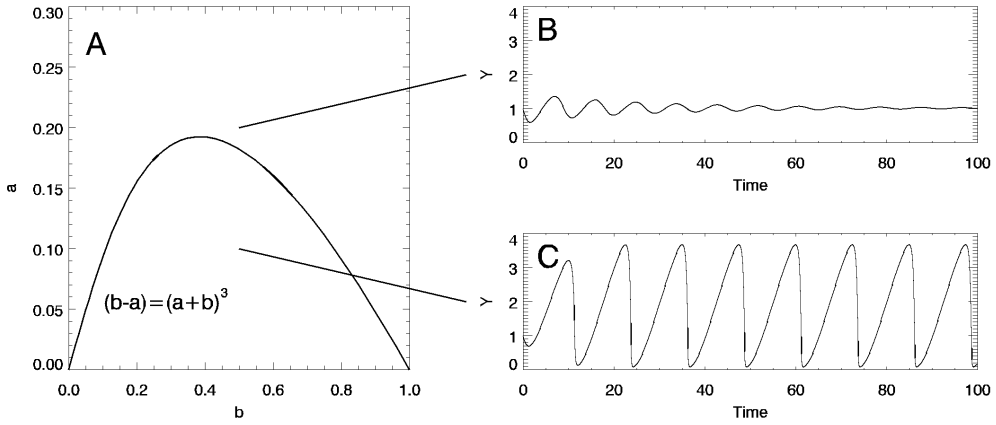

Figure B.1: **A:** Parameter space of Eqns. B.1,B.2, for $a > 0, b > 0$. The area below the curve depicts the regime of self-sustained oscillations. **B:** Simulated time-series of y for $a = 0.2, b = 0.5$, showing transient dynamics to a steady-state. **C:** Simulated time-series of y for $a = 0.1, b = 0.5$, showing self-sustained oscillations.

section of the phase-space, the *basin of attraction*.

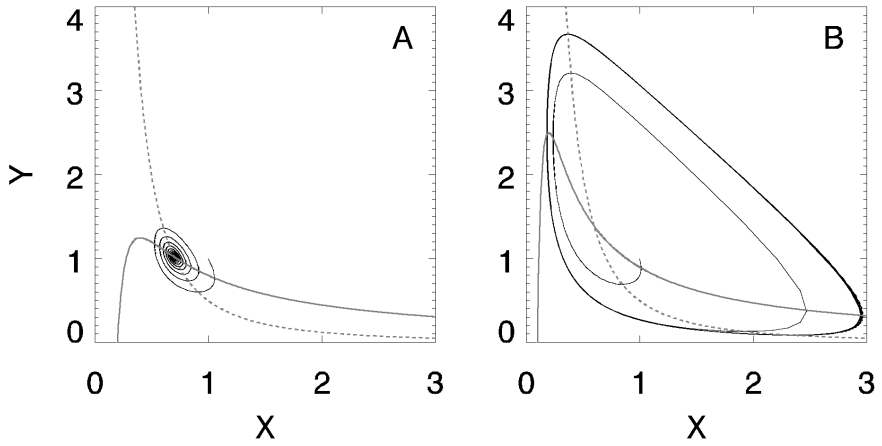

Figure B.2: **A:** Phase portrait of system Eqs. (B.1, B.2), showing evolution into a steady-state regime. $a = 0.1, b = 0.5$ (corresponds to Fig. B.1B). The grey solid line is the nullcline $dx/dt = 0$, the grey dashed line the nullcline $dy/dt = 0$. **B:** Phase portrait of system Eqs. (B.1, B.2) in the oscillatory regime, showing evolution into a limit cycle. $a = 0.2, b = 0.5$ (corresponds to Fig. B.1B). The nullclines are identical to the ones in A.

Dynamical systems can exhibit two more types of behavior, i.e. quasiperiodic and chaotic dynamics. The corresponding geometrical structures in phase space are tori and strange attractors, respectively. These types of dynamics are subject of a vast literature, e.g. (Strogatz 1994; Mackey & Glass 1988; Goldbeter 1996), and as they are not featured any further in this work, they are not discussed in detail.

Perturbed Oscillators

In phase space, the impact of an external perturbation on a self-sustained oscillator is depicted as a deviation of the trajectory off the limit-cycle (Fig. B.3A). As limit cycles describing biological clock must be stable, the system returns to the cycle, i.e. the amplitude returns to its initial value, yet a phase-shift in relation to the unperturbed system has been introduced: "the amplitude of a limit cycle is stable, but the phase is free" (Winfree 2001).
Scanning the entire cycle by applying a defined perturbation in each possible phase of the cycle, and measuring the induced phase shift as function of the old phase, one obtains a phase-response curve, an important tool for the investigation of biological clocks (Winfree 2001; Mackey & Glass 1988). Figure B.3B sketches a typical phase-response curve for a biological clock perturbed with light pulses. Pulses applied in the early subjective night provoke a phase-delay (as the system assumes a prolonged dusk) while light pulses in the late subjective night provide a phase-advance (as the system is expecting an early dawn).

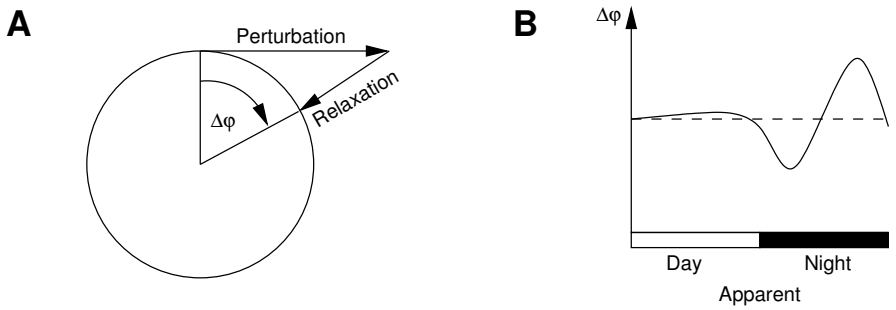

Figure B.3: Perturbation of self-sustained oscillators. **A:** Scheme of a perturbation of a system from a (circular) limit cycle. After perturbation the system returns immediately to the limit cycle, by which a phase shift $\Delta\varphi$ in comparison to an unperturbed system has been introduced. **B:** Sketch of a typical phase-response curve of a biological clock perturbed with light pulses, plotting the induced phase shift as a function of the phase when the perturbation occurred.

C Numerical Techniques

C.1 Data Analysis

The analysis of both experimental and numerical data have been performed with scripts written in IDL 5.3.

Lomb-Scargle Periodogram

The Lomb-Scargle periodogram has been calculated with the IDL function *lnp_test*, which is an implementation of the subroutine *faster*, found in the Numerical Recipes (Press et al. 1992).

Fourier Transform

The Fourier transform has been computed with the IDL function *FFT*, which uses a Winograd algorithm (Press et al. 1992). The advantage of this algorithm is particularly that the number of points in the analyzed timeseries does not have to be an integer power of 2 like in the algorithms provided with many other data analysis software kits.

Hilbert Transform

The Hilbert transform has been computed with the IDL function *hilbert*. This algorithm consists of three steps:

1. Computation of the Fourier transform of the given data vector x_k
2. Multiplication of the components of the Fourier spectrum having positive real parts with i
3. Re-transformation to the time domain by inverse FFT

Bandpass Filtering

Bandpass filtering has been realized by Fourier filtering. The ideal Fourier filter is a rectangular function which suppresses all frequencies outside the desired band by 80dB. Before applying the filter to the Fourier transform of the timeseries of interest, the ideal filter is convolved with a Hanning window by multiplying the inverse FFT of the ideal filter with a Hanning window and FFT transforming back to the frequency domain.

Non-Periodic Trend Analysis

Low frequency fluctuations have been eliminated by bandpass filtering. In order to detect a non-periodic, polynomial trend in the considered timeseries, the data vector x_k was fitted to a fourth-order polynomial with the IDL function *poly_fit*, which is based on a least-square fit. In order to detrend the timeseries, the best-fit curve has been subtracted from the original series.

C.2 Simulations

Integration of Stochastic Differential Equations

The simulations have been performed with the software package *xpp* version 5.5, and been confirmed with spot-checks with programs written in Fortran 90. As integration algorithm in both cases a second order Runge-Kutta method has been used. This low-order algorithm is sufficient, as for stochastic differential equations, the integration step size must be rather small, because noise (being updated at each integration step) needs to be the smallest time scale of the system (Garcia-Ojalvo & Sancho 1999).

Noise Generation

In the simulations white noise has been generated by adding a Wiener parameter to the differential equations (xpp-function *wiener*). These parameters are held constant during one integration step. The term dW is given for an integration step size dt by $dW = \sqrt{dt}N(0,1)$, where $N(0,1)$ is a normal distribution with zero mean and unit standard deviation, which is generated by standard random generators for uniformly distributed random numbers, e.g. *ran1* (Press et al. 1992), which is transformed to the normal distribution by the Box-Mueller algorithm.

D Relations of Plant Physiological Observables

This chapter surveys the quantities which are available from an intact single leaf in a cuvette and are subject to timeseries analysis. There are two classes, the quantities measured directly and those derived mathematically from the former. Details of the setup can be found in Rascher (2001).

D.1 Measured Quantities

Directly measured quantities are

- net whole-leaf CO_2 -uptake (J_c), given in μmol $m^{-2}s^{-1}$
- whole-leaf transpiration rate (J_w), given in mmol $m^{-2}s^{-1}$
- relative humidity of the cuvette air (RH_a), in %
- leaf as well as cuvette air temperature (T_L / T_A), in ^oC.
- Photosynthetic photon flux density (L), in μE $m^{-2}s^{-1}$
  ($=$ μEinstein $m^{-2}s^{-1}$ $=$ μmol Photons $m^{-2}s^{-1}$)

D.2 Derived Quantities

From the directly measured quantities, some other important variables of ecophysiological gas fluxes may be derived.

Vapor Pressure Deficit

The vapor pressure deficit (Δw) of ambient is estimated from RH, T_L and T_A . Water vapor pressure w is calculated by an empirical formula (Tetens 1930).

$$w = RH \cdot w^{sat} = RH \cdot 610.78 \exp\left(\frac{17.27\,T}{T + 237.3}\right) \tag{D.1}$$

Assuming $RH_i = 100\%$, Δw (in Pa/kPa) reads

$$\Delta w = w_i - w_a = 610.78 \left[\exp\left(\frac{17.27\,T_L}{T_L + 237.3}\right) - RH_a \exp\left(\frac{17.27\,T_A}{T_A + 237.3}\right)\right] \tag{D.2}$$

Leaf Conductance to Water Vapor

With Δw given, the leaf conductance to water vapor (g_w^s, in mmol $m^{-2}s^{-1}$) is determined according to Eqn. (2.2).

$$J_w = g_w^s \cdot \Delta w \Rightarrow g_w^s = \frac{J_w}{\Delta w}. \tag{D.3}$$

As g_w^s is proportional to stomatal conductance, it is further referred to as such. The proportionality assumption is based on the fact that the conductance through the epidermis other than the stomata is negligible.

CO_2 Concentration in Intracellular Air Spaces

From Eqs. (2.1,2.2) the intracellular CO_2 (c_i) can be estimated by

$$\begin{aligned} \Delta c &= c_a - c_i = \frac{J_c}{g_c^s} = 1.6\frac{J_c}{g_w^s} \\ \Rightarrow c_i &= c_a - 1.6\frac{J_c \Delta w}{J_w} \end{aligned} \tag{D.4}$$

Scaling c_i to c_a, which is assumed to be constant at 360 μmol mol^{-1}, yields the dimensionless quantity

$$c_{ia} = \frac{c_i}{c_a} = 1 - 1.6\frac{J_c \Delta w}{J_w c_a}, \tag{D.5}$$

which is used further in this work instead of c_i itself.
In Chapter 2.1, c_c is mentioned as a further relevant CO_2 -concentration. It can be calculated as

$$c_c = c_a - \frac{J_c}{g_c^s + g_c^i} \tag{D.6}$$

The value of g_c^i was estimated to be 50 mmol $m^{-2}s^{-1}$ in *K. daigremontiana* (Maxwell et al. 1997). Assuming that this is a constant value, c_c could be computed. However, as the wave forms of c_c calculated in that way and c_i do not significantly differ from each other (data not shown), only c_i , and c_{ia} , respectively, were considered in this work.

Bibliography

Achermann, P. & Kunz, H. (1999). Modeling circadian rhythm generation in the suprachiasmatic nucleus with locally coupled self-sustained oscillators: Phase shifts and phase response curves. *J Biol Rhythms*, 14, 460–468.

Albano, A. M., Rapp, P. E., Abraham, N. B., & Passamante, A. (1996). Measures of spatio-temporal dynamics. *Physica D*, 96.

Aschoff, J. (1960). Exogenous and endogenous components in circadian rhythms. *Cold Spring Harbor Symp Quant Biol*, 25, 11–28.

Aschoff, J. (1988). Masking of circadian rhythms by zeitgebers as opposed to entrainment. In W. T. J. M. Hekkens, G. A. Kerkhoff, & W. J. Rietveld (Eds.), *Advances in the Biosciences (Trends in Chronobiology*, volume 73 (pp. 149–161). New York - NY, USA: Pergamon Press.

Aschoff, J. (1990). From temperature regulation to rhythm research. *Chronobiol Int*, 7, 179–186.

Ball, P. (1999). *The self-made tapestry. Pattern formation in nature*. Oxford, UK: Oxford University Press.

Barkai, N. & Leibler, S. (2000). Circadian clocks limited by noise. *Nature*, 403, 267–268.

Beck, F., Blasius, B., Lüttge, U., Neff, R., & Rascher, U. (2001). Stochastic noise interferes coherently with a model biological clock and produces specific dynamic behaviour. *P Roy Soc Lond B Bio*, 268, 1307–1313.

Benedito-Silva, A. A. (1999). Aspectos metodológicos da cronobiologia. In N. Marques & L. Menna-Barreto (Eds.), *Cronobiologia: Princípios e Aplicações* (pp. 215–236). São Paulo, Brazil: Editora da Universidade de São Paulo, 2nd edition.

Blasius, B. (1997). *Zeitreihenanalyse und Modellierung regulärer und irregulärer Photosyntheseoszillationen bei Crassulaceen-Säurestoffwechsel-Pflanzen*. PhD thesis, Department of Physics, Darmstadt University of Technology, Darmstadt, Germany.

Blasius, B., Beck, F., & Lüttge, U. (1997). A model for photosynthetic oscillations in Crassulacean acid metabolism (CAM). *J Theor Biol*, 184, 345–351.

Blasius, B., Beck, F., & Lüttge, U. (1998). Oscillatory model of Crassulacean acid metabolism: structural analysis and stability boundaries with a discrete hysteresis switch. *Plant Cell Environ*, 21, 775–784.

Blasius, B., Huppert, A., & Stone, L. (1999a). Complex dynamics and phase synchronization in spatially extended ecological systems. *Nature*, 399, 354–359.

Blasius, B., Neff, R., Beck, F., & Lüttge, U. (1999b). Oscillatory model of Crassulacean acid metabolism with a dynamic hysteresis switch. *P Roy Soc Lond B Bio*, 266, 93–101.

Blasius, B. & Stone, L. (2000). Chaos and phase synchronization in ecological systems. *Int J Bifurcation Chaos*, 10, 2361–2380.

Boashash, B. (1992). Estimating and interpreting the instanteneous frequency of a signal - part 1: Fundamentals. *Proc IEEE*, 80, 520–538.

Bohn, A., Geist, A., Rascher, U., & Lüttge, U. (2001). Responses to different external light rhythms by the circadian rhythm of Crassulacean acid metabolism in *Kalanchoë daigremontiana*. *Plant Cell Environ*, 24, 811–820.

Bohn, A., Hinderlich, S., Hütt, M. T., Kaiser, F., & Lüttge, U. (2003). Identification of rhythmic subsystems in the circadian cycle of Crassulacean acid metabolism under thermoperiodic perturbations. *Biol Chem*, 384.

Bohn, A., Rascher, U., Hütt, M. T., Kaiser, F., & Lüttge, U. (2002). Responses of a plant circadian rhythm to thermoperiodic perturbations with asymmetric temporal patterns and the rate of temperature change. *Biol Rhythm Res*, 33, 151–170.

Brezina, V., Orekhova, I. V., & Weiss, K. R. (1997). Control of time-dependent biological processes by temporally patterned input. *Proc Natl Acad Sci USA*, 94, 10444–10449.

Broda, H., Brugge, D., Homma, K., & Hastings, J. W. (1986). Circadian communication between unicells? *Cell Biophys*, 8, 47–63.

Buchanan-Bollig, I. C. (1984). Circadian rhythms in *Kalanchoë*: effects of irradiance and temperature on gas exchange and carbon metabolism. *Planta*, 160, 264–271.

Buck, J. & Buck, E. (1976). Synchronous fireflies. *Sci Am*, 234, 74–85.

Busch, H., Hütt, M. T., & Kaiser, F. (2001). The effect of colored noise on a network of nonlinear oscillators. *Phys Rev E*, 64, 021105.

Busch, H. & Kaiser, F. (2000). Noise enhanced signal correlation and wave propagation in networks of oscillatory and excitable systems. *Acta Physica Polonica B*, 31, 1143.

Cazelles, B. & Boudjema, G. (2001). The moran effect and phase synchronization in complex spatial community dynamics. *Am Nat*, 157, 670–676.

Collins, J. J. (1999). Fishing for function in noise. *Nature*, 402, 241–242.

Comins, H. N. & Farquhar, G. D. (1982). Stomatal regulation and water economy in Crassulacean acid metabolism plants: an optimization model. *J Theor Biol*, 99, 263–284.

Cook, R. M., Lindsay, J. G., Wilkins, M. B., & Nimmo, H. G. (1995). Decarboxylation of malate in the Crassulacean acid metabolism plant *Bryophyllum (Kalanchoë) fedtschenkoi*. *Plant Physiol*, 109, 1301–1307.

Daan, S. & Berde, C. (1978). Two coupled oscillators: Simulations of the circadian pacemaker in mammalian activity rhythms. *J Theor Biol*, 70, 297–313.

Devlin, P. F. (2002). Signs of the time: environmental input to the circadian clock. *J Exp Bot*, 53, 1535–1550.

Dodd, A. N., Borland, A. M., Haslam, R. P., Griffiths, H., & Maxwell, K. (2002). Crassulacean acid metabolism: plastic, fantastic. *J Exp Bot*, 53, 569–580.

d'Ortous de Mairan, J. J. (1729). Observation Botanique. In *Histoire de l'Academie Royale des Sciences* (pp. 35–36).

Dunlap, J. C. (1999). Molecular bases for circadian clocks. *Cell*, 96, 271–290.

Engelmann, W., Johnsson, A., Karlsson, H. G., Kobler, R., & Schimmel, M. L. (1978). Attenuation of the petal movement rhythm in Kalanchoë with light pulses. *Physiol Plant*, 43, 68–76.

Eskin, A. (1979). Identification and physiology of circadian pacemakers. Circadian system of the *Aplysia* eye: Properties of the pacemaker and mechanisms of its entrainment. *Fed Proc*, 38, 2570–2579.

Fall, C. P., Marland, E. S., Wagner, J. M., & Tyson, J. J., Eds. (2002). *Computational Cell Biology*. New York, NY: Springer.

Farquhar, G. D. & Sharkey, T. D. (1982). Stomatal conductance and photosynthesis. *Ann Rev Plant Physiol*, 33, 317–45.

Farquhar, G. D., von Caemmerer, S., & Berry, J. A. (2001). Models of photosynthesis. *Plant Physiol*, 125, 42–45.

Freund, J. A. & Pöschel, T., Eds. (2000). *Stochastic Processes in Physics, Chemistry and Biology*. Berlin and Heidelberg, Germany: Springer.

Friemert, V., Heininger, D., Kluge, M., & Ziegler, H. (1988). Temperature effects on malic-acid efflux from the vacuoles and on the carboxylation pathways in Crassulacean acid metabolism plants. *Planta*, 174, 453–461.

Friesen, W. O., Block, G. D., & Hocker, C. G. (1993). Formal approaches to understanding biological oscillators. *Ann Rev Physiol*, 55, 661–81.

Gallagher, R. & Appenzeller, T. (1999). Beyond reductionism. *Science*, 284, 79.

Gammaitoni, L., Hänggi, P., Jung, P., & Marchesoni, F. (1998). Stochastic resonance. *Rev Mod Phys*, 70, 223–287.

Garcia-Ojalvo, J. & Sancho, J. M. (1999). *Noise in Spatially Extended Systems*. New York - NY, USA: Springer.

Genty, B., Briantais, J. M., & Baker, N. R. (1989). The relationship between the quantum yield of photosynthetic electron transport and quenching of chlorophyll fluorescence. *Biochim Biophys Acta*, 990, 87–92.

Gibbs, W. W. (2001). Cybernetic cells. *Sci Am*, (8), 42–47.

Giersch, C. (2000). Mathematical modelling of metabolism. *Curr Opin Plant Biol*, 3, 249–253.

Glass, L. (2001). Synchronization and rhythmic processes in physiology. *Nature*, 410, 277–284.

Goldbeter, A. (1996). *Biochemical Oscillations and Cellular Rhythms*. Cambridge, UK: Cambridge University Press.

Gooch, V. D., Wehseler, R. A., & Gross, C. G. (1994). Temperature effects on the resetting of the phase of the *Neurospora* circadian rhythm. *J Biol Rhythms*, 9, 83–94.

Grams, T. E. E., Beck, F., & Lüttge, U. (1996). Generation of rhythmic and arrhythmic behaviour of Crassulacean acid metabolism in *Kalanchoë daigremontiana* under continuous light by varying the irradiance or temperature: Measurements in vivo and model simulations. *Planta*, 198, 110–117.

Grams, T. E. E., Borland, A. M., Roberts, A., Griffiths, H., Beck, F., & Lüttge, U. (1997). On the mechanism of reinitiation of endogenous Crassulacean acid metabolism rhythm by temperature changes. *Plant Physiol*, 113, 1309–1317.

Grenfell, B. T., Wilson, K., Finkenstädt, B. F., Coulson, T. N., Murray, S., Albon, S. D., Pemberton, J. M., Clutton-Brock, T. H., & Crawley, M. J. (1998). Noise and determinism in synchronized sheep dynamics. *Nature*, 394, 674–677.

Hafke, J. B., Hafke, Y., Smith, J. A. C., Lüttge, U., & Thiel, G. (2003). Vacuolar malate uptake is mediated by an anion-selective inward rectifier. *Plant J*, 35.

Haken, H. (1975). Cooperative effects in systems far from thermal equilibrium and in nonphysical systems. *Rev Mod Phys*, 47, 67–121.

Haken, H. (1977). *Synergetics: An introduction*. Berlin and Heidelberg, Germany: Springer.

Haken, H. (1983). *Advanced Synergetics*. Berlin and Heidelberg, Germany: Springer.

Hartwell, L. H., Hopfield, J. J., Leibler, S., & Murray, A. W. (1999). From molecular to modular cell biology. *Nature*, 402, C47–C52. (Suppl.).

Hennessey, T. L. & Field, C. B. (1991). Circadian rhythms in photosynthesis. *Plant Physiol*, 96, 831–836.

Hütt, M. T. (2001). *Datenanalyse in der Biologie*. Berlin and Heidelberg, Germany: Springer.

Hütt, M. T. & Neff, R. (2001). Quantification of spatio-temporal dynamics by means of cellular automata techniques. *Physica A*, 298, 498–516.

Johnson, C. H. (2001). Endogenous timekeepers in photosynthetic organisms. *Ann Rev Physiol*, 63, 695–728.

Johnson, C. H., Knight, M., Trewavas, A., & Kondo, T. (1998). A clockwork green: circadian programs in photosynthetic organisms. In P. J. Lumsden & A. J. Millar (Eds.), *Biological Rhythms and Photoperiodism in Plants* (pp. 1–34). Oxford, UK: Bios Scientific.

Kaiser, F. (1980). Nonlinear oscillations (limit cycles) in physical and biological systems. In P. L. E. Ushlengi (Ed.), *Nonlinear electromagnetics* (pp. 343–389). New York, NY: Academic Press.

Kaiser, F. (1996). Coded frequency signals and oscillations in non-linear systems. In H. Greppin, R. Degli Agosti, & M. Bonzon (Eds.), *Vistas on Biorhythmicity* (pp. 175–202). Geneva, Switzerland: University of Geneva.

Kaiser, F. (1999). Deterministic and noise-induced signal amplification and signal transfer in coupled nonlinear systems. *Cell Mol Biol Lett*, 4, 87–104.

Kaiser, F. (2000). External signals and internal oscillation dynamics: principal aspects and response of stimulated rhythmic processes. In J. Walleczek (Ed.), *Self-organized biological dynamics & nonlinear control* (pp. 15–43). Cambridge, UK: Cambridge University Press.

Kawato, M. & Suzuki, R. (1980). Two coupled neural oscillators as a model of the circadian pacemaker. *J Theor Biol*, 86, 547–575.

Keener, J. & Sneyd, J. (1998). *Mathematical Physiology*. New York, NY: Springer.

Kitano, H., Ed. (2001). *Foundations of Systems Biology*. Cambridge, MA: MIT Press.

Kitano, H. (2002a). Computational systems biology. *Nature*, 420, 206–210.

Kitano, H. (2002b). Systems biology: a brief overview. *Science*, 295, 1662–1664.

Kliemchen, A., Schomburg, M., Galla, H. J., Lüttge, U., & Kluge, M. (1993). Phenotypic changes in the fluidity of the tonoplast membrane of Crassulacean-acid-metabolism plants in response to temperature and salinity stress. *Planta*, 189, 403–409.

Knight, J. (2002). Bridging the culture gap. *Nature*, 419, 244–246.

Kopell, N. & Howard, L. N. (1973). Horizontal bands in the Belousov reaction. *Science*, 180, 1171–1173.

Kronauer, R. E. (1990). A quantitative model for the effects of light on the amplitude and phase of the deep circadian pacemaker, based on human data. In J. Horne (Ed.), *Sleep '90. Proceedings of the 10t European Congress on Sleep Research* (pp. 306–309). Bochum, Germany: Pontenagel.

Kuramoto, Y. (1984). *Chemical Oscillations, Waves and Turbulence*. Berlin and Heidelberg, Germany: Springer.

Lander et al., E. S. (2001). Initial sequencing and analysis of the human genome. *Nature*, 409, 860–921.

Lema, M., Golombek, D. A., & Echave, J. (2000). A simple delay model of the circadian pacemaker. *J Theor Biol*, 204, 565–573.

Lillo, C., Meyer, C., & Ruoff, P. (2001). The nitrate reductase circadian system. the central clock dogma contra multiple oscillatory feedback loops. *Plant Physiol*, 125, 1554–1557.

Lomb, N. R. (1976). Least-squares frequency analysis of unequally spaced data. *Astrophys Space Sci*, 39, 447–462.

Luscombe, N. M., Greenbaum, D., & Gerstein, M. (2001). What is bioinformatics? A proposed definition and overview of the field. *Method Inform Med*, 40, 346–358.

Lüttge, U. (2000). The tonoplast functioning as the master switch for circadian regulation of Crassulacean acid metabolism. *Planta*, 211, 761–769.

Lüttge, U. (2002). Circadian rhythmicity: Is the "biological clock" hardware or software? *Prog Bot*, 64, 277–319.

Lüttge, U. & Ball, E. (1978). Free running oscillations of transpiration and CO_2 exchange in CAM plants without a concomitant rhythm of malate levels. *Z Pflanzenphysiol*, 60, 69–77.

Lüttge, U. & Beck, F. (1992). Endogenous rhythms and chaos in Crassulacean acid metabolism. *Planta*, 188, 28–38.

Lüttge, U., Grams, T. E. E., Hechler, B., Blasius, B., & Beck, F. (1996). Frequency resonances of the circadian rhythm of CAM under external temperature rhythms of varied period lengths in continuous light. *Bot Acta*, 109, 422–426.

Lüttge, U., Kluge, M., & Bauer, G. (1997). *Botanik*. Weinheim, Germany: VCH, 2nd, corrected edition.

Lüttge, U. & Smith, J. A. C. (1984). Mechanism of passive malic-acid efflux from vacuoles of the CAM plant *Kalanchoë daigremontiana*. *J Membrane Biol*, 81, 149–158.

Mackey, M. & Glass, L. (1988). *From Clocks to Chaos. The Rhythms of Life*. Princeton, NJ: Princeton University Press.

Marques, M. D. & do Val, F. C. (1999). Evolução da ritmicidade biológica. In N. Marques & L. Menna-Barreto (Eds.), *Cronobiologia: Princípios e Aplicações* (pp. 203–214). São Paulo, Brazil: Editora da Universidade de São Paulo, 2nd edition.

Marques, M. D., Golombek, D., & Moreno, C. (1999). Adaptação temporal. In N. Marques & L. Menna-Barreto (Eds.), *Cronobiologia: Princípios e Aplicações* (pp. 45–84). São Paulo, Brazil: Editora da Universidade de São Paulo, 2nd edition.

Marques, N. & Menna-Barreto, L., Eds. (1999). *Cronobiologia: Princípios e Aplicações*. São Paulo, Brazil: Editora da Universidade de São Paulo, 2nd revised edition.

Matsuda, H. (2000). Physical nature of higher-order mutual information: Intrinsic correlations and frustration. *Phys Rev E*, 62, 3096–3102.

Maxwell, K., von Caemmerer, S., & Evans, J. R. (1997). Is a low internal conductance to CO_2 diffusion a consequence of succulence in plants with Crassulacean acid metabolism. *Aust J Plant Physiol*, 24, 777–786.

McClung, C. R. (2001). Circadian rhythms in plants. *Ann Rev Plant Physiol Plant Mol Biol*, 52, 139–162.

Merrow, M. & Roenneberg, T. (2001). The circadian cycle: is the whole greater than the sum of its parts? *Trends Genet*, 17, 4–7.

Millar, A. J. (1998). The cellular organization of circadian rhythms in plants: not one but many clocks. In P. J. Lumsden & A. J. Millar (Eds.), *Biological Rhythms and Photoperiodism in Plants* (pp. 51–68). Oxford, UK: Bios Scientific Publ.

Millar, A. J. (1999). Biological clocks in *Arabidopsis thaliana*. *New Phytol*, 141, 175–197.

Mouravieff, P. J. (1956). Action du CO_2 sur l'appareil stomatique séparé du mésophylle. *Botaniste*, 195, 195–212.

Murray, J. D. (1993). *Mathematical Biology*. Berlin, Heidelberg - Germany: Springer, 2nd corrected edition.

Neff, R., Blasius, B., Beck, F., & Lüttge, U. (1998). Thermodynamics and energetics of the tonoplast membrane operating as an hysteresis switch in an oscillatory model of Crassulacean acid metabolism. *J Membrane Biol*, 165, 37–43.

Nicolis, G. (1995). *Introduction to nonlinear science*. Cambridge, UK: Cambridge University Press.

Nimmo, H. G. (2000). The regulation of phosphoenolpyruvate carboxylase in CAM plants. *Trends Plant Sci*, 5, 75–80.

Njus, D., McMurray, L., & Hastings, J. W. (1977). Conditionality of circadian rhythmicity: Synergistic action of light and temperature. *J Comp Physiol B*, 117, 335–344.

Nobel, P. S. (1999). *Physicochemical and Environmental Plant Physiology*. San Diego - CA, USA: Academic Press, 2nd edition.

Nuernbergk, E. L. (1961). Endogener Rhythmus und CO_2-Stoffwechsel bei Pflanzen mit diurnalem Säurerhythmus. *Planta*, 56, 28–70.

Nungesser, D., Kluge, M., Tolle, H., & Oppelt, W. (1984). A dynamic computer model of the metabolic and regulatory processes in Crassulacean acid metabolism. *Planta*, 162, 204–214.

Osmond, C. B. (1978). Crassulacean acid metabolism: a curiosity in context. *Ann Rev Plant Physiol*, 29, 379–414.

Otnes, R. K. & Enochson, L. (1972). *Digital Time Series Analysis*. New York - NY, USA: John Wiley & Sons.

Ouyang, Y., Andersson, C. R., Kondo, T., & Johnson, C. H. (1998). Resonating circadian clocks enhance fitness in cyanobacteria. *Proc Natl Acad Sci USA*, 95, 8660–8664.

Peterson, E. L. (1980). A limit cycle interpretation of a mosquito circadian oscillator. *J Theor Biol*, 84, 281–310.

Peterson, E. L. & Jones, M. D. R. (1979). Do circadian oscillators ever stop in constant light? *Nature*, 280, 677–679.

Pikovsky, A., Rosenblum, M., & Kurths, J. (2001). *Synchronization. A universal concept in nonlinear sciences*. Cambridge, UK: Cambridge University Press.

Pikovsky, A. S. & Kurths, J. (1997). Coherence resonance in a noise-driven excitable system. *Phys Rev Lett*, 78, 775–778.

Post, E. & Forchhammar, M. C. (2002). Synchronization of animal population dynamics by large-scale climate. *Nature*, 420, 168–171.

Press, W. H., Teukolsky, S. A., Vetterling, W. T., & Flannery, B. P. (1992). *Numerical Recipes in Fortran. The Art of Scientific Computing*. Cambridge, UK: Cambridge University Press, 2nd edition.

Quian Quiroga, R., Kraskov, A., Kreuz, T., & Grassberger, P. (2002). Performance of different synchronization measures in real data: A case study on electroencephalographic signals. *Phys Rev E*, 65, 041903.

Ranta, E., Kaitala, V., & Lindström, J. (1997). The spatial dimensions in population fluctuations. *Science*, 278, 1621–1623.

Rascher, U. (2001). *Der endogene CAM-Rhythmus von* Kalanchoë daigremontiana *als nichtlineares Modellsystem zum Verständnis der raum-zeitliche Dynamik einer biologischer Uhr*. PhD thesis, Department of Biology, Darmstadt University of Technology, Darmstadt, Germany.

Rascher, U., Blasius, B., Beck, F., & Lüttge, U. (1998). Temperature profiles for the expression of endogenous rhythmicity and arrhythmicity of CO_2 exchange in the CAM plant *Kalanchoë daigremontiana* can be shifted by slow temperature changes. *Planta*, 207, 76–82.

Rascher, U., Hütt, M. T., Siebke, K., Osmond, B., Beck, F., & Lüttge, U. (2001). Spatiotemporal variation of metabolism in a plant circadian rhythm: The biological clock as a assembly of coupled individual oscillators. *P Natl Acad Sci USA*, 98, 11801–11805.

Rensing, L. & Ruoff, P. (2002). Temperature effect on entrainment, phase shifting, and amplitude of circadian clocks and its molecular bases. *Chronobiol Int*, 19, 807–864.

Ritz, D. & Kluge, M. (1987). Circadian rhythmicity of CAM in continuous light: coincidences between gas exchange parameters, $^{14}CO_2$ fixation patterns and PEP-carboxylase properties. *J Plant Physiol*, 131, 267–284.

Roenneberg, T. & Hastings, J. W. (1993). Cell movement and pattern formation in *Gonyaulax polyhedra*. In L. Rensing (Ed.), *Oscillations and Morphogenesis* (pp. 399–412). New York - NY, USA: Marcel Dekker.

Roenneberg, T. & Merrow, M. (1998). Molecular circadian oscillators: An alternative hypothesis. *J Biol Rhythms*, 13, 167–179.

Roenneberg, T. & Merrow, M. (1999). Circadian systems and metabolism. *J Biol Rhythms*, 14, 449–459.

Rosenblum, M., Pikovsky, A., Kurths, J., Schäfer, C., & Tass, P. A. (2001). Phase synchronization: from theory to data analysis. In A. J. Hoff (Ed.), *Handbook of Biological Physics*, volume 4, Neuro-informatics, of *Handbook of Biological Physics* chapter 9, (pp. 279–321). Amsterdam, The Netherlands: Elsevier Science.

Ruf, T. (1999). The Lomb-Scargle periodogram in biological rhythm research: Analysis of incomplete and unequally spaced time-series. *Biol Rhythm Res*, 30, 178–201.

Russell, D. F., Wilkens, L. A., & Moss, F. (1999). Use of behavioural stochastic resonance by paddle fish for feeding. *Nature*, 402, 291–294.

Rutter, J., Reick, M., & McKnight, S. L. (2002). Metabolism and the control of circadian rhythms. *Annu Rev Biochem*, 71, 307–331.

Rutter, J., Reick, M., Wu, L. C., & McKnight, S. L. (2001). Regulation of clock and NPAS2 DNA binding by the redox state of NAD cofactors. *Science*, 293, 510–514.

Scargle, J. D. (1982). Studies in astronomical time series analysis. II. Statistical aspects of spectral analysis of unevenly spaced data. *Astrophys J*, 263, 835–853.

Scheper, T. O., Klinkenberg, D., Pennartz, C., & Pelt, J. V. (1999). A mathematical model for the intracellular circadian rhythm generator. *J Neurosci*, 19, 40–47.

Schibler, U., Ripperger, J. A., & Brown, S. A. (2001). Chronobiology - reducing time. *Science*, 293, 437–438.

Schnackenberg, J. (1979). Simple chemical reaction systems with limit cycle behaviour. *J Theor Biol*, 81, 389–400.

Schreiber, U. & Bilger, W. (1993). Progress in chlorophyll fluorescence research: major developments during the past years in retrospect. *Prog Bot*, 54, 151–172.

Schreiber, U., Schliewa, U., & Bilger, W. (1986). Continuous recording of photochemical and nonphotochemical quenching with a new type of modulated fluorometer. *Photosynth Res*, 10, 51–62.

Shannon, C. E. (1948). A mathematical theory of communication. *Bell Syst Techn J*, 27, 379–423.

Strogatz, S. H. (1994). *Nonlinear Dynamics and Chaos*. Reading, MA: Addison-Wesley.

Strogatz, S. H. (2000). From Kuramoto to Crawford: exploring the onset of synchronization in populations of coupled oscillators. *Physica D*, 143, 1–20.

Szathmáry, E., Jordán, F., & Pál, C. (2001). Can genes explain biological complexity? *Science*, 292, 1315–1316.

Tass, P., Rosenblum, M. G., Weule, J., Kurths, J., Pikovsky, A., Volkmann, J., Schnitzler, A., & Freund, H. J. (1998). Detection of n:m phase locking from noisy data: application to magnetoencephalography. *Phys Rev Lett*, 81, 3291–3294.

Tass, P. A. (1999). *Phase Resetting in Medicine and Biology*. Berlin and Heidelberg, Germany: Springer.

Tetens, O. (1930). Über einige meteorologische Begriffe. *Z Geophys*, 6, 297–309.

Thain, S. C., Hall, A., & Millar, A. J. (2000). Functional independence of circadian clocks that regulate plant gene expression. *Curr Biol*, 10, 951–956.

van der Pol, B. (1926). On relaxation oscillations. *Phil Mag*, 2, 978–992.

Van Dongen, H. P. A., Olofsen, E., VanHarteveld, J. H., & Kruyt, E. W. (1999). A procedure of multiple period searching in unequally spaced time-series with the Lomb-Scargle method. *Biol Rhythm Res*, 30, 149–177.

Venter et al., J. C. (2001). The sequence of the human genome. *Science*, 291, 1304–1351.

von Bertalanffy, L. (1968). *General System Theory*. New York, NY: Braziler.

Walleczek, J., Ed. (2000). *Self-Organized Biological Dynamics & Nonlinear Control*. Cambridge, UK: Cambridge University Press.

Warren, M. D. & Wilkins, M. B. (1961). An endogenous rhythm in the rate of dark-fixation of carbon dioxide in leaves of *Bryophyllum fedtschenkoi*. *Nature*, 191, 686–688.

Wedding, R. T. (1989). Malic enzymes of higher plants. *Plant Physiol*, 90, 367–371.

Welsh, D. K., Logothetis, D. E., Meister, M., & Reppert, S. M. (1995). Individual neurons dissociated from rat suprachiasmatic nucleus express independently phased circadian firing rhythms. *Neuron*, 14, 697–706.

Wiener, N. (1948). *Cybernetics or Control and Communication in the Animal and the Machine*. Cambridge, MA: MIT Press.

Wilkins, M. B. (1983). The circadian rhythm of carbon-dioxide metabolism in *Bryophyllum*: the mechanism of phase-shift induction by thermal stimuli. *Planta*, 157, 471–480.

Wilkins, M. B. (1991). The role of the epidermis in the generation of the circadian rhythm of carbon dioxide fixation in leaves of *Bryophyllum fedtschenkoi*. *Planta*, 185, 425–431.

Winfree, A. T. (2001). *The Geometry of Biological Time*. New York - NY, USA: Springer, 2nd edition.

Winter, K. & Smith, J. A. C., Eds. (1996). *Crassulacean Acid Metabolism. Biochemistry, ecophysiology and evolution.* Berlin, Heidelberg, Germany: Springer.

Wu, H., Lu, J., & Li, B. (2000). A coupled oscillatory model mimicking avian circadian regulatory systems. *J Biol Phys*, 26, 261–272.

Wyka, T. P. & Lüttge, U. (2003). Contributions of C_3 carboxylation to the circadian rhythm of carbon dioxide uptake of the Crassulacean acid metabolism plant *Kalanchoë daigremontiana*. *J Exp Bot*, 54, 1471–1479.

Yamada, S. (1999). Information-theoretical analysis of small neuronal networks. In U. Windhorst & H. Johansson (Eds.), *Modern Techniques in Neuroscience Research* (pp. 543–588). Heidelberg, Germany: Springer.

Zeiger, E. & Hepler, P. K. (1977). Light and stomatal function: blue light stimulated swelling of guard cell protoplasts. *Science*, 196, 887–889.

Acknowledgments

I would like to thank Prof. Dr. Friedemann Kaiser for the friendly reception in his group, for the granted freedom, the constructive criticism and discussions, and the trust in my work. I would furthermore like to acknowledge his efforts in promoting the idea that modern theory-groups working with computational tools require funding which goes beyond paper and pencils only.

To Prof. Dr. Ulrich Lüttge I would like to express my gratitude for his interest in interdisciplinary interactions, for many intensive and fruitful discussions, and for many important advices concerning biological issues.

I would like to extend my thanks to Prof. Dr. Mário José de Oliveira, for giving me the chance to stay at the University of São Paulo. During my time in Brazil I enjoyed many fruitful discussions with numerous scientists from Physics and Biology, some of which also gave me the opportunity to present my work to a greater audience, for which I am very grateful.

In the Nonlinear Dynamics Group I have been lucky to find a place with a friendly working atmosphere and many stimulating discussions, for which I would like to thank all former and current members of the group, in particular Dr. Andreas Stepken, Ivona Zerajic, Kristian Motzek, and - of course - Hauke Busch, to whom I owe extra thanks for being a committed and innovative system administrator and a great partner in crime.

A thank you is reserved for the other physicists with whom I enjoyed working in the Graduiertenkolleg 340 “Communication in Biological Systems”, as there are Prof. Dr. Friedrich Beck, Juniorprof. Dr. Marc-Thorsten Hütt, Dr. Luis Diambra, and Roland Neff. Fundamental for this work were the experimental efforts by Dr. Uwe Rascher, Dr. Tomasz Wyka, who is also thanked for critically reading the biological parts of this work, Heitor Monteiro Duarte, Anja Geist, and Sven Hinderlich. I am very grateful for having been entrusted with their data and for the vivid interdisciplinary dialogue. For the cooperative atmosphere I would like to thank all other members of the Graduiertenkolleg.

Many thanks are directed to the Deutsche Forschungsgemeinschaft (DFG) for a scholarship plus generous support within the Graduiertenkolleg 340 “Communication in Biological Systems”.

A very special set of thanks goes out to my family members, relatives and friends for their comprehension, their patience and their support. Big additional thanks are submitted to my friends in Brazil for their generous and kind support during my stays over there.

Last not least, this work would not have been possible without the fundamental and unconditional support in all aspects I have received from my parents Dr. Manfred and Brigitte Bohn, to whom I owe my deepest gratitude.

Summary

Rhythmic processes are fundamental for the temporal organization of the behaviour of living organisms. In particular under the geophysical 24 h - cycle of light intensity and temperature, endogenous timekeepers, so-called circadian clocks, have evolved in almost all species of the plant and animal kingdom.
This thesis deals with circadian clocks in Crassulacean acid metabolism (CAM), an eco-physiological adaptation of photosynthesis to conditions of water scarcity. The interest is on systems, which are composed of several circadian clocks, like leaves of the CAM plant *Kalanchoë daigremontiana* consisting of a large number of cells, or systems of various functionally different but interacting rhythms, like the diurnal rhythm in carbon metabolism in the photosynthesizing mesophyll cells and the circadian oscillations of the stomatal guard cells controlling the gas exchange of the mentioned plant. The general aim is the understanding of the collective dynamics of the entire system, which is here achieved with mathematical methods based on the theory of nonlinear dynamical systems. This work is a further project within an interdisciplinary co-operation of biologists and theoretical physicists, which so far has lead to the formulation of a quantitative model of the circadian rhythm of CAM. This model is based on the following hypotheses:

- The central pacemaking process (the clock) of CAM is the periodic uptake and release of malic acid by the cell vacuole. Robust circadian oscillations are generated by a nonlinear feedback of the vacuolar malic acid concentration on the malic acid transport over the tonoplast membrane around the vacuole. Hence, in this model, the circadian clock is fully located at the metabolic level.

- Beyond a sharply delimited range of light intensities and temperature this oscillator stops in a defined phase of the normal cycle.

- Further potential pacemakers, like circadian gene expression or guard cell movements are slaved by this master-oscillator.

- The collective dynamics of an entire leaf can only be understood by a statistical consideration of the large number of leaf cells. In this picture, collective processes like the desynchronization of different leaf patches induced by omni-present random fluctuations, and the phase reset by strong environmental signals (temperature

pulses) working equally on all cells, respectively are fundamental for the integrated, macroscopic rhythm.

In order to check the last hypothesis, an imaging method has been installed at the Institute of Botany of the Darmstadt University of Technology, allowing to monitor the spatio-temporal distribution of metabolic activity in the an intact leaf, while simultaneously recording the integrated CO_2 -uptake and transpiration losses of the leaf.

The present work investigates the circadian rhythmicity of multi-oscillator systems in *Kalanchoë daigremontiana* by means of two computational tools, the *quantitative analysis of experimental data* and *computer simulation*.
One principal objective of data analysis is the characterization of the period as well as the amplitude- and phase dynamics of individual rhythms. For this purpose special analysis tools are required in order to obtain reliable information also from short and noisy timeseries. Furthermore, statistical measures for the characterization of populations of oscillators are applied, and the spatial distribution of rhythm properties in a leaf or in simulations of 1-dimensional chains of oscillators are discussed. A further main aspect is the analysis of the interaction of diverse rhythms by calculation of cross-correlations, phase differences and synchronization indices. This allows the identification of leaf patches being synchronized and correlated among each other and with environmental quantities.
For a better understanding of of the collective dynamics of many identical circadian clocks, populations of phenomenological minimal models of biological clocks are simulated. Diverse scenarios of of environmental conditions and their effect on populations of excitable and oscillatory systems, respectively, are examined. The comparison of the simulated populations with experimental data allows to draw conclusions on the emergence of macroscopic rhythmicity and spatio-temporal pattern formation from many microscopic oscillations. Furthermore, simulations of CAM with a physiologically detailed model lead to testable predictions about the impact of certain experimental protocols on the circadian rhythms of CO_2 uptake and transpiration. Here, the comparison of experiment and simulation allows a verification of the physiological hypotheses behind the model.

Altogether, the results of this work lead to the following conclusions:

- The collective dynamics of the ensemble of cells is correlated to the dynamics of each individual cell. All properties of the macroscopic rhythm are also seen in the microscopic rhythms, that is by averaging over the entire population, no additional effects appear.

- Rhythm generation in each spot of the leaf is the outcome of a complex network of functionally different oscillators, comprising several rhythms on various levels from the environment to metabolism and gene expression.

- The disappearance of an observable rhythm is most likely not caused by a stopping of the circadian clock, but rather by a breakdown of the signaling pathway from the clock to the output.
- Dynamical pattern formation and synchronization in the physiologically homogeneous leaf tissue is most likely induced by the heterogeneous, spatio-temporal properties of the environmental conditions.

It is to be expected that a continued cultivation of interdisciplinary systems-biological research in CAM plants will yield important contributions to the basic understanding of i) the physiological and molecular keys to time-keeping processes in plants and ii) the emergence of dynamical patterns and synchronization in spatially extended ecosystems exposed to fluctuating environments.

Zusammenfassung

Rhythmische Prozesse sind von zentraler Bedeutung für die zeitliche Organisation des Verhaltens lebender Organismen. Insbesondere durch den geophysikalischen 24 h - Zyklus von Lichtintensität und Temperatur sind in nahezu allen Arten der Pflanzen- und Tierwelt endogene Schrittmacher, so genannte circadiane Uhren, entstanden.
Diese Dissertation beschäftigt sich mit circadianen Uhren im Crassulaceen Säurestoffwechsel (CAM), einer ökophysiologischen Anpassung photosynthetischer Organismen an Wassermangel hervorrufende Umweltbedingungen. Von Interesse sind dabei Systeme, die aus mehreren circadianen Uhren aufgebaut sind, wie z.B. das aus einer Vielzahl von Zellen bestehende Blattgewebe der CAM Pflanze *Kalanchoë daigremontiana* , oder in der selben Pflanzen anzutreffende Systeme funktional verschiedener, gekoppelter Rhythmen, wie z.B. dem Kohlenstoff-Metabolismus der photosynthetisierenden Mesophyllzellen, und den circadianen Bewegungen der den Gasaustausch kontrollierenden stomatären Schließzellen. Ziel ist in jedem Fall das Verständnis der kollektiven Dynamik des Gesamtsystems, welches hier durch Anwendung von mathematischen Methoden, basierend auf der Theorie nichtlinearer dynamischer Systeme, erreicht werden soll.

Diese Arbeit ist ein weiteres Projekt im Rahmen einer interdisziplinäre Zusammenarbeit von Biologen und theoretischen Physikern, aus deren vorigem Wirken ein quantitatives Modell zur Beschreibung grundlegender Eigenschaften circadianer Rhythmen im CAM hervorgegangen ist. Dieses Modell beruht auf den folgenden Hypothesen:

- Der zentrale schrittmachende Prozess (die Uhr) des CAM besteht im periodischen Füllen und Entleeren der Zellvakuole mit Äpfelsäure. Robuste circadiane Oszillationen werden erzeugt durch die nichtlineare Rückkopplung der Äpfelsäurekonzentration in der Vakuole auf den Äpfelsäuretransport durch die (die Vakuole umgebende) Tonoplastenmembran. Das heißt, die circadiane Uhr ist in diesem Modell vollständig auf der metabolischen Ebene angesiedelt.

- Jenseits eines scharf begrenzten Bereichs von Lichtintensität und Temperatur kommt dieser Oszillator in einer wohl definierten Phase des normalen Zyklusses zum Stillstand.

- Weitere potenzielle Schrittmacher, wie z.B. circadiane Genexpressionszyklen, oder rhythmische Schließzellbewegungen sind dem Tonoplastenoszillator untergeordnet.

- Die Gesamtdynamik eines ganzen Blattes kann nur durch statistische Mittelwertsbildung der großsen Anzahl von Zellen im Blatt verstanden werden. Fundamental hierbei sind kollektive Prozesse, wie z.B. die durch stets präsente zufällige Fluktuationen herbeigeführte Desynchronisation verschiedener Blattbereiche, die durch auf alle Zellen gleichermaßen wirksame, starke Umweltsignale (z.B. Temperaturpulse), aufgehoben wird.

Zur Überprüfung der letztgenannten Hypothese wurde am Institut für Botanik der Technischen Universität Darmstadt ein bildgebendes Verfahren etabliert, welches es ermöglicht, die raumzeitliche Verteilung der metabolischen Aktivität im Blatt darzustellen, und simultan über das gesamte Blatt integrierte Aufzeichnungen der ökophysiologischen CO_2 - und Wasserdampfflüsse in und aus dem Blatt vorzunehmen.

Die vorliegende Arbeit untersucht die circadiane Rhythmik von Multioszillatorensystemen in *Kalanchoë daigremontiana* mit Hilfe zweier rechnerischer Werkzeuge, der *quantitativen Analyse experimenteller Daten* und der *Computersimulation*.
Ein Hauptziel der Datenanalyse ist die Charakterisierung der Periode sowie der Amplituden- und Phasendynamik individueller Rhythmen. Hierzu sind spezielle Analyseverfahren notwendig, um verlässliche Informationen auch aus relativ kurzen und rauschbehafteten Signalen zu erhalten. Desweiteren werden statistische Maße zur Charakterisierung von Populationen angewandt und die räumliche Verteilung von Rhythmuseigenschaften im Blatt oder in Simulationen 1-dimensionaler Ketten von Oszillatoren betrachtet. Ein weiterer Hauptaspekt ist die Analyse der Wechselwirkung verschiedener Rhythmen durch Berechnung von Kreuzkorrelationen, Phasendifferenzen und Synchronisationsindizes. Diese erlaubt die Identifikation von untereinander bzw. mit Umweltgrößen synchronisierten und korrelierten Blattbereichen.
Zum besseren Verständnis der kollektiven Dynamik vieler identischer circadianer Uhren werden Populationen phänomenologischer Minimalmodelle biologischer Uhren simuliert. Verschiedene Szenarien von Umweltbedingungen und deren Wirkung auf Populationen erregbarer bzw. oszillatorischer Systeme werden untersucht. Der Vergleich der simulierten Population mit experimentellen Daten erlaubt Rückschlüsse auf die Entstehung makroskopischer Rhythmik und raumzeitlicher Strukturbildung aus vielen mikroskopischen Oszillationen. Desweiteren führt die Simulation des CAM mit einem physiologisch detaillierten Modell auf experimentell überprüfbare Vorhersagen der Auswirkung bestimmter experimenteller Protokolle auf die circadianen Rhythmen von CO_2 -Aufnahme und Transpiration. Hier erlaubt der Vergleich mit experimentellen Zeitserien eine Verifizierung der dem Modell zu Grunde liegenden physiologischen Hypothesen.

Zusammenfassend führen die Ergebnisse dieser Arbeit zu folgenden Schlüssen:

- Die integrierte Dynamik der gesamten Zellpopulation ist mit der Dynamik der einzelnen Zelle korreliert. Das heißt, alle Eigenschaften des makroskopischen Rhythmus

sind auch in den mikroskopischen Rhythmen zu beobachten, bzw. durch Mittelwertbildung über die Population treten keine zusätzlichen Effekte auf.

- Die Rhythmusgenerierung in jedem Punkt des Blattes ist das Ergebnis eines komplexen Netzwerks aus funktional verschiedenen Oszillatoren, das verschiedene Rhythmen auf mehreren Ebenen, von der Umwelt, über den Metabolismus bis zur Genexpression umfasst.

- Das Verschwinden eines sichtbaren Rhythmusses in der CO_2 -Aufnahme ist sehr wahrscheinlich nicht auf das Stoppen des circadianen Schrittmachers zurückzuführen, sondern auf eine Unterbrechung der Signaltransduktion von der circadianen Uhr zur sichtbaren Observablen.

- Dynamische Strukturbildung und Synchronisation im physiologisch homogenen Blattgewebe ist höchstwahrscheinlich auf die raumzeitliche Dynamik der Umweltbedingungen zurückzuführen.

Es ist zu erwarten, dass eine Fortführung der interdisziplinären Forschung an CAM Pflanzen bedeutend zum grundlegenden Verständnis i) der physiologischen und molekularen Bausteinen chronobiologischer Prozesse in Pflanzen und ii) der Entstehung dynamischer Strukturen und von Synchronisation in ausgedehnten Ökosystemen unter räumlich und zeitlich fluktuierenden Umweltbedingungen, beitragen wird.

Curriculum Vitae

Personal Data

Name:	Andreas Bohn
Date of birth:	29 March 1972
Place of birth:	Kronberg im Taunus, Germany
Citizenship:	Germany
Marital status:	unmarried, no children
Address:	Merckstraße 10, 64283 Darmstadt, Germany; e-mail: abohn@web.de

School Education

1978 - 1981	Grundschule Marxheim (elementary school) - Hofheim am Taunus, Germany
1981 - 1984	Heiligenstockschule (elem. school + orientation level) - Hofheim am Taunus
1984 - 1988	Rosenbergschule (grammar school) - Hofheim am Taunus
1988 - 1991	Main-Taunus-Schule (grammar school) - Hofheim am Taunus
06/1991	Abitur (graduation)

National Service

07/1991 - 07/1992	Grundwehrdienst (military service) - Eschweiler(Rheinland) and Fuldatal

Undergraduate Studies

10/1992 - 03/1998	Undergraduate studies in physics - Darmstadt University of Technology, Germany
10/1994	Vordiplom (Intermediate diploma)
09/1995 - 07/1996	EU-SOCRATES exchange, Physics Department, University of Salamanca, Spain
03/1997 - 03/1998	Diplomarbeit (dissertation), advisor: Prof. Dr. F. Kaiser, Institute of Applied Physics (IAP), Darmstadt U of T. Title: *Einfluss externer Rückkopplung auf polarisationsbistabile Halbleiterlaser* *(Influence of external feedback on polarization-bistable semiconductor lasers)*
03/1998	Diplom-Physiker (Diploma in physics, eqv. M.Sc.)

Graduate Studies

05/1998 - 04/2003	PhD studies, advisor: Prof. Dr. F. Kaiser, IAP, Physics Department, Darmstadt U of T
05/1998 - 04/2001	Scholarship, DFG Graduiertenkolleg 340 “Kommunikation in biologischen Systemen”, Biology Department, Darmstadt U of T
06/2001 - 05/2003	Research and teaching assistant, IAP, Darmstadt U of T
09/2001 - 10/2001	Short-visit, Institute of Physics, University of São Paulo, Brazil

Hiermit erkläre ich an Eides Statt, dass ich
die vorliegende Dissertation selbständig verfasst
und nur die angegebenen Hilfsmittel verwendet habe.
Ich habe bisher keinen Versuch unternommen, an einer
anderen Hochschule das Promotionsverfahren einzuleiten.

Darmstadt, im April 2003